Reaction mechanism of CaO-MgO-Al_2O_3-SiO_2 (CMAS) on lanthanide zirconia thermal barrier coatings

by

Honglong Wang

A dissertation submitted to the Graduate Faculty of
Auburn University
In partial fulfillment of the
Requirements for the Degree of
Doctor of Philosophy

Auburn, Alabama
May 7, 2016

Keywords: CMAS, TBC, corrosion, reaction mechanism

Approved by
Jeffrey W. Fergus, Chair, Professor of Materials engineering
Bart Prorok, Professor of Materials engineering
Dong-Joo Kim, Professor of Materials engineering
Robert Jackson, Professor of Mechanical engineering

Abstract

Higher operating temperature could improve energy efficiency in the gas turbine engines, and thus, thermal barrier system is applied to protect the superalloy blades from the high temperature. Thermal barrier system is a multi-layer system and the most significant part is the top layer, thermal barrier coating (TBC). TBC should not only protect the blades from the high temperature, but also resist the corrosion from the molten dust injected into the engines. Lanthanide zirconates are promising materials to replace currently used yttria stabilized zirconia as TBC materials due to its better thermal properties and higher corrosion resistance against molten dust. However, the corrosion resistance mechanism is still not clearly understood.

This paper targets to provide an essential understanding in lanthanide zirconates materials' corrosion resistance against molten dust. The molten dust was simulated by CaO-MgO-Al_2O_3-SiO_2 (CMAS) and the materials simulated as TBC were $[Gd_xSm_{(1-x)}]_2Zr_2O_7$ (x = 0, 0.2, 0.4, 0.6,0.8 and 1.0). The reactions between CMAS and lanthanide zirconates were studied to understand the corrosion mechanism. Lanthanide zirconates ceramics were prepared by solid oxide sintering and co-precipitation method in pellet shape and molten dust were prepared by sintering raw oxides (CaO, MgO, Al_2O_3, SiO_2) in stoichiometric ratio to get homogeneous glass powders. Then the CMAS powders were placed on top of lanthanide zirconates and sintered from 1200°C to 1500°C. All the samples were characterized by X-ray diffraction (XRD) and scanning electron microscopy (SEM)

equipped with energy-dispersive X-ray spectroscopy (EDS). CHAPTER 2 shows the experimental procedures, including how to prepare lanthanide zirconates and CMAS glass powders. CHAPTER 3 provides morphologies and properties of materials before corrosion. CHAPTER 4 discusses the CMAS corrosion properties on the lanthanide zirconates materials at higher temperature (>1250°C) and lower temperature (<1250°C). The trend in reaction products at various temperatures are also discussed in this chapter. Furthermore, the effect of porosities in lanthanide zirconates and CMAS composition on corrosion were studied in this chapter too. Effect of water flow on CMAS corrosion is discussed in Section 4.5. Then, the quantification of corrosion and function of reaction layer are shown in CHAPTER 5. In this chapter, corrosion on yttria stabilized zirconia was used to compare with corrosion on lanthanide zirconates.

Acknowledgments

First and foremost I would like to express my gratitude to my advisor Dr. Jeffrey Fergus for his expert guidance and help during my graduate studies at Auburn University. His valuable suggestions helped me a lot in my research work and dissertation writing. The most significant spirit I learnt from him during these years is the research attitude he conveyed besides the knowledge of materials science.

I also wish to thank my committee member, Dr. Dong-Joo Kim, Dr. Bart Prorok and Dr. Robert Jackson for their constructive advices and insightful suggestions, which is of assistance to finish this dissertation. I also appreciate the outside reader Dr. Minseo Park for his kindly help in this work. The grate thanks will also be given to Mr. Steven Moore for the technical support.

The special thanks are given to Dr. Dileep Kumar, Dr Victor Agubra, Dr. Yu Zhao, Dr Yingjia Liu, who helped me a lot on the pyrochlore materials preparation and experiment apparatus installation at the early stage of this work and gave me valuable discussions. Besides, I also thank Emily Tarwater, Xingxing Zhang and Ahmet Bakal for solving problems during my research. All my colleagues and friends in materials engineering deserve my sincere thanks.

I also acknowledge the financial support from the Department of Energy through the National Energy Technology Laboratory.

The last but not the least, I would like to give my most special thanks to my whole family for their selfless support. The special thanks are given to my wife Zhizhi Sheng and my new born baby Alice, who provide me the source of fighting.

Table of Contents

List of Tables

List of Figures

CHAPTER 1. Introduction

Gas turbine engines provide great power for airplanes and electrical generators. The working principle of gas turbine engine is shown in Figure 1.1. Fresh air is compressed and transported into the combustion room with fuels. After combustion, the hot air propels the metal turbines to make a workout. After all, the hot air was exhausted. This cycle is called "Brayton cycle" and the relationship of temperature and entropy is shown in Figure 1.2. Thus, the ideal thermal efficient of the gas turbine engine can be expressed in equation $\eta = (T_3 - T_4)/T_3$ [1]. This equation indicates that increased working temperature can increase the thermal efficiency. The working temperature in gas turbine engines can reach 1600°C for rocket engines and 1500°C for commercial jet engines [2].

The strength of metals decrease at elevated temperature and nickel-based superalloys have a maximum working temperature of around 1150°C [3]. Furthermore, the increasing demand of improving thermal efficiency and reducing carbon emissions motivate researchers to increase higher operating temperature. Thus, ceramic thermal barrier coatings (TBC) are applied to protect the turbine blades from the high temperature.

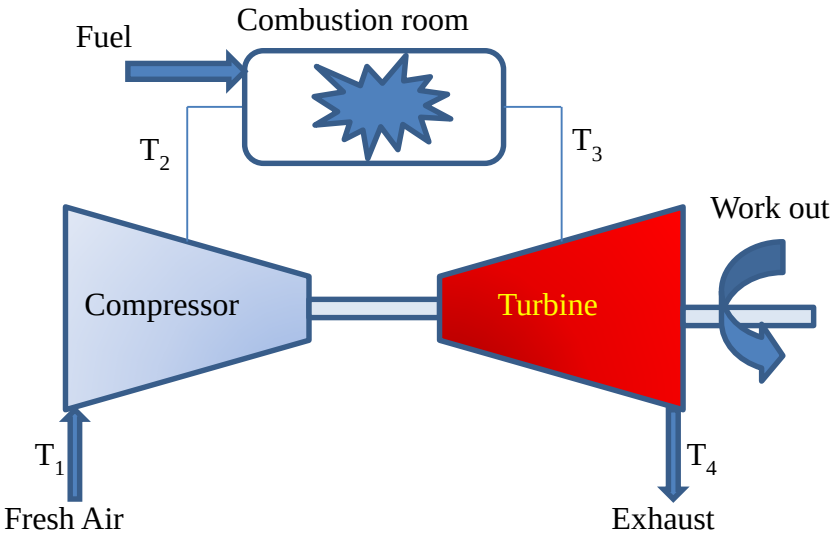

Figure 1.1 Working principle of gas turbine engines

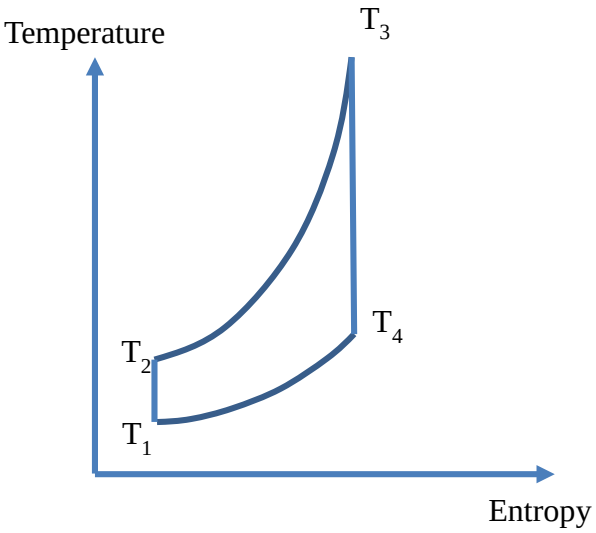

Figure 1.2 Schematic of Brayton cycle.

1.1. Thermal barrier system

Applying multi-layers of ceramic materials on the blades' surface is a promising way to increase the working temperature. The multi-layer system is shown in Figure 1.3. The dashed line in Figure 1.3 represents the temperature gradient in the system. The multi-

layer system contains thermal barrier coatings (over 100 μm), thermal grown oxide (0.1~10 μm) and bond coat (30~100 μm) [4].

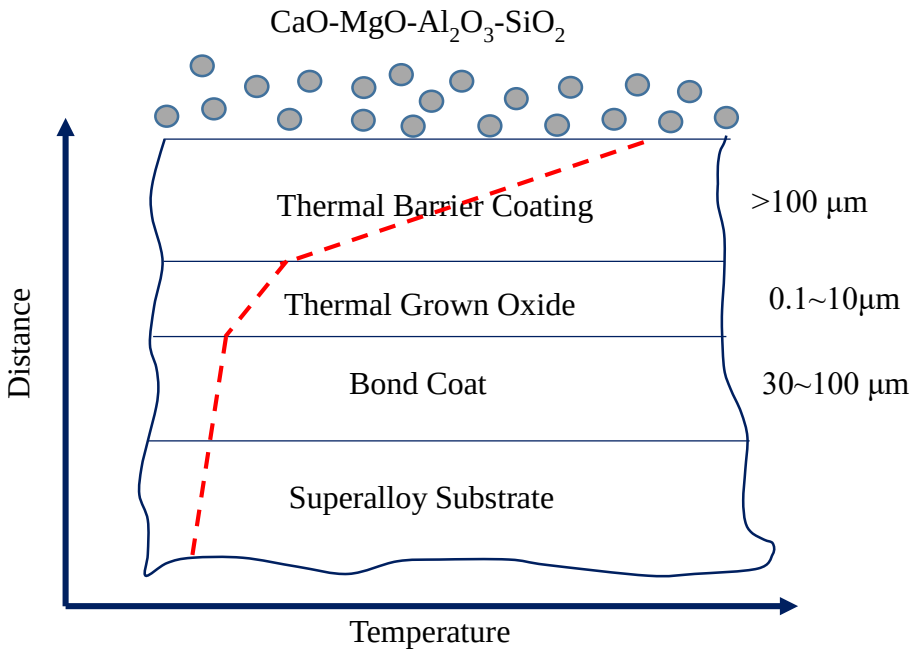

Figure 1.3 Schematic of multi-layer thermal barrier system

1.1.1. Thermal barrier coatings

The first layer in this system is the thermal barrier coating and it plays a significant role in reducing the surface temperature. Currently applied thermal barrier coatings can reduce the surface temperature above 165°C while the target is 200°C [5-7]. Lower metal blades' temperature can both help to increase the working temperature and extend the lifetime of the blades. The temperature drop is determined by several aspects, including material's thermal conductivity, porosity, coating thickness [5]. Meanwhile, the thermal expansion coefficient difference between the ceramic coatings and superalloy blades could cause residual stress and even cracks during thermal cycling, which may also result to the failure of thermal barrier coating. Appropriate porosity is helpful in thermal barrier coatings because porosity can reduce the residual stress and improve the strain tolerance in

thermal cycling. At the same time, pores in the coatings can also decrease the thermal conductivity.

Additionally, molten dust and ash from the air can be injected and deposited into the engines and then react with the coatings. Silicate phases could form after reaction and the coatings would not stabilized again [8]. The reaction product may not prevent heat and corrosion materials as well as before and cause the failure of the thermal barrier coatings [9, 10]. So it is concluded that the requirements of thermal barrier coatings are:

- Low thermal conductivity;
- Close thermal expansion coefficient with superalloy blades;
- High phase stability;
- Good corrosion resistance.

Currently, thermal barrier coatings are mainly manufactured by electron beam physical vapor deposition (EBPVD) [11, 12] or air plasma spray (APS) [13]. Schematic figures of coatings made by these two methods are shown in Figure 1.4. The micro-structures are obviously different for this two methods. Coatings manufactured by EBPVD have the columnar grown vertical to the substrate while the coatings deposited by APS have a parallel grains with substrate and the inter-grain pores have the parallel direction as the columnar. The inter-grain pores introduced in both manufacture methods help to reduce the thermal conductivity and improve the strain compliance [14-16]. In general, EBPVD can make the coatings with higher strain compliance, smoother surface but limits in materials due to the low use ratio of feed stocks [17]. Meanwhile, APS can provide various materials with lower thermal conductivity, higher chemical resistance and lower cost [18].

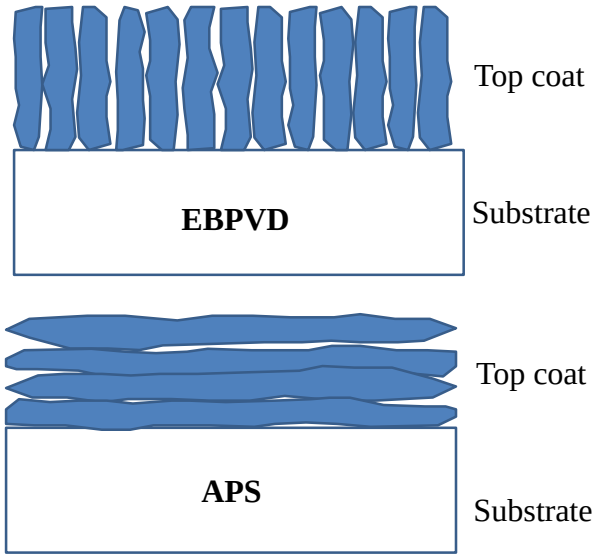

Figure 1.4 Micro-structure of thermal barrier coatings. Top is manufactured by EBPVD and the bottom is deposited by APS.

1.1.2. Bond coat

The third layer of thermal barrier system is bond coat. Bond coat provides good adhesion between ceramic top coating and superalloy blades. It can also protect the underlying superalloy blades by forming TGO and corrosion as well [6]. MCrAlY (M=Ni, Co or Ni+Co) alloy is the most common bond coat due to its good thermal property [4, 19]. Oxygen is transported through the porous thermal barrier coatings and then aluminum in the alloys would be oxidized and grow to be part of TGO due to the higher activity than chromium in superalloys. Thus, the superalloy blades would be protected under this oxide layer. The oxides can be easily formed, but grow slowly. However, the growth of TGO can consume aluminum in the bond coat and after Al's depletion, secondary oxides could form [19]. NiO_x or CoO_x (depends on what the M is in MCrAlY) with porous microstructure would form after Al is insufficient in bond coat. Thus, the layer would not be protective again [20].

Platinum accompanied with aluminide can also be part of bond coat to enhance the oxidation and corrosion resistance properties [21]. Additionally, recent study shows the Pt-added coating also provide better adhesion with the superalloys [22]. In Laney's research, the platinum aluminide coatings can improve from 150 cycles to 2233 cycles than pure nickel aluminide [23]. It is also reported that platinum plays a significant role in preventing sulfur's penetration and keeping aluminum in a higher level from forming a porous secondary oxides [24-26].

Hafnium and iridium can also be used to replace the expensive platinum in bond coat. In Hf-modified bond coat, Hf can be oxidized to HfO_2 and enhance the protective α-Al_2O_3 layer [27]. It is reported that even Hf addition as low as 0.05 at% can reduce the growth of α-Al_2O_3 remarkably and provide better adhesion than NiAl or Pt-NiAl [28]. However, several critical problems still exist for Hf-modified bond coat, including difficult to specify the optimal amount of Hf addition and hard to fabricate the coating because the composition would change due to the inter diffusion [22, 29].

1.1.3. Thermal grown oxide

The second layer of thermal barrier system is thermal grown oxide (TGO). Normally protective α-Al_2O_3 is applied between TBCs and bond coat to prevent further oxidation in bond coat [30, 31]. Without thermal grown oxide, the oxygen could be transported via the cracks and holes in TBCs, and thus, metal based bond coat would be oxidized [4].

Failure caused by TGO can be concluded into two aspects: Firstly, cracks grow as TGO thickens [32]. Secondly, a compressive residual stress exists in thermal grown oxide during thermal cycling due to it has a lower thermal expansion coefficient than metal based

bond coat [33]. The displacement between TGO and bond coat can also result to cracks [34]. So the requirements of TGO can be concluded as:

- Low growth rate;
- Limited defects;
- Adherent with bond coat.

1.2. Thermal barrier materials

1.2.1. Yttria stabilized zirconia

Zirconia was firstly applied as thermal barrier materials since 1960s due to its low thermal conductivity (2.5 $W \cdot m^{-1} \cdot K^{-1}$ at 1200°C), high melting point and relatively higher thermal expansion coefficient [35, 36]. Currently, yttria stabilized zirconia (YSZ) is the most applied material in thermal barrier coating. 6~8 wt% (3.4~4.5 mol%) Y_2O_3 stabilized zirconia presents good thermal properties according to the previous research. Vacancies caused by trivalent Y_2O_3 doping into tetravalent ZrO_2 results to decreased thermal conductivity. Recent research shows the thermal conductivity of 7YSZ drops in the range of 1.5~2.7$W \cdot m^{-1} \cdot K^{-1}$ at 1200°C [37-41]. The partially stabilized zirconia provides much longer thermal cycling life than pure zirconia in burner fig tests [5, 42]. The porous YSZ deposited by either APS or EB-PVD can provide strain tolerance during thermal cycling and thus, the lifetime increases. The relationship of lifetime and amount of Y_2O_3 is shown in Figure 1.5. 6~8 wt% Y_2O_3 stabilized ZrO_2 was reported at longest thermal cycling lifetime due to its specific fracture toughness.

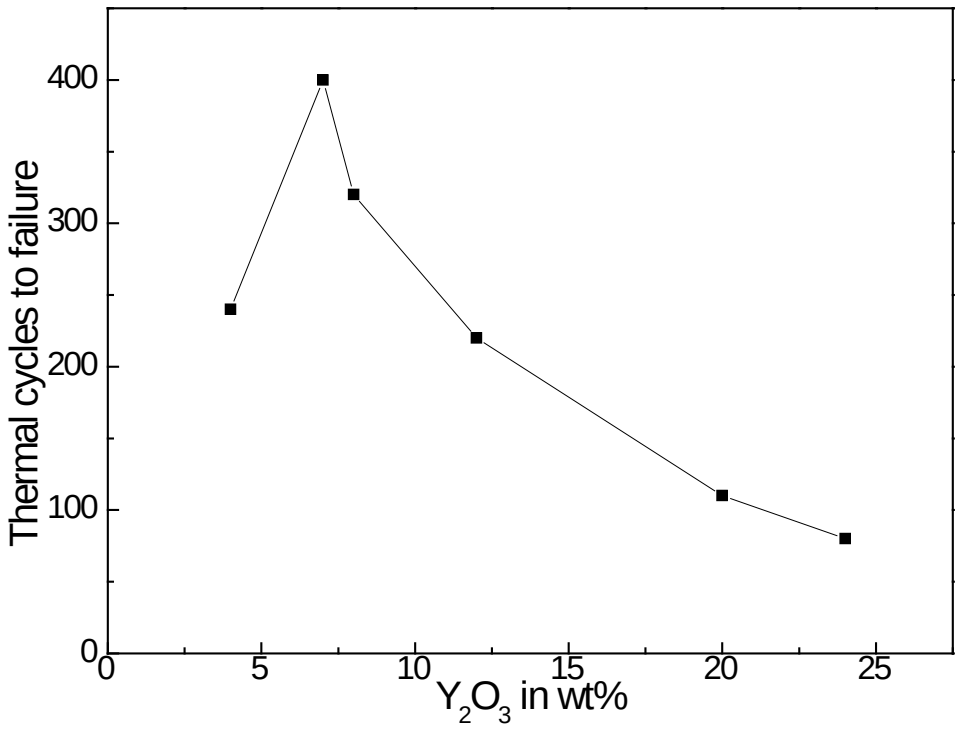

Figure 1.5 Relationship between Y_2O_3 amount and thermal cycles to failure (data from [35]).

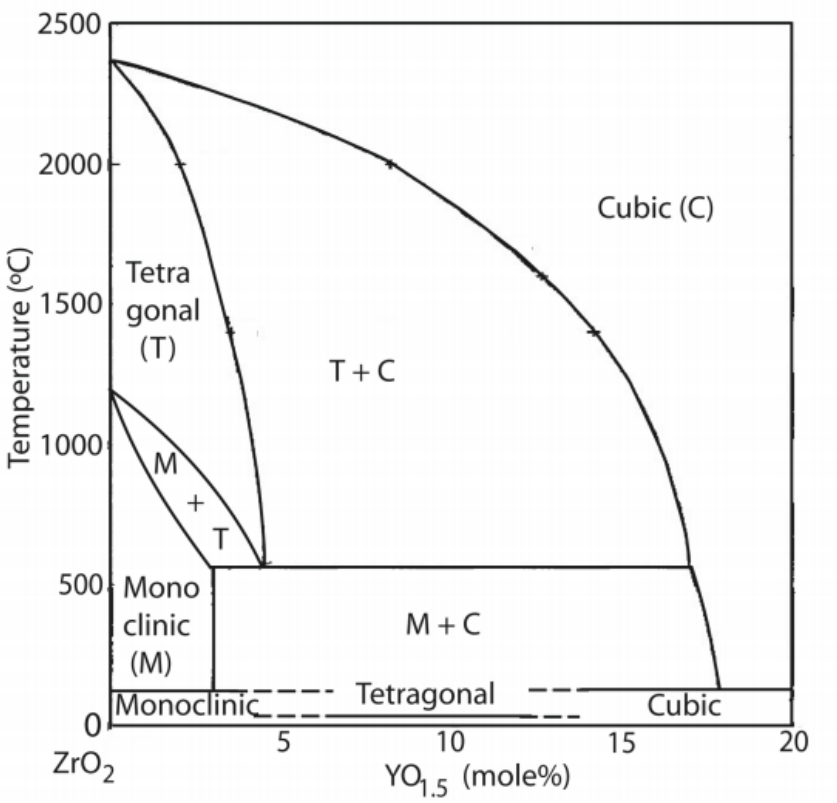

Figure 1.6 Phase diagram of $YO_{1.5}$-ZrO_2 [43].

The $YO_{1.5}$-ZrO_2 phase diagram is shown in Figure 1.6. From the phase diagram, it is clear to see that the 7.6 mol% $YO_{1.5}$-ZrO_2 corresponded to 7YSZ is mixed by two phases at the temperature of interest: Zr-rich phase in tetragonal and Y-rich phase in cubic. However, the performance of YSZ in thermal barrier coating is different as the bulk materials. Conflicting to equilibrium state mixed with tetragonal and cubic phase, a meta-stable phase, called t' phase, forms during the thermal barrier coating's fabrication, either by APS or EB-PVD [44]. The t' phase helps to improve thermal cycling life but transforms to tetragonal and monoclinic phases when the temperature is above 1200°C [5, 45]. A 3~4% volume change caused by phase transformation between t' phase and tetragonal phase can result to a significant crack formation and spallation of the thermal barrier coatings [5].

Furthermore, another shortcoming of YSZ is the higher temperature corrosion resistance property. Impurities from volcanic ash and dust can react with YSZ at elevated temperature. After reaction, the new phase has higher thermal conductivity and less strain tolerance [46]. Sulfur and vanadium from fossil based fuels can also plays a significant role in invalidating YSZ thermal barrier coatings at 600°C ~ 1000°C [47]. So alternative thermal barrier material is needed for higher working temperature.

1.2.2. Pyrochlore materials

Lanthanide zirconates with the pyrochlore structure were firstly discovered as a promising thermal barrier material due to their high phase stability at higher temperature. Phase diagrams of Gd_2O_3-ZrO_2 and Sm_2O_3-ZrO_2 are shown in Figure 1.7 and Figure 1.8 separately. For Gd_2O_3-ZrO_2 system, $Gd_2Zr_2O_7$ with pyrochlore structure can stand stable up to 1500°C and for Sm_2O_3-ZrO_2 system, the stable temperature can be 1900°C for pyrochlore structure, which is much higher than the current working temperature. Thus, the absence of volume change associated with phase transformation helps to improve the coating's service life.

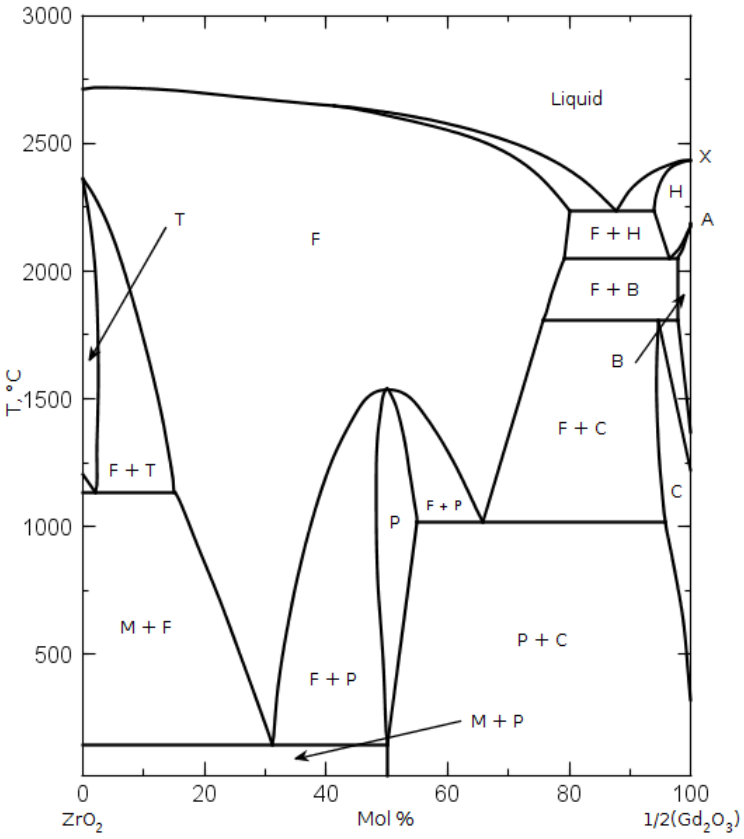

Figure 1.7 Gd_2O_3-ZrO_2 phase diagram. T = tetragonal, F = Cubic fluorite, M = monoclinic, P = pyrochlore, C, B, H = Gd_2O_3 phases [48].

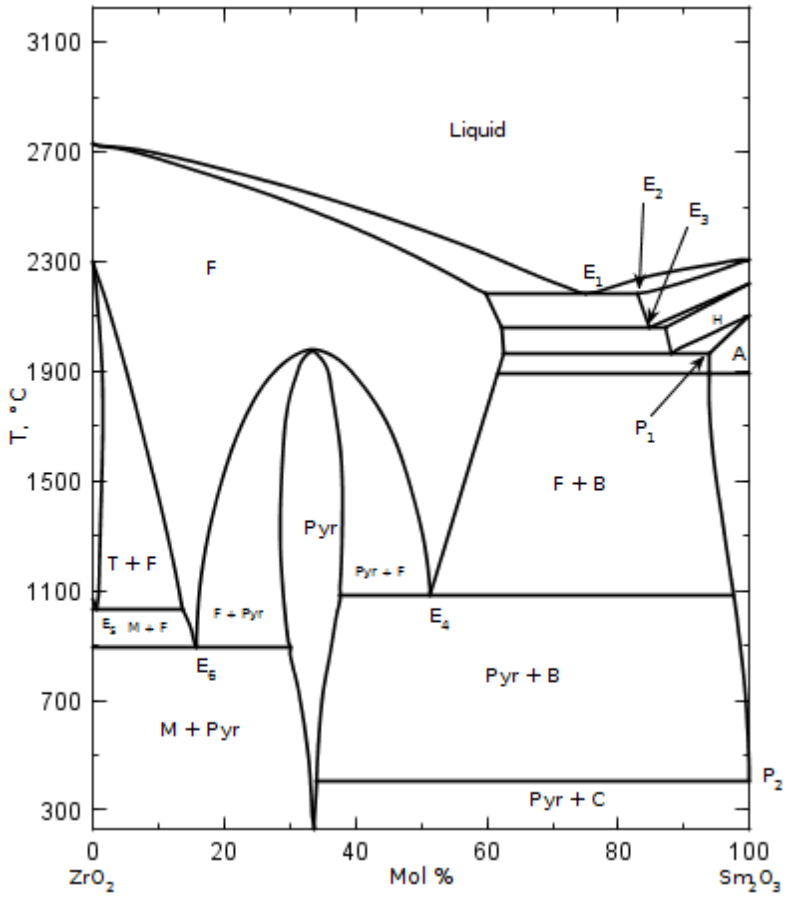

Figure 1.8 $SmO_{1.5}$-ZrO_2 phase diagram. T = tetragonal, F = cubic fluorite, M = monoclinic, Pyr = pyrochlore, C, B, H = Sm_2O_3 phases [49].

The pyrochlore structure is related to fluorite structure with formula of $A_2B_2O_7$ is a kind of complex crystal structure, where A is trivalent cations and B is tetravalent cations. Figure 1.9 and Figure 1.10 show the schematic figures of pyrochlore and fluorite crystal structures, respectively. Compared to fluorite structure, there is an oxygen vacancy at position (¾, ¼, ¼) in the 1/8 sub-unit cell of the pyrochlore structure. The difference of ion size between lanthanide ions and zirconium ions is larger than that of 7YSZ, which produces more vacancies. Both the vacancies caused by ion size difference and oxygen vacancy can lead to lower mean free path of phonons, and then lower thermal conductivity.

The thermal conductivity of several lanthanide zirconates with pyrochlore structure is shown in Table 1.1. Compared with 7YSZ in 1.5~2.3 $W \cdot m^{-1} \cdot K^{-1}$(see 1.2.1), pyrochlore materials show relatively lower thermal conductivity.

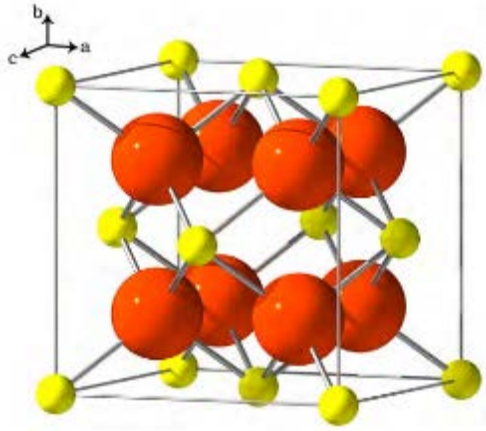

Figure 1.9 Cubic fluorite structure in AO_2 formula. Red balls represent O^{2-} ions and small yellow balls represent A^{4+} ions [50].

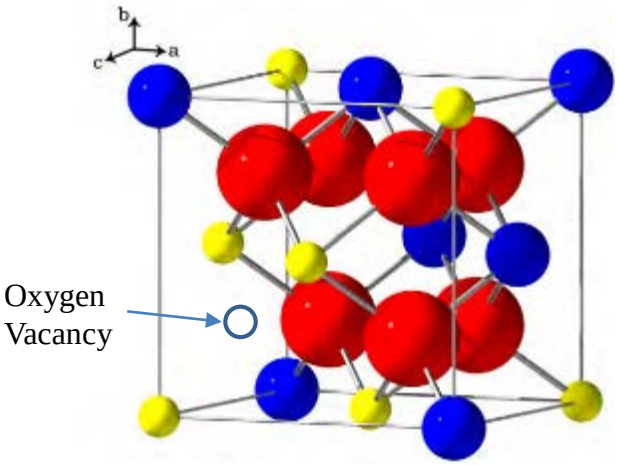

Figure 1.10 Sub-unit cell of pyrochlore structure in $A_2B_2O_7$ structure. Red balls represent O^{2-} ions. Blue balls and small yellow balls are A^{3+} and B^{4+} ions separately [50].

Table 1.1 Thermal conductivities of some pyrochlore materials (in $W \cdot m^{-1} \cdot K^{-1}$)

	Thermal conductivity at 800°C	Thermal conductivity at 1200°C
$La_2Zr_2O_7$ [51]	1.6	1.65
$Nd_2Zr_2O_7$ [52]	1.25	1.4
$Sr_2Zr_2O_7$ [53]	2.1	2.25
$Eu_2Zr_2O_7$ [54]	1.55	1.6

1.3. Failure of thermal barrier coatings

The operating temperature in gas turbine engines could be even higher than the melting point of superalloy blades, so any tiny failure of thermal barrier coatings can cause severe problems. Failure of thermal barrier coatings are caused by stress, strain and corrosion during thermal cycling.

1.3.1. Residual stress and strain

The residual stress in thermal barrier coating mainly comes from the mismatch thermal expansion coefficient between ceramic coatings and superalloy substrates during thermal cycling. The superalloy substrate (IN738) has a thermal expansion coefficient in $16\times10^{-6}K^{-1}$ and the NiAlPt bond coat has a CTE in $15\times10^{-6}K^{-1}$ at 1000°C[5, 55]. However, 7YSZ has a CTE as low as $10.3\times10^{-6}K^{-1}$ at 1000°C [51]. Pyrochlore materials have a CTE even lower than $10\times10^{-6}K^{-1}$ [52]. Lower thermal expansion coefficient in thermal barrier coatings can cause compressive residual stress in thermal cycling as is in Figure 1.11. The thermal barrier coating is deposited at around 260°C~540˚C (500°F~1000˚F), so the compression in TBC caused by manufacturing is really small compared with the working temperature (>1200˚C). Residual stress measured by laser-spectroscopic method can be

3~6 GPa in thermal barrier coatings and this compressive stress is much smaller than thermal stress, which is the origin of residual stress [34, 56]. Thus, cracks can form in the thermal cycling and after some cycles of forming and relaxation of compressive stress, cracks can accumulate and propagate to the edge of thermal barrier coatings, which can result to spall off of the coatings. This process is shown in Figure 1.12.

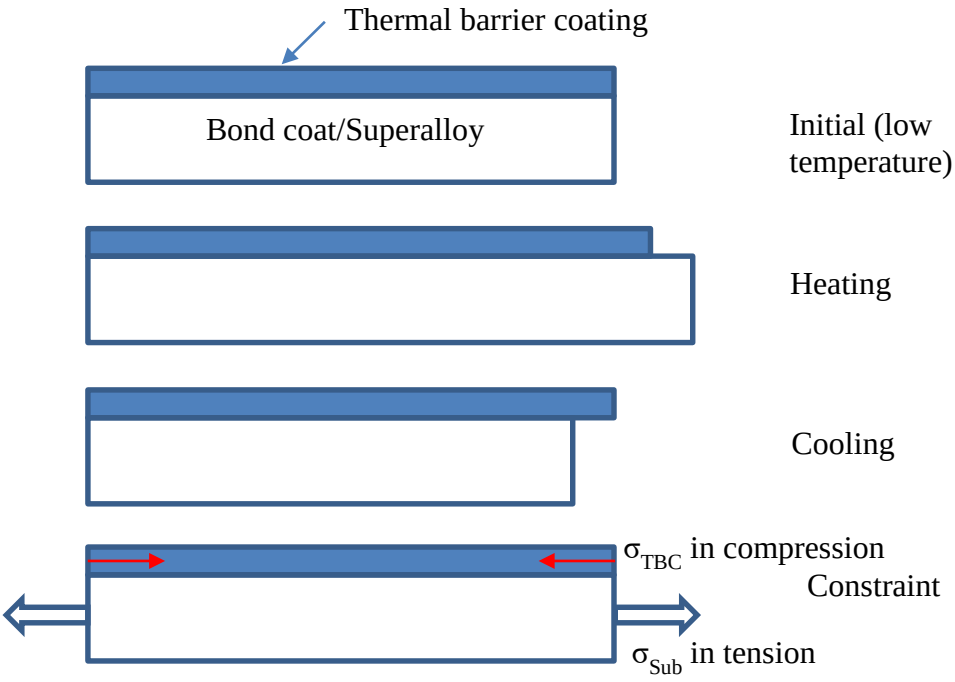

Figure 1.11 Schematic figure of strain and stress in thermal cycling.

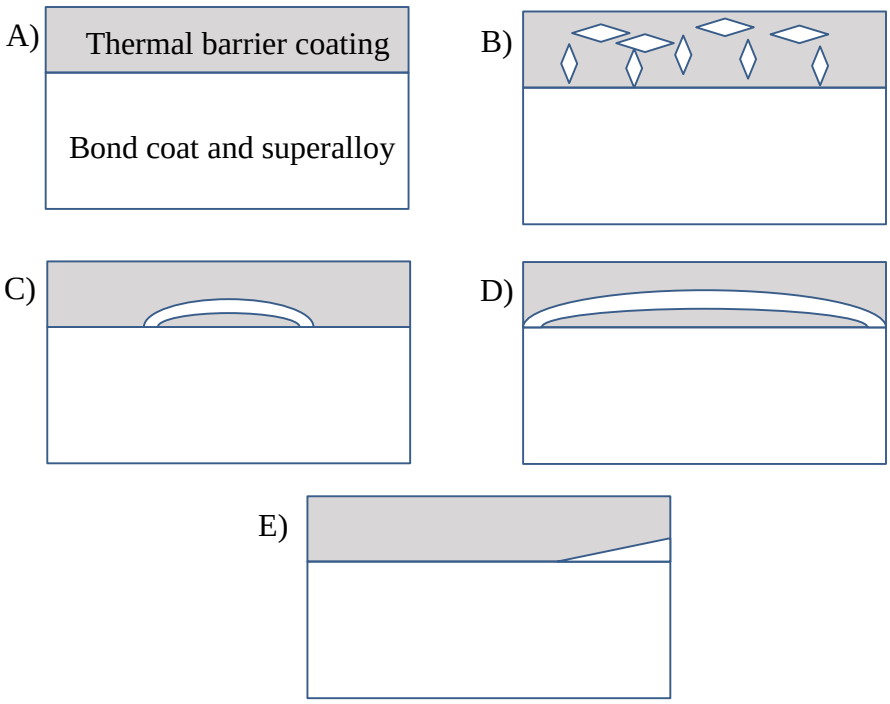

Figure 1.12 Spallation off process of thermal barrier coating. A) is initial state; B) is cracks start to form in thermal cycling; C) is accumulation of cracks; D) represents cracks propagate to the edge of coatings; E) is the thermal barrier coating spall off from substrate in the edge.

Although YSZ thermal barrier coatings can persist thousands of hours without failure, it is still worth to pursue longer thermal cycling lifetime by increasing the thermal expansion coefficient of thermal barrier materials. 30 mol% CeO_2 added in zirconates can increase thermal expansion coefficient from $8\times10^{-6}K^{-1}$ to $12.5\times10^{-6}K^{-1}$ at 800°C [57]. The CTE of $La_2Ce_2O_7$ can even reach $13\times10^{-6}K^{-1}$ at 1000°C [58], which is much closer to the CTE of bond coat and superalloy and helps to increase the lifetime.

1.3.2. TGO growth stress

Thermal grown oxide layer grows in the working temperatures. Once the TGO grows over some certain thickness, the thermal barrier coatings may spall off. Mostly the

TGO is originated from bond coat and forms at the interface of thermal barrier coating and bond coat. Al from MCrAlY (M=Ni and/or Co) would form dense α-Al_2O_3 to protect further oxygen diffusion [32]. Additionally, Cr and Ni in the bond coat can also form chromia and/or nickel oxide along with formation of α-Al_2O_3, especially in air plasma spray thermal barrier coatings[59-61]. The growth of the mixed oxide layer can lead to spalling of the thermal grown oxide [62, 63].

Weight change test is usually used to characterize the growth of TGO in thermal cycling. Figure 1.13 shows a typical growth of thermal grown oxide. This illustrates temperature plays a significant role in TGO growth. At lower temperature as 980°C, TGO still grows, but the growth rate was much lower than the rate at higher temperature and the growth time was much longer than 100 hours; while at higher temperature as 1200°C, TGO still kept growing after 140 hours' exposure, and the thickness was also much higher than the TGO exposed at lower temperature.

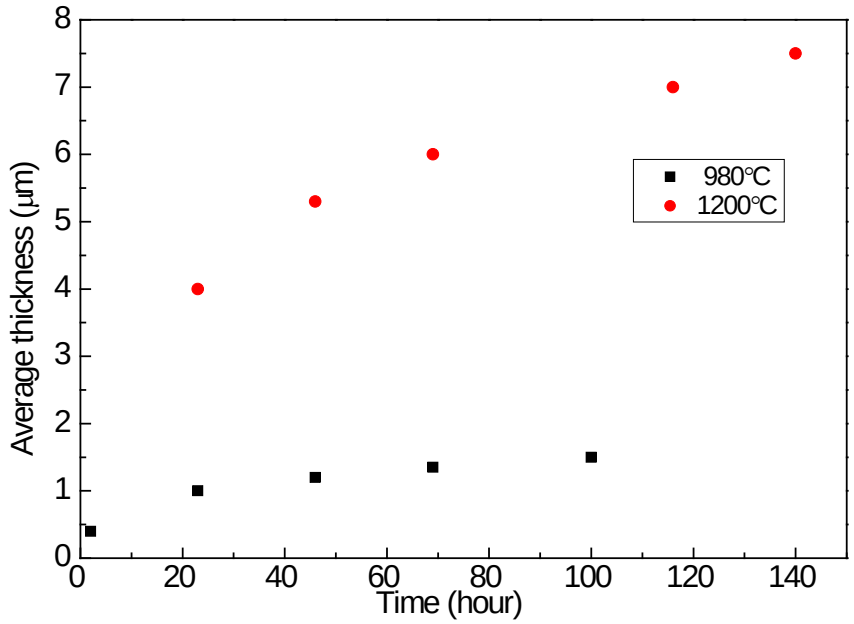

Figure 1.13 Average thickness of thermal grown oxide for Ni-22Cr-10Al-Y (wt%) bond coat, data from [64].

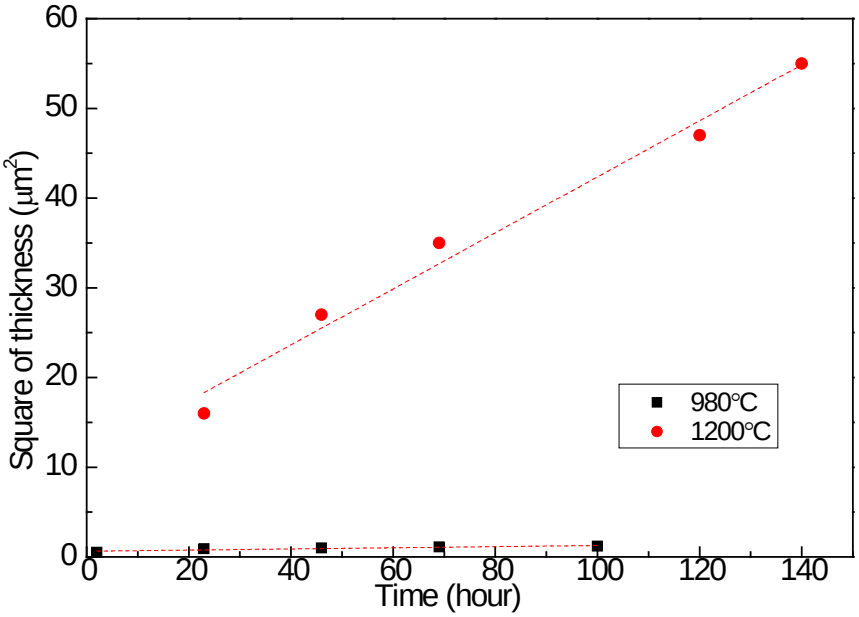

Figure 1.14 Square of thickness of thermal grown oxide for Ni-22Cr-10Al-Y (wt%) bond coat, data from [64].

Figure 1.14 shows the square value of thickness along with the thermal exposure time. This illustrates the square of Al_2O_3 layer's thickness has a linear relationship as the exposure time and at higher temperature as 1200°C, the cracks propagate at a much higher rate than 980°C.

Recent research found that nanostructured NiCrAlY bond coats presents higher stability than micro structured bond coat [65, 66]. Nanostructured NiCrAlY has higher activity in forming α-Al_2O_3 due to Al has a higher activity than Cr. The dense α-Al_2O_3 can prevent further growth of oxide layer. Although nanostructured bond coat could elongate the lifetime of thermal barrier system, it is difficult to manufacture. Nano powders have a higher adhesion property and higher volts is applied to feed the powders into plasma [67].

1.3.3. CMAS corrosion on thermal barrier coatings

Dust and ash from air could be injected and melted in the gas turbine engines and react with thermal barrier coatings. The main composition of the pollutant is CaO-MgO-Al_2O_3-SiO_2 (CMAS) and the ratio may change between different sources. Molten CMAS can penetrate through the pores and cracks that are connected to the surface during thermal cycling. Thus, thermal barrier coatings made by EB-PVD that have vertical columnar and pores that may be easier to penetrate.

Composition of CMAS varies throughout the earth and but the corrosion mechanism is similar for different composition [68, 69]. Firstly, the CMAS melts in the engines and penetrates the coatings through the pores and cracks in the coatings and then solidifies in the pores. Then the solid CMAS can reduce the tolerance of thermal stress tremendously. The eutectic CaO-MgO-Al_2O_3-SiO_2 has a melting point as low as 1240~1260°C, which is much lower than the individual constituent (1600°C~2852°C). So

the molten CMAS can cause severe problems that the individual constituent cannot. Any open pores in thermal barrier coatings are sensitive for CMAS penetration due to its excellent wetting property above melting point [70, 71]. Recent research shows that the penetration of CMAS can be initiated as low as 4.8 mg/cm^2 at 1300°C [72].

Furthermore, the new phase formation after CMAS corrosion presents dense microstructure and results to loss tolerance of thermal stress, which leads to spall off the coatings, especially for YSZ thermal barrier coatings [73]. However, recent research found that some materials can dissolve in CMAS and re-precipitate into different phases and morphology, and the new phases may present good corrosion resistance, especially for lanthanide zirconates [71]. $2ZrO_2 \cdot Y_2O_3$ also present this property. After reaction, cubic fluorite ZrO_2 and Ca-Y crystal apatite formed after reaction [74].

According to recent research, two ways are applied to prevent CMAS attack. First method is to make an overlay coatings on top of thermal barrier coating to prevent CMAS penetration. Al_2O_3 layer in dense, uniform and crack-free structure produced by electrophoretic deposition (EPD) could prevent CMAS attack for air plasma sprayed YSZ thermal barrier coatings. Increase Al amount in CMAS can accelerate the crystallization and lead to form anorthite platelets and $MgAl_2O_4$ spinel [75]. The second way to slow down CMAS degradation is to find new promising thermal barrier materials. Lanthanide zirconates with the pyrochlore structure meet this demand. Pyrochlore materials could react with CMAS easily and then form a dense and protective layer to prevent further CMAS attack [76].

1.3.4. Sulfur corrosion on thermal barrier coatings

Sulfur impurities from fossil fuels can similarly corrode thermal barrier coatings at lower temperature than CMAS corrosion. Currently applied YSZ thermal barrier coating presents destructive phase transformation to m-ZrO_2 through the reaction of molten sulfate and thermal barrier materials [77]. Sulfur corrosion accompanied with vanadium oxide. Usually, thermal barrier coatings are attacked by sodium sulfate (Na_2SO_4) and vanadium oxide (V_2O_5) and several mechanisms presents in sulfur and vanadium corrosion due to the temperature difference. The melting point of Na_2SO_4 and V_2O_5 are 884°C and 690°C separately, so the corrosion caused by sulfur and vanadium could be more active than CMAS corrosion. The main mechanism is the dissolution of YSZ in melting depositions and the re-precipitation could form new phase and change the volume to reduce both the chemical corrosion resistance and tolerance of residual stress. Current research shows that only Na_2SO_4 itself does not have obvious attack on thermal barrier materials, both for YSZ and pyrochlore materials [47].

1.3.4.1. V_2O_5 corrosion only

The reaction mechanism of YSZ and V_2O_5 could be divided by 747°C [47]. When the temperature is below 747°C, the molten V_2O_5 reacts with ZrO_2 as the equation 1-1 shows. So V_2O_5 could accelerate the formation of metastable t'-ZrO_2 phase and reduce the tolerance of residual stress [78].

$$ZrO_2\ (s) + V_2O_5\ (l) \rightarrow ZrV_2O_7\ (s) + t'\text{-}ZrO_2 \qquad (1\text{-}1)$$

When the temperature is above 747°C, ZrV_2O_7 melts and decomposed to ZrO_2 (solid) and V_2O_5 (liquid) [79]. Then the predominant reaction is between Y_2O_3 in YSZ and V_2O_5 and the product is YVO_4 and m-ZrO_2. The reaction is shown in 1-2. YVO_4 has a

stable phase up to 1810°C and remove yttrium from the YSZ, and thus, the stability of YSZ is reduced [80].

$$Y_2O_3\ (s) + V_2O_5\ (l) \rightarrow 2YVO_4\ (s) + m\text{-}ZrO_2 \quad (1\text{-}2)$$

1.3.4.2. V_2O_5 and Na_2SO_4 mixture corrosion

It is believed that only Na_2SO_4 would not react with thermal barrier materials [81]. But when Na_2SO_4 is accompanied with SO_3 at higher partial pressure, the SO_3 could react with yttria and form $Y_2(SO_4)_3$ [82]. In addition, Na_2SO_4 mixed with V_2O_5 tends to form $NaVO_3$ as reaction 1-3 and 1-4 shows.

$$Na_2SO_4\ (l) \rightarrow Na_2O\ (l) + SO_3\ (g) \quad (1\text{-}3)$$

$$Na_2O\ (l) + V_2O_5\ (l) \rightarrow 2NaVO_3\ (l) \quad (1\text{-}4)$$

Then sodium vanadate has a low melting point at 610°C and could degrade YSZ as low as 700°C in reaction 1-5 [81, 83]. The reaction product Na_2O could react with V_2O_5 again and accelerate the degradation of YSZ. The phase diagram is shown in Figure 1.15. The Na_2SO_4 and V_2O_5 binary system has a melting point as low as 500°C, so it can degrade the YSZ coatings at a much lower temperature than molten CMAS [78, 84].

$$Y_2O_3\ (s) + 2NaVO_3\ (l) \rightarrow 2YVO_4\ (s) + m\text{-}ZrO_2 + Na_2O\ (l) \quad (1\text{-}5)$$

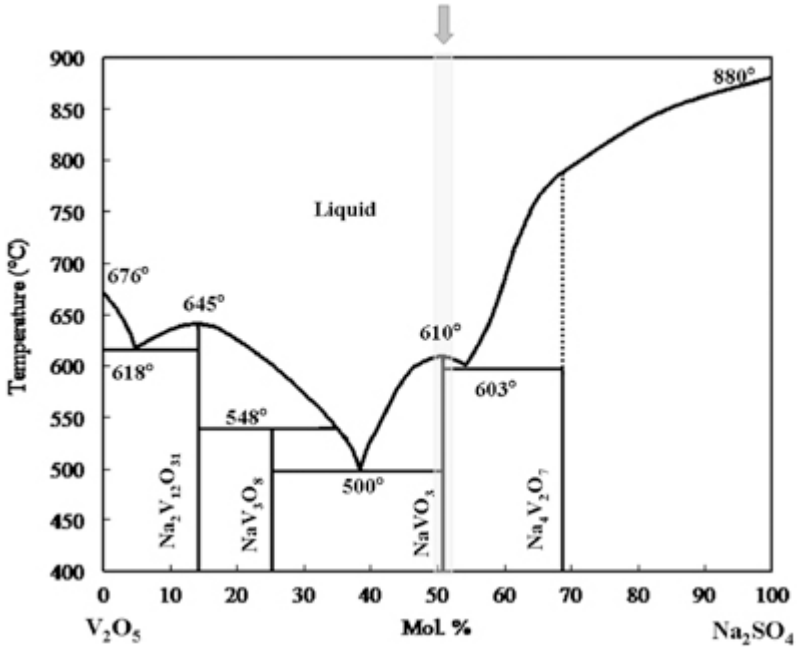

Figure 1.15 Phase diagram of Na_2SO_4-V_2O_5 mixture [85].

1.4. Research objective

The research objective of this project is understanding the reaction mechanism of CMAS corrosion on pyrochlore materials. Currently applied 7~8 wt% YSZ has been served as thermal barrier coatings for tens of years. However, the phase transformation from metastable t' phase to t phase and CMAS corrosion limits the potential to increase the working temperature. CMAS deposition accelerates transformation from t' phase to t phase in YSZ thermal barrier coatings [86]. Recent research shows pyrochlore materials present good properties in phase stability, thermal conductivity and thermal expansion coefficient [51-55]. Additionally, it is believed that pyrochlore materials have better CMAS corrosion resistance because the corrosion product will fill and seal the pores and then the apatite phase with high melting temperature will prevent further corrosion [87]. Although the experimental results were shown in some papers, the mechanism is not clearly understood.

This work focuses on the reaction mechanism of CMAS and pyrochlore materials, and the function of the reaction layer after CMAS deposition.

In study of reaction mechanism, pyrochlore materials would be dissolved in molten CMAS easily and precipitate into two phases – fluorite phase which is rich in zirconia and apatite phase which is rich in lanthanide silicates. The reaction mechanism has been studied via several valuables, i.e. microstructure, temperature, composition. The comparison of pyrochlore materials and YSZ will be studied to understand the reaction mechanism. $[Gd_XSm_{(1-x)}]_2Zr_2O_7$ and 7 wt% YSZ ceramics will be used in this research.

In study of function of the reaction layer after CMAS deposition, re-corrosion experiments will be applied to see the growth of reaction layer. The thickness of reaction layers before and after re-corrosion experiment are investigated and tracing atom was used to detect the thickness.

CHAPTER 2. Materials and Experimental

2.1. Materials Preparation

There are two ways to synthesize the pyrochlore materials: solid oxide sintering and co-precipitation. Solid oxide sintering method needs less steps while co-precipitation method has lower sintering temperature and good sintering result.

The 7YSZ used in this research is commercial YSZ purchased from Fuel Cell Materials (FCM) Inc.

2.1.1. Solid oxide sintering

In solid oxide sintering method, Gd_2O_3, Sm_2O_3 and ZrO_2 powders were weighed and mixed in stoichiometric amounts and ball milled in ethanol for 24 hours. After drying, the powders were pressed uniaxially under 100 MPa into pellets with the diameter of 12.7 mm, which would be sintered at a specific temperature and time. The heating ramp rate was varied to obtain different porosity and the cooling rate was no more than 400°C/hour. The whole process is summarized as Figure 2.1 shows.

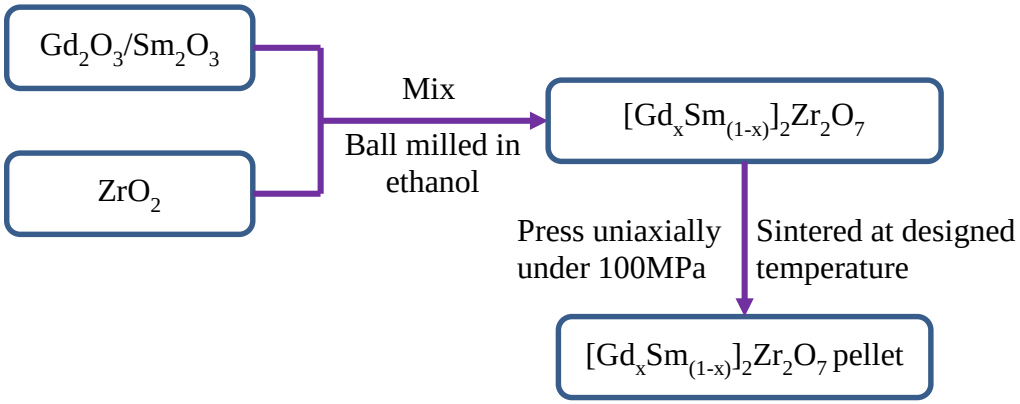

Figure 2.1 Process of solid oxide sintering in pyrochlore materials' preparation

2.1.2. Co-precipitation

Firstly, the $ZrOCl_2 \cdot 8H_2O$ was dissolved in deionized water. Gd_2O_3 or Sm_2O_3 in stoichiometric amounts was dissolved in nitric acid separately and then added to the $ZrOCl_2 \cdot 8H_2O$ aqueous solution. The resulting mixture was stirred for 30 minutes to obtain a homogeneous solution and an aqueous ammonia solution was added. The pH was kept above 10 in this step. The precipitate was washed with deionized water and dried at 150°C for 10 hours. After desiccation, the powders were heated to 800°C. 5 wt% PVA solution was used as binding agent. The amount of PVA used is 1% of total weight of dried powders. After grinding, the powders were sieved under mesh 40. Then the dried materials were pressed under 100 MPa into discs, which were sintered at the same temperature prepared by solid oxide sintering method. The whole process is summarized in Figure 2.2.

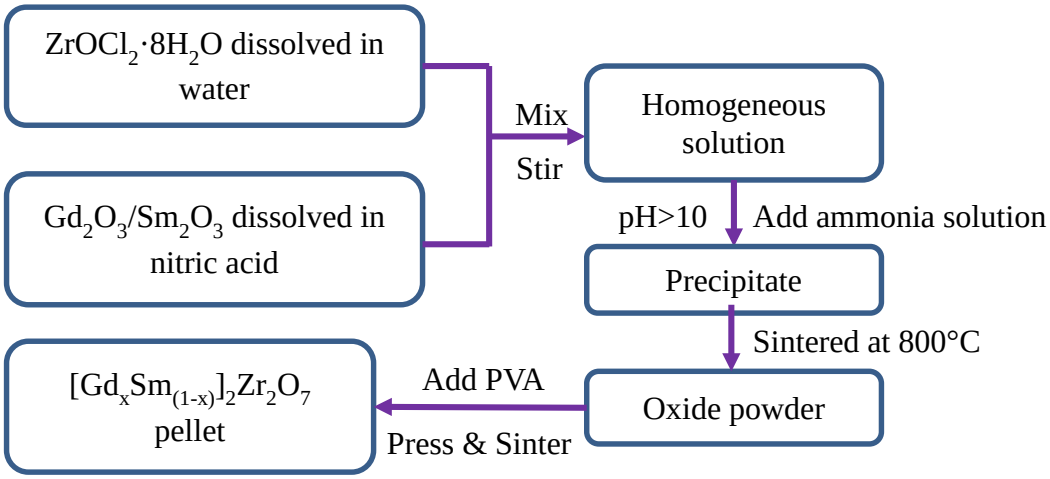

Figure 2.2 Process of co-precipitation method in pyrochlore materials' preparation

2.1.3. Corrosion materials

$CaO\text{-}MgO\text{-}Al_2O_3\text{-}SiO_2$ glass was used to simulate deposit ingested during application. Two compositions were used in this study and the compositions in molar percentage are in shown in Table 2.1 and Table 2.2. CMAS – 2 contains more Al than CMAS – 1 and the ratio of Ca:Mg:Si were the same. The glass in both composition has a melting point of around 1240°C to 1260°C. To synthesize the glass, powders for the constituent oxides in stoichiometric ratio were mixed and sintered at 1300°C for 5 hours to obtain a homogeneous glass. The glasses were crushed and ball milled for 24 hours to obtain fine glass particles.

Table 2.1. Composition of CMAS – 1 in molar percentage

CaO	33
MgO	9
$AlO_{1.5}$	13
SiO_2	45

Table 2.2. Composition of CMAS – 2 in molar percentage

CaO	29
MgO	8
$AlO_{1.5}$	23
SiO_2	40

2.2. Hot corrosion procedure

2.2.1. Corrosion on thermal barrier materials

The fine glass powders prepared in 2.1.3 were placed on top of pyrochlore discs and then sintered at different temperature from 1200°C to 1300°C. The amount used is 35 mg/cm^2. Figure 2.3 shows the corrosion setup for pellets.

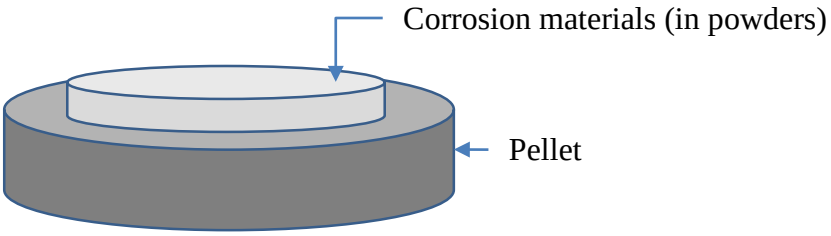

Figure 2.3 Schematic of CMAS and/or sulfate corrosion on pellets.

The effects of water flow on the corrosion behavior were also studied. Figure 2.4 shows the corrosion behavior setup for water flows. Corrosion at moisture atmosphere were studied at 1200°C and 1300°C. The water flow is driven by compressed air in pressure of 5 psi and the flow rate is calculated as 10ml/h.

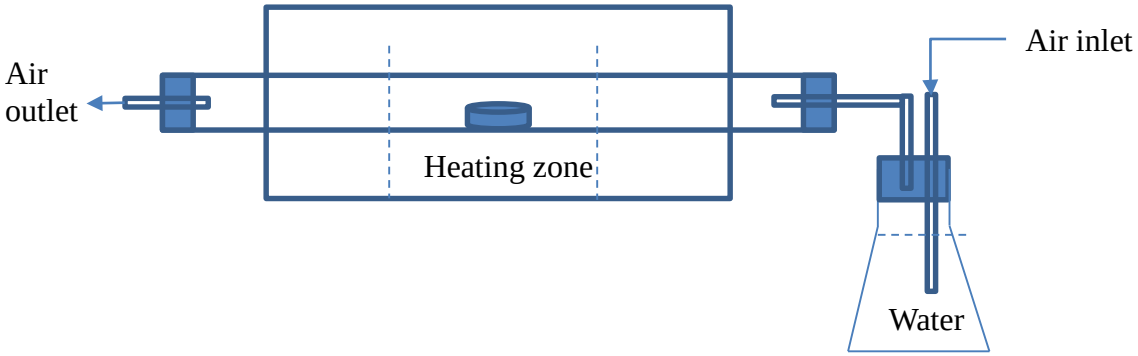

Figure 2.4 Setup for corrosion behavior in air with water flows.

2.3. Materials characterization

Phase analysis was performed by XRD using a Bruker D8 diffractometer with Cu X-ray source. The working current and voltage were 40 mA and 40 kV. Morphology and composition analyses were carried out using a JEOL JSM-7000F scanning electron microscope (SEM) equipped with energy dispersive X-ray spectroscopy (EDS). The location of iridium in the reaction layer was also determined by EDS. Thickness of reaction layer with iridium can also be determined by optical microscope.

2.4. Porosity measurement

Porosity is a critical parameter in thermal barrier coatings' property and it is determined by sintering temperature, sintering durations and ramp rate. In this study, both apparent porosity and total porosity were tested. Slower ramp rate in the sintering procedure was used to obtain lower porosity. The porosity used in this work is apparent porosity, namely the pores that connected to the surface.

Apparent porosity was tested according to ASTM C20-00. Firstly, put the specimens in water and boil for 2 hours. During boiling, the specimens should be totally

immersed in water and no contact with the container's bottom. After boiling, the specimens were cooled in water and immersed in water at least 12 hours. Then the saturation weight, *W*, was determined after remove the water in the surface. After saturation weight was determined, the specimens were placed in 110°C for 5 hours to make sure the specimens were totally dried. Then the dry weight, *D*, was determined in 4 decimal in grams. Because the samples were pressed into pellets, the volume of the specimens could be determined easily by measuring the dimension *d* and thickness *h*. Then the apparent porosity, P_1, would be obtained according to equation 2-1 to 2-3.

$$\text{Volume of open pores, cm}^3 = W - D \tag{2-1}$$

$$\text{Volume of specimen, cm}^3 = \pi \times (d/2)^2 \times h \tag{2-2}$$

$$\text{Apparent porosity, P} = (W - D)/[\ \pi \times (d/2)^2 \times h] \tag{2-3}$$

CHAPTER 3. Morphology and property of pre-corrosion materials

3.1. Surface morphology of pyrochlore materials

As mentioned in section 2.1.1 and 2.1.2, pyrochlore materials are prepared by two ways: solid oxide sintering method and co-precipitation method. The different conditions tends to form various surface morphologies and properties.

3.1.1. Solid oxide sintering method

The surface morphologies of $Gd_2Zr_2O_7$ and $Sm_2Zr_2O_7$ prepared by solid oxide sintering method at 1500°C for 5 hours is shown in Figure 3.1. It is illustrated that both $Gd_2Zr_2O_7$ and $Sm_2Zr_2O_7$ specimens prepared by solid oxide sintering did not have uniform grains distribution. The grains are divided into two sizes: the smaller grains are around 0.5 μm and the larger grains are around 2~3 μm. Furthermore, the results of elemental distribution of $Gd_2Zr_2O_7$ and $Sm_2Zr_2O_7$ collected by EDS are shown in Figure 3.2 and Figure 3.3, respectively. The EDS data explains that the specimens prepared by solid oxide sintering has non uniform elemental distribution as well both in $Gd_2Zr_2O_7$ and $Sm_2Zr_2O_7$. The grains are divided into two phases: Gd/Sm-rich phase and Zr-rich phase.

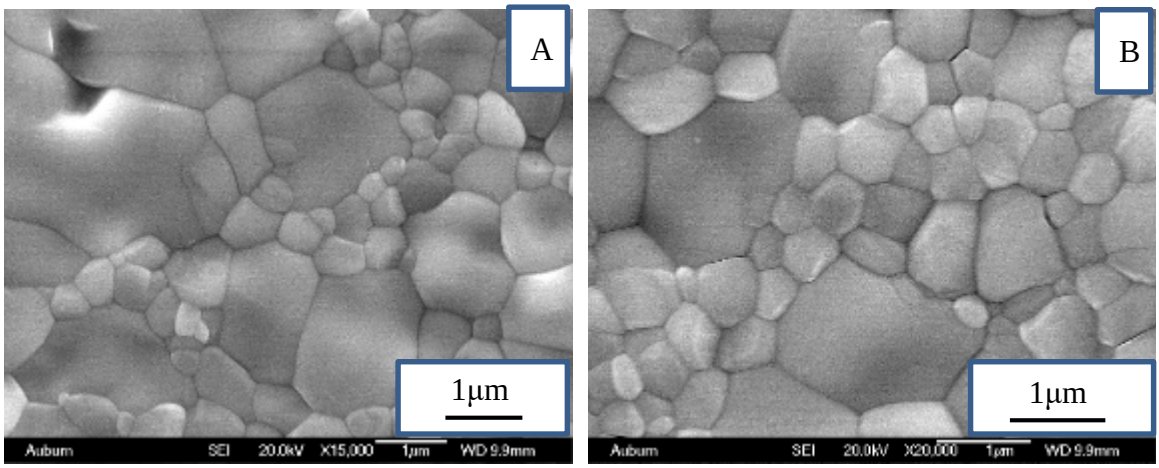

Figure 3.1 Surface morphology of $Gd_2Zr_2O_7$ and $Sm_2Zr_2O_7$ prepared by solid oxide sintering method at 1500°C for 5 hours. A) is $Gd_2Zr_2O_7$ and B) is $Sm_2Zr_2O_7$.

3.1.2. Co-precipitation method

The surface morphology of $Gd_2Zr_2O_7$ and $Sm_2Zr_2O_7$ prepared by co-precipitation method at 1500°C for 5 hours is shown in Figure 3.4. Compared to the surface morphology prepared by solid oxide sintering shown in Figure 3.1, the pyrochlore specimens prepared by co-precipitation present smaller and more uniform in grain size around 1 μm. The elemental distribution data of $Gd_2Zr_2O_7$ and $Sm_2Zr_2O_7$ are shown in Figure 3.5. Compared to Figure 3.2 and Figure 3.3, specimens prepared by co-precipitation method have uniform elemental distribution as well as grain size. The ratio of Gd/Sm : Zr is close to 1:1. In addition, the XRD pattern of $Gd_2Zr_2O_7$ and $Sm_2Zr_2O_7$ prepared by co-precipitation at various conditions are shown in Figure 3.6 and Figure 3.7. Higher sintering temperature has strong peaks, which illustrates that higher sintering temperature accelerate the grain growing and get a larger grains. All the peaks can be indexed to $Gd_2Zr_2O_7$ and $Sm_2Zr_2O_7$ pyrochlore ceramic according to JCPDS card (#01-075-8269 for $Gd_2Zr_2O_7$ and #00-024-1012 for $Sm_2Zr_2O_7$). The peaks indexed as (311), (331) and (511) can be used to tell the

difference from pyrochlore structure to cubic fluorite structure according to JCPDS card (#01-080-0471 for fluorite $Gd_2Zr_2O_7$ and #01-078-1291 for fluorite $Sm_2Zr_2O_7$).

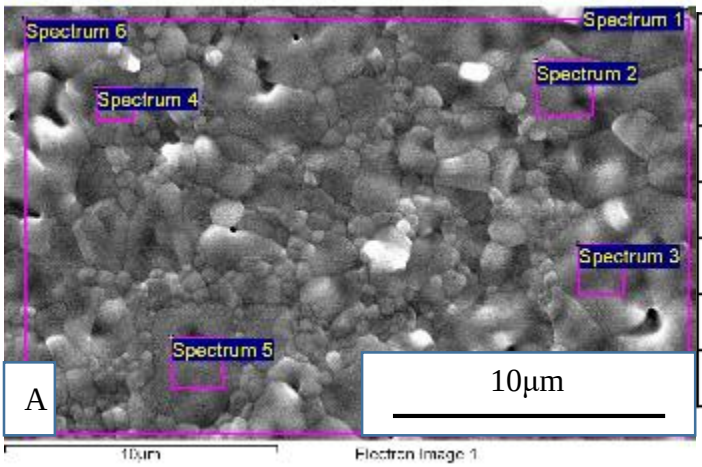

Spectrum #	Gd	Zr
1	8	42
2	6	36
3	8	45
4	6	42
5	7	40
6	6	40

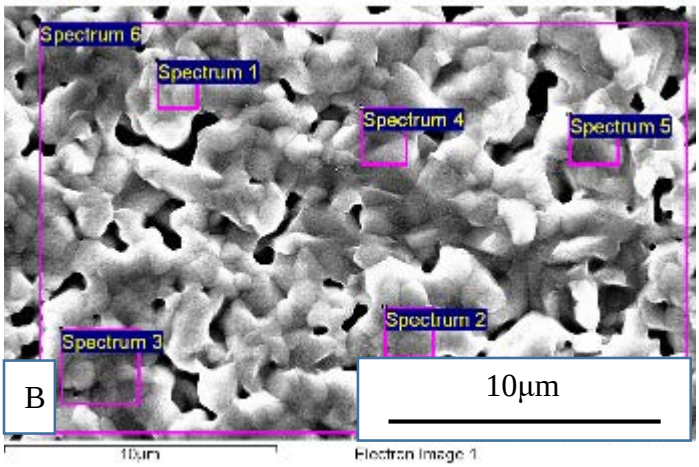

Spectrum #	Gd	Zr
1	39	
2	34	
3	34	
4	32	9
5	36	
6	33	7

Figure 3.2 Elemental distribution result of $Gd_2Zr_2O_7$ prepared by solid oxide sintering method (in atomic ratio).

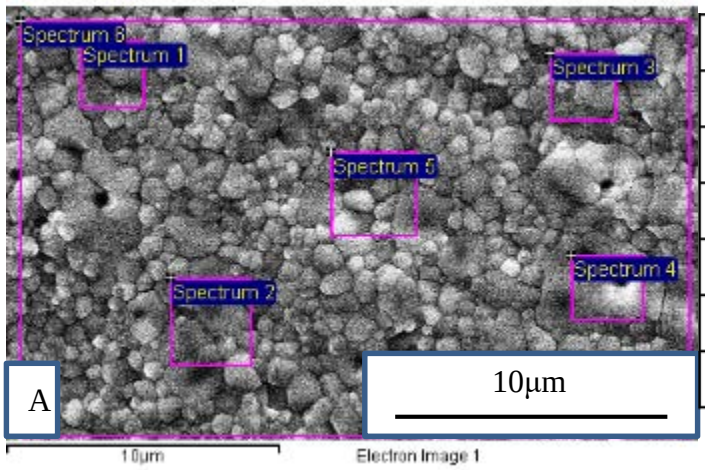

Spectrum #	Sm	Zr
1	5	36
2	4	37
3	3	38
4	6	34
5	4	37
6	3	38

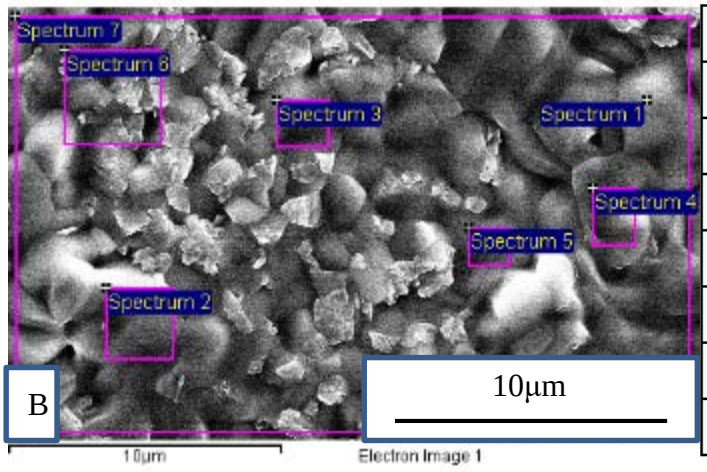

Spectrum #	Sm	Zr
1	26	10
2	23	10
3	23	10
4	29	11
5	28	10
6	26	6
7	26	8

Figure 3.3 Elemental distribution result of $Sm_2Zr_2O_7$ prepared by solid oxide sintering method (in atomic ratio).

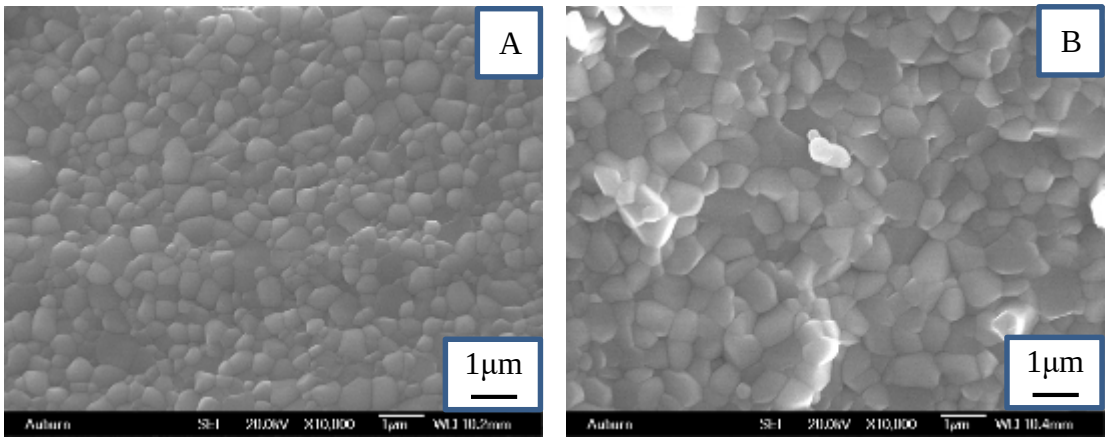

Figure 3.4 Surface morphology of $Gd_2Zr_2O_7$ (A) and $Sm_2Zr_2O_7$ (B) prepared by co-precipitation method at 1500°C for 5 hours.

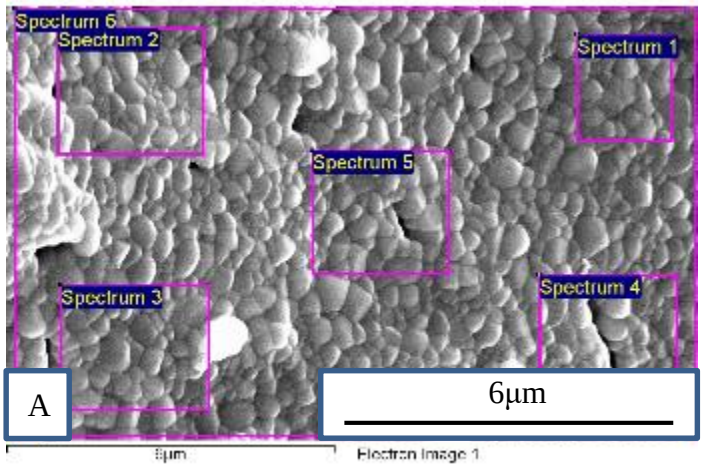

Spectrum #	Gd	Zr
1	14	17
2	15	17
3	13	16
4	13	15
5	14	16
6	13	16

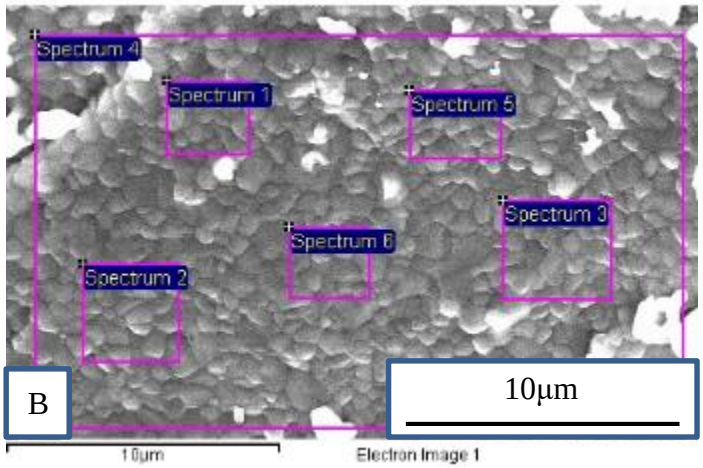

Spectrum #	Sm	Zr
1	15	18
2	14	18
3	14	18
4	14	17
5	14	17
6	14	18

Figure 3.5 Elemental distribution of $Gd_2Zr_2O_7$ (A) and $Sm_2Zr_2O_7$ (B) prepared by co-precipitation at 1500°C for 5 hours (in atomic ratio).

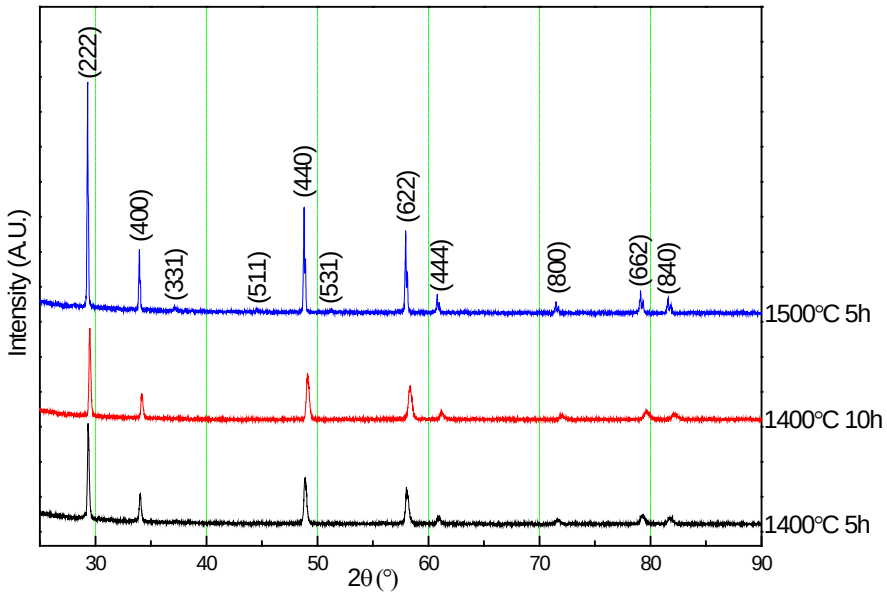

Figure 3.6 XRD pattern of $Gd_2Zr_2O_7$ prepared at different temperatures by co-precipitation method.

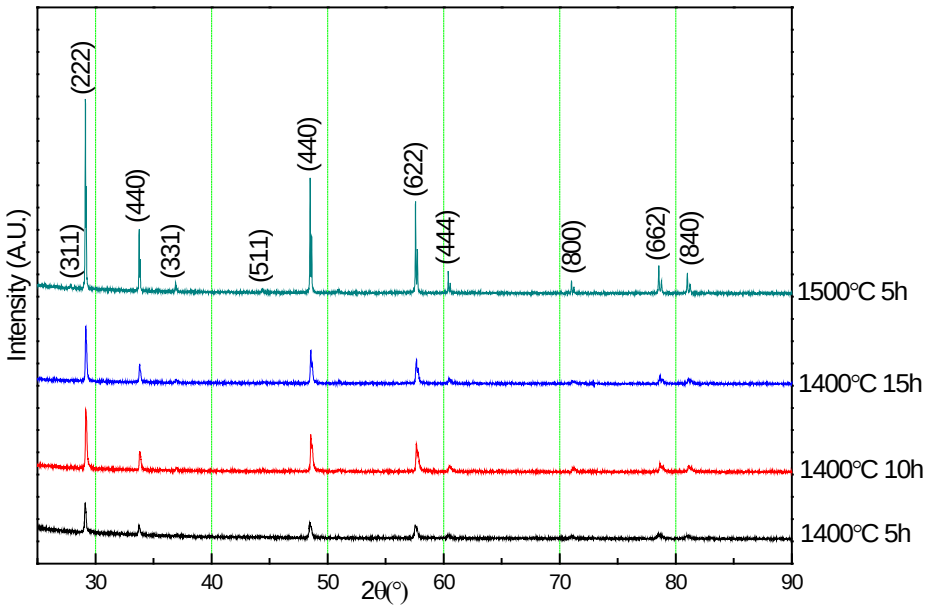

Figure 3.7 XRD pattern of $Sm_2Zr_2O_7$ ceramic prepared by co-precipitation method and sintered at various conditions.

3.2. Porosities of pyrochlore materials

The pyrochlore materials were sintered at 1500°C with three different ramp rates. The relationship of porosity and sintering conditions is shown in Table 3.1.

Table 3.1. Relationship of apparent porosity and sintering conditions

Ramp rate	400°C/hour	600°C/hour	800°C/hour
$Gd_2Zr_2O_7$	19%	23%	31%
$Sm_2Zr_2O_7$	13%	19%	29%

3.3. YSZ property

The XRD pattern of YSZ is shown in Figure 3.8. Every peak can be indexed according to JCPDS card #030-1468 in cubic fluorite phase.

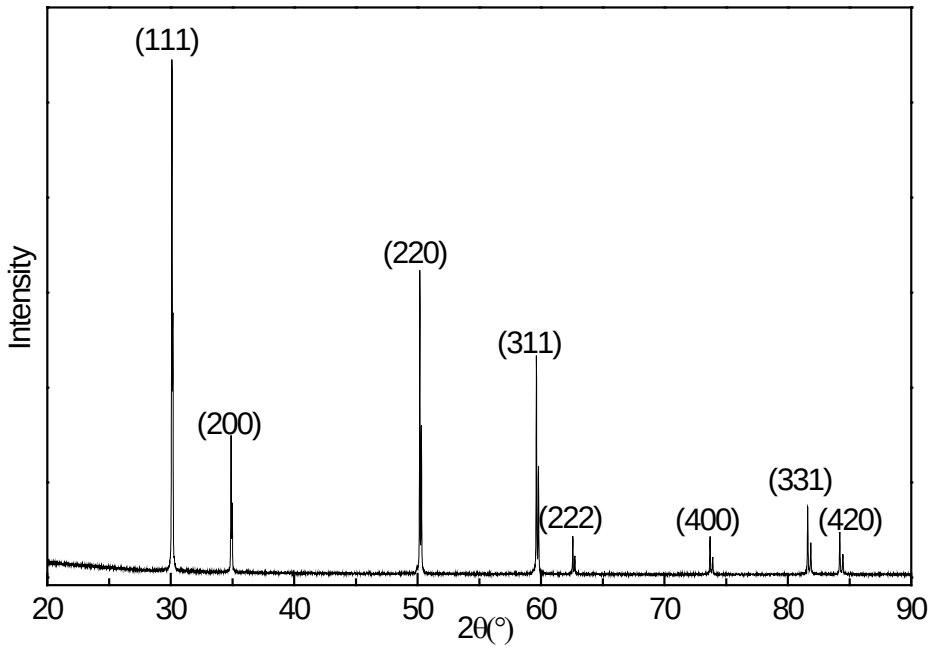

Figure 3.8 XRD pattern of commercial YSZ

3.4. CMAS property

CMAS mixture was sintered at 1300°C (above the melting point around 1240°C to 1260°C) to obtain a uniform phase. After sintering, the powders transformed to transparent and uniform glass, which can explain the reaction mechanism more clearly. Then the transparent glass was crushed and ball milled to acquire the uniform glass powders. Figure 3.9 shows the XRD pattern of CMAS glass powder and transparent glass bulk. No peaks appeared both in CMAS powders and CMAS bulk, which means the CMAS materials remained as amorphous glass phase after sintering. It helps to identify the phases after corrosion test and all the phases after corrosion with CMAS would be the reaction product.

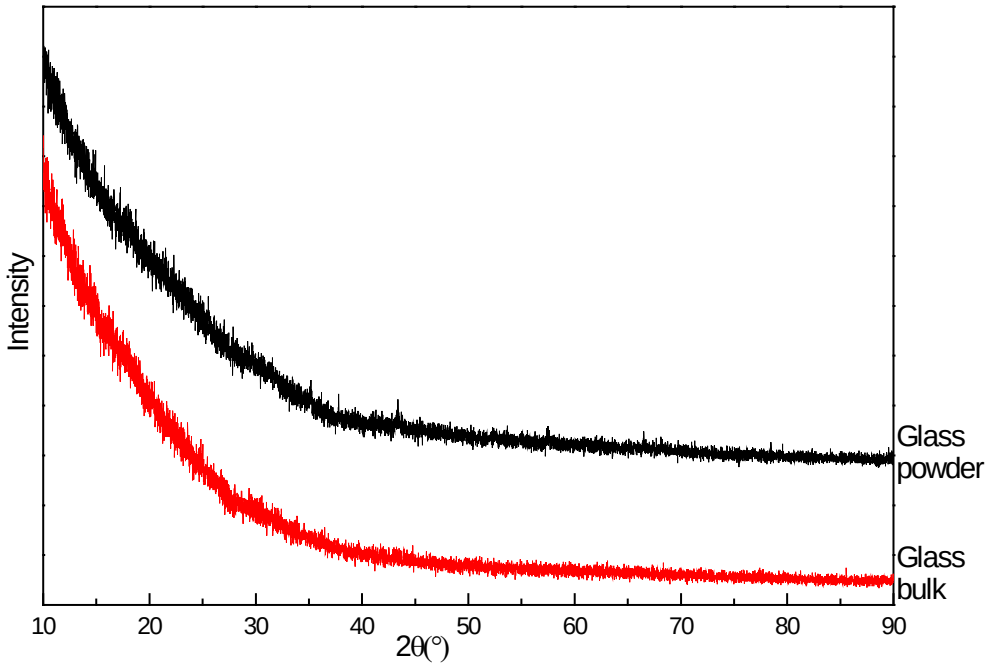

Figure 3.9 XRD pattern of CMAS glass bulk and glass powder.

3.5. Discussion and conclusion

Pyrochlore specimens prepared by co-precipitation present uniform morphology both in grain size and elemental distribution than solid oxide sintering method. In solid oxide sintering method, the raw oxide materials are ball milled but cannot reach to the same uniformity as co-precipitation method and it needs higher sintering temperature and much longer sintering duration to get uniform morphology. While in co-precipitation method, all the precipitations come from the ions and can form uniform distribution in elemental distribution. The fine particles prepared in co-precipitation method contribute to forming uniform and smaller grains. To simulate better working conditions, the specimens prepared by co-precipitation method are used for the corrosion test.

CHAPTER 4. CMAS corrosion properties of thermal barrier materials

CMAS has a melting point around 1240°C~1260°C due to its glass phase and difference in composition. It is reasonable to believe that the materials would present different properties below and above CMAS melting point. So the CMAS corrosion resistance property is studied at low temperature (<1250°C) and high temperature (>1250°C). The composition of CMAS used in this chapter was CMAS – 1 if not specified (composition see 2.1.3).

4.1. High temperature (>1250°C) CMAS corrosion property

4.1.1. Reaction product after corrosion at high temperature

The surface morphology of $Gd_2Zr_2O_7$ and $Sm_2Zr_2O_7$ in low porosity (19% and 13% separately) after CMAS – 1 exposure at various temperatures are shown in Figure 4.1 and Figure 4.2 respectively. After CMAS corrosion, a new phase in long stick shape formed. Furthermore, higher corrosion temperature presented larger grains. For $Gd_2Zr_2O_7$ in Figure 4.1, the length of new phase was around tens of microns after corrosion at 1500°C and less than 10 microns after corrosion at 1300°C. The other rest phase formed round shape grains and their size was in the same scale as the long stick phase. For $Sm_2Zr_2O_7$ in Figure 4.2, the length of the new phase did not change as much as $Gd_2Zr_2O_7$ and dropped around 10 μm. The size of round shape phases was uniform and around several microns.

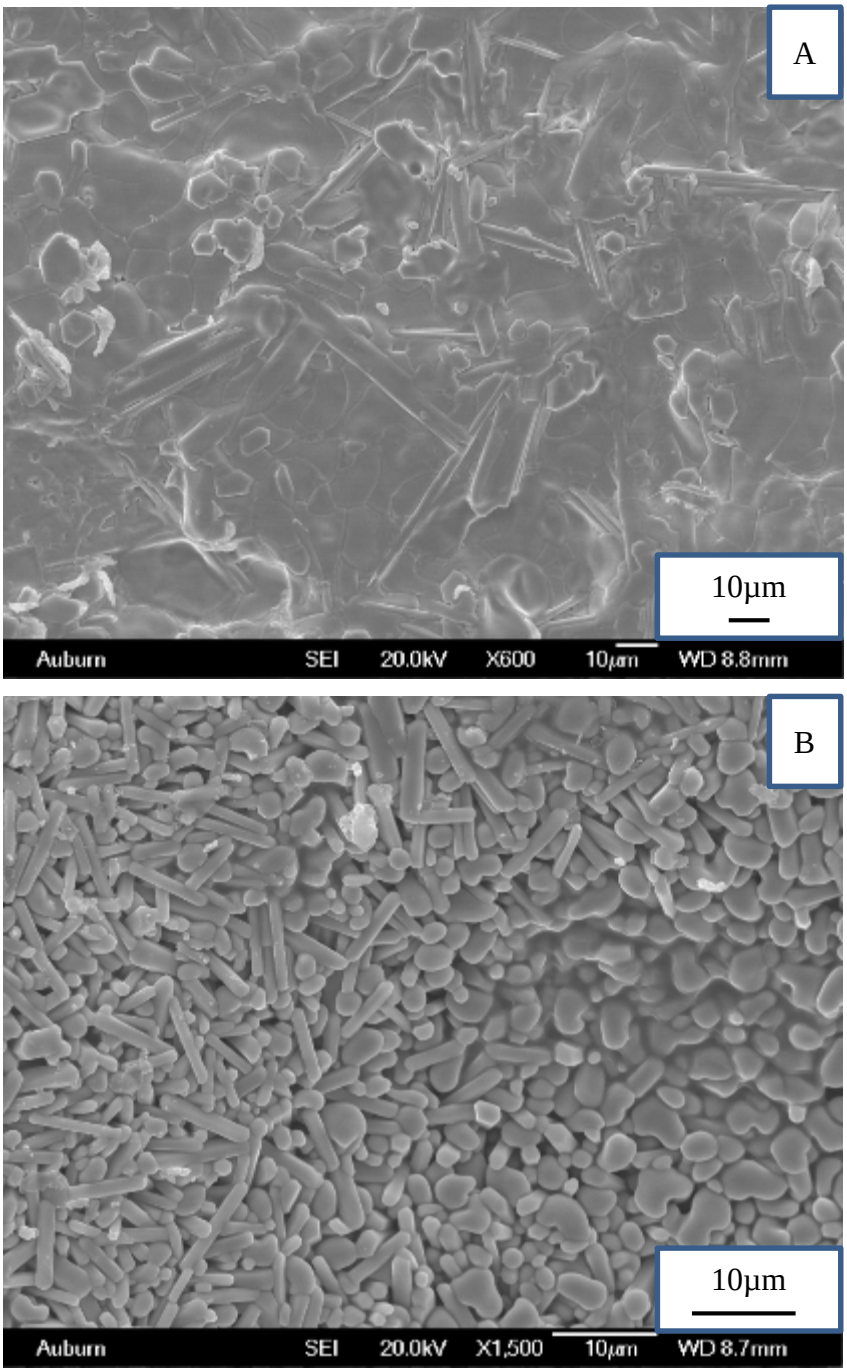

Figure 4.1 Surface morphology of $Gd_2Zr_2O_7$ exposed at CMAS for 5 hours. (A) is taken at 1500°C and (B) is taken at 1300°C.

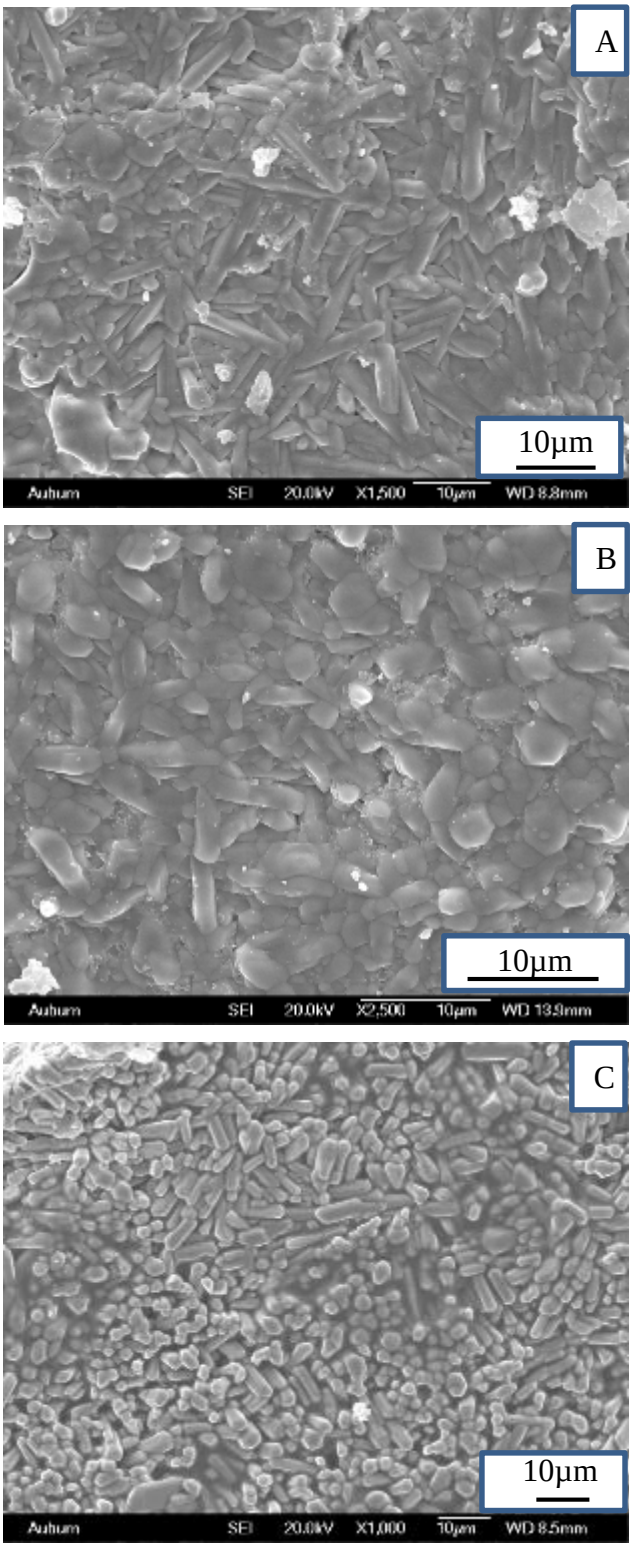

Figure 4.2 $Sm_2Zr_2O_7$ exposed at CMAS for 5 hours. (A), (B) and (C) are taken at 1500°C, 1400°C and 1300°C separately.

To identify the phases after corrosion, the EDS data of $Gd_2Zr_2O_7$ after corrosion tests at various conditions are also shown in Figure 4.3 and Figure 4.4. In Figure 4.3, spectra 1,4,5,7 represent the rod-like phase and the spectra 2, 3 and 6 represent the round phases. In long stick grains, no zirconium was detected and the amount of Si, Ca and Gd closed to a ratio of 3:1:4. While in the round shape grains, the amount of Ca, Si, Mg and Al was almost zero and the content of zirconium was higher than the content of gadolinium, but the difference was not large. This meant the gadolinium element was dissolved in CMAS and precipitated again to form a new phase rich in Si, Ca and Gd. The other phases would remain most zirconium and gadolinium and the phase would reprecipitate to cubic fluorite according to the Gd_2O_3-ZrO_2 phase diagram shown in Figure 1.7. The XRD pattern of the specimens after corrosion at various conditions are shown in Figure 4.5. In the XRD pattern, $Ca_2Gd_8(SiO_4)_6O_2$ is detected and the elemental ratio in elongated grains match the silicate well. The phase transformation from pyrochlore structure to fluorite structure was also corresponded in the XRD pattern. The main peaks shifted to a little bit higher angles due to a decrease in lattice parameter associated with an increase in the amount of zirconium, which was smaller than gadolinium in ionic radii as shown in Table 4.1. All the peaks were labeled. In the spectra of non-corrosion surface and before corrosion, the main peaks represented pyrochlore structure with the (331) and (511) which are present for the pyrochlore structure but not the fluorite structure. Some silicate peaks appeared in non-corrosion surface and it was because the CMAS melted at 1300°C and then flow to this surface along the specimen's edge and then some silicates formed at the non-corrosion surface. In the corrosion surface, the right shifted peaks were labeled as fluorite phase and other peaks were $Ca_2Gd_8(SiO_4)_6O_2$, which could match the EDS data.

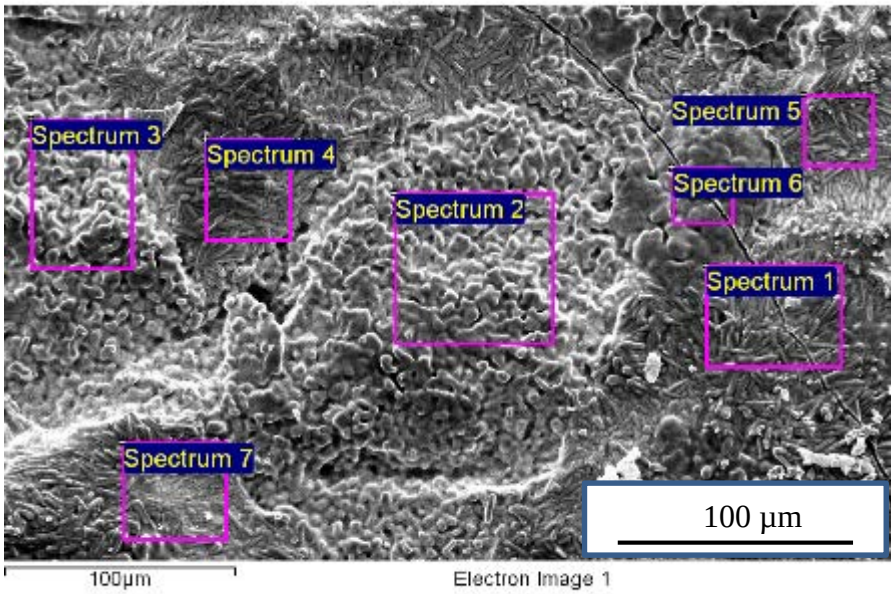

Spectrum	Si	Ca	Zr	Gd
1	13	6	0	25
2	0	2	20	15
3	0	0	19	16
4	13	5	0	17
5	12	4	0	15
6	0	0	22	21
7	12	4	0	18

Figure 4.3 Elemental distribution of $Gd_2Zr_2O_7$ after CMAS corrosion at 1500°C for 5 hours (in atomic ratio).

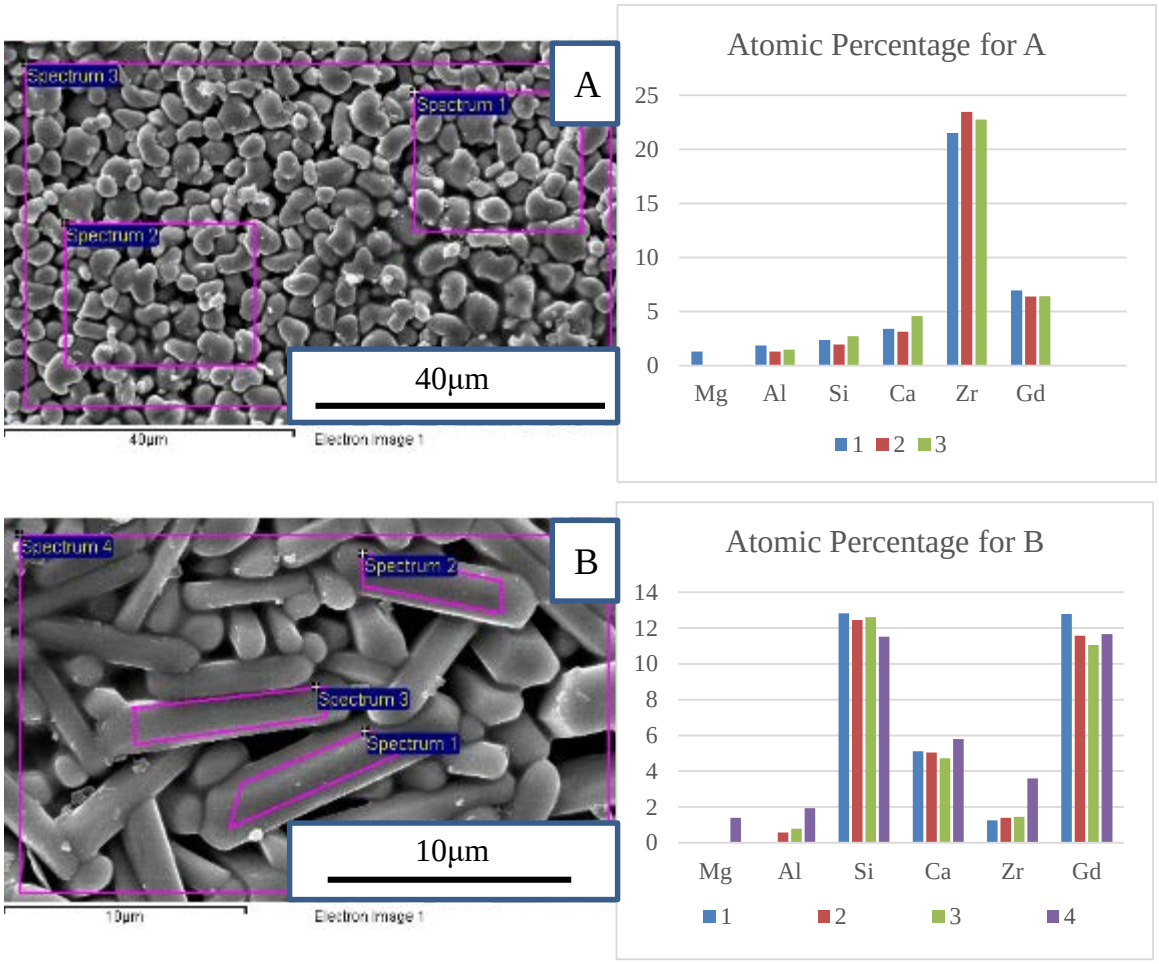

Figure 4.4 Elemental distribution of $Gd_2Zr_2O_7$ pyrochlore ceramics prepared by co-precipitation after CMAS corrosion at 1300°C for 5 hours.

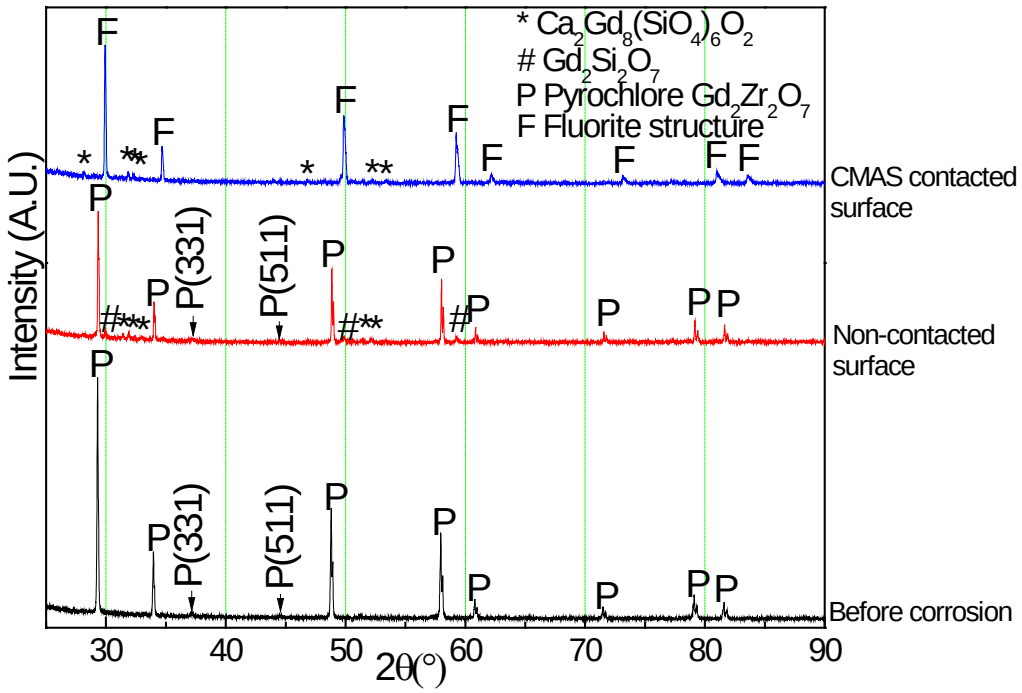

Figure 4.5 XRD pattern of $Gd_2Zr_2O_7$ prepared by co-precipitation before and after corrosion test at 1300°C for 5 hours. JCPDS 01-075-8269 (pyrochlore), 01-080-0471 (fluorite) and 00-028-0212 ($Ca_2Gd_8(SiO_4)_6O_2$) are used.

Table 4.1 Ionic radii with coordination number = VIII [88].

Ion	Radium (pm)
Zr^{4+}	84
Gd^{3+}	105.3
Sm^{3+}	107.9

The phase information and elemental distribution of $Sm_2Zr_2O_7$ after corrosion test are shown in Figure 4.6 and Figure 4.7. The result was similar to the $Gd_2Zr_2O_7$ after corrosion. The new elongated phase was rich in Si, Ca and Sm and almost no Zr was

detected. Additionally, the ratio of Si:Ca:Sm was close to the ratio shown in Figure 4.3. While in the round shape grains, almost no Ca, Mg, Si and Al was detected and the amount of Zr was larger than that of Sm, especially in the whole area shown in spectrum 5. This illustrated that Sm was dissolved in the molten CMAS and form a new silicate phase. According to the Sm_2O_3-ZrO_2 phase diagram shown in Figure 1.8, the rest would be dissolved in CMAS and reprecipitate to cubic fluorite with the increase in ratio of Zr:Sm. The XRD pattern of $Sm_2Zr_2O_7$ after corrosion at 1300°C is shown in Figure 4.8. $Sm_2Zr_2O_7$ presented the similar result as $Gd_2Zr_2O_7$ after corrosion test. In the non-corrosion surface, most peaks were the pyrochlore structure peaks with (311), (331) and (511) index which can tell the difference between pyrochlore structure and cubic fluorite structure. In the corrosion surface, all the main peaks shifted to the higher angle and could match the fluorite structure well. Higher peak angles illustrated a lower lattice parameter. This can be explained by the increase in the amount of Zr and the smaller size of Zr^{4+} ion decreased the lattice parameter. The ionic radius of related ions are also shown in Table 4.1. The small peaks in the spectra of corrosion surface are labeled as $Ca_2Sm_8(SiO_4)_6O_2$. Combined with the elemental distribution data, the fluorite phase and calcium samarium silicate phase illustrate that CMAS glass melted on the surface, and then Sm was dissolved from pyrochlore structure and reacted with CMAS to form $Ca_2Sm_8(SiO_4)_6O_2$ crystal.

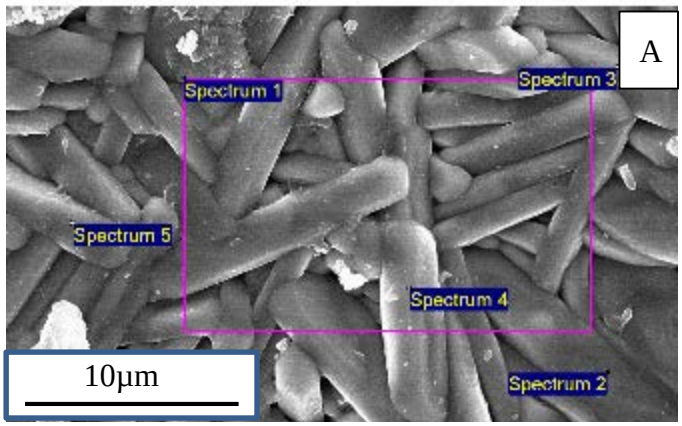

Spectrum	Si	Ca	Sm
1	14	4	17
2	15	6	20
3	15	6	19
4	14	5	17
5	14	5	17

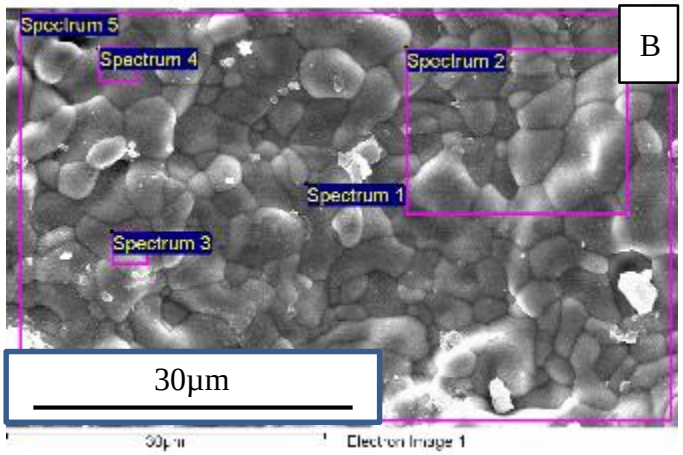

Spectrum	Ca	Zr	Sm
1	1	20	13
2	2	23	17
3	2	23	24
4	0	24	21
5	0	21	15

Figure 4.6 Elemental distribution of different phases in $Sm_2Zr_2O_7$ after corrosion at 1500°C for 5 hours. (A) is the long shape grains and (B) is the round shape grains. The value is in atomic ratio.

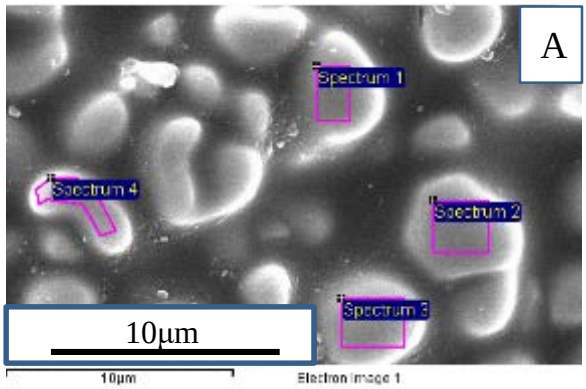

Spectrum	Al	Si	Ca	Zr	Sm
1	1	1	2	26	4
2	1	2	3	31	5
3	1	1	3	28	5
4	1	2	4	33	6

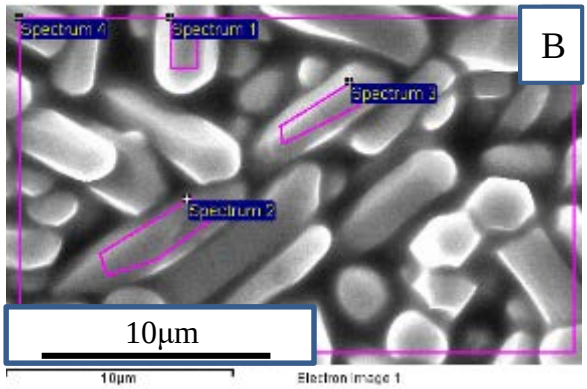

Spectrum	Al	Si	Ca	Zr	Sm
1	1	15	6	1	15
2	1	13	5	1	11
3	0	14	5	1	14
4	3	12	6	4	12

Figure 4.7 Elemental distribution of different phases in $Sm_2Zr_2O_7$ after corrosion at 1300°C for 5 hours. A is the round shape grans and B is the long shape grains. All the values are in atomic ratio.

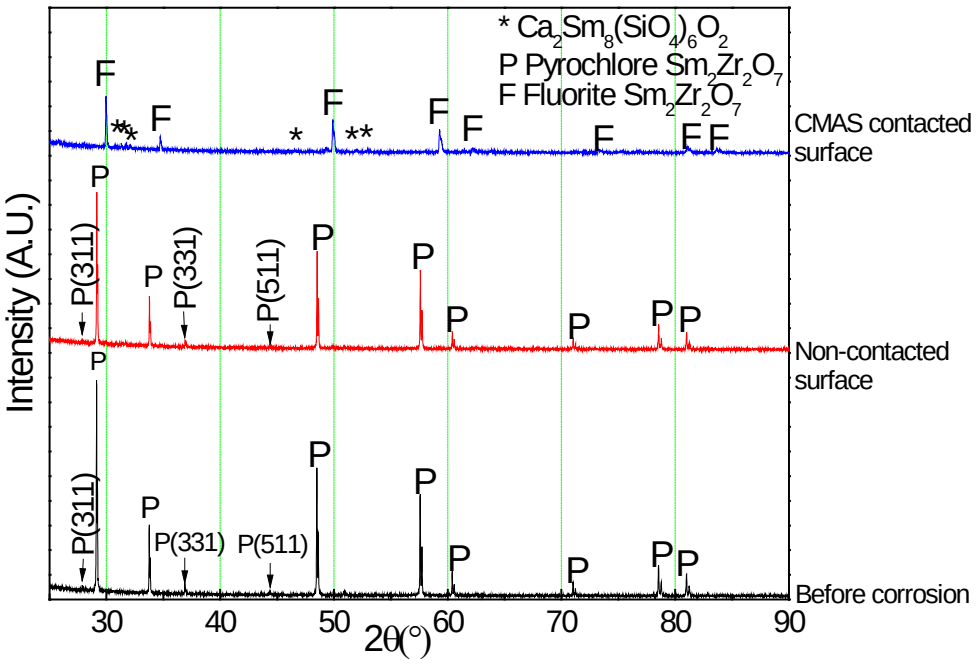

Figure 4.8 XRD pattern of $Sm_2Zr_2O_7$ prepared by co-precipitation method after corrosion test at 1300°C for 5 hours. $Ca_2Sm_8(SiO_4)_6O_2$ are detected.

4.1.2. Trends in reaction product as temperature varies

4.1.2.1. $Gd_2Zr_2O_7$

The combined XRD pattern of $Gd_2Zr_2O_7$ after corrosion at 1300°C, 1400°C and 1500°C are shown in Figure 4.9. Compared to the non-corrosion spectra, all the peaks shifted to right due to formation of cubic fluorite structure and decrease in cation size. Furthermore, corrosion at lower temperature (1300°C) tends to shift more than corrosion at higher temperature (1500°C). The d-spacing data calculated from Bragg's law ($n\lambda=2dsin\theta$) and lattice parameter can be calculated from d-spacing. The lattice parameter of $Gd_2Zr_2O_7$ from non-corrosion to corrosion at various temperatures are shown in Table 4.2 (angles' value and d-spacing can be found in Appendix I). The decreasing in lattice parameter at lower corrosion temperature (1300°C) means the cubic fluorite structure

product after corrosion was smaller than the reaction product at higher corrosion temperature (1500°C). Zr^{4+} has a smaller radii than Gd^{3+} (see Table 4.1), so the decrease in d-spacing was caused by addition Zr in cubic fluorite product. Thus, the smaller crystals in lower corrosion temperature (1300°C) should have more Zr than the crystals in higher corrosion temperature (1500°C). In Gd_2O_3-ZrO_2 phase diagram shown in Figure 1.7, the cubic fluorite phase tended to have more Zr at lower temperature, which was consistent with the result from XRD pattern.

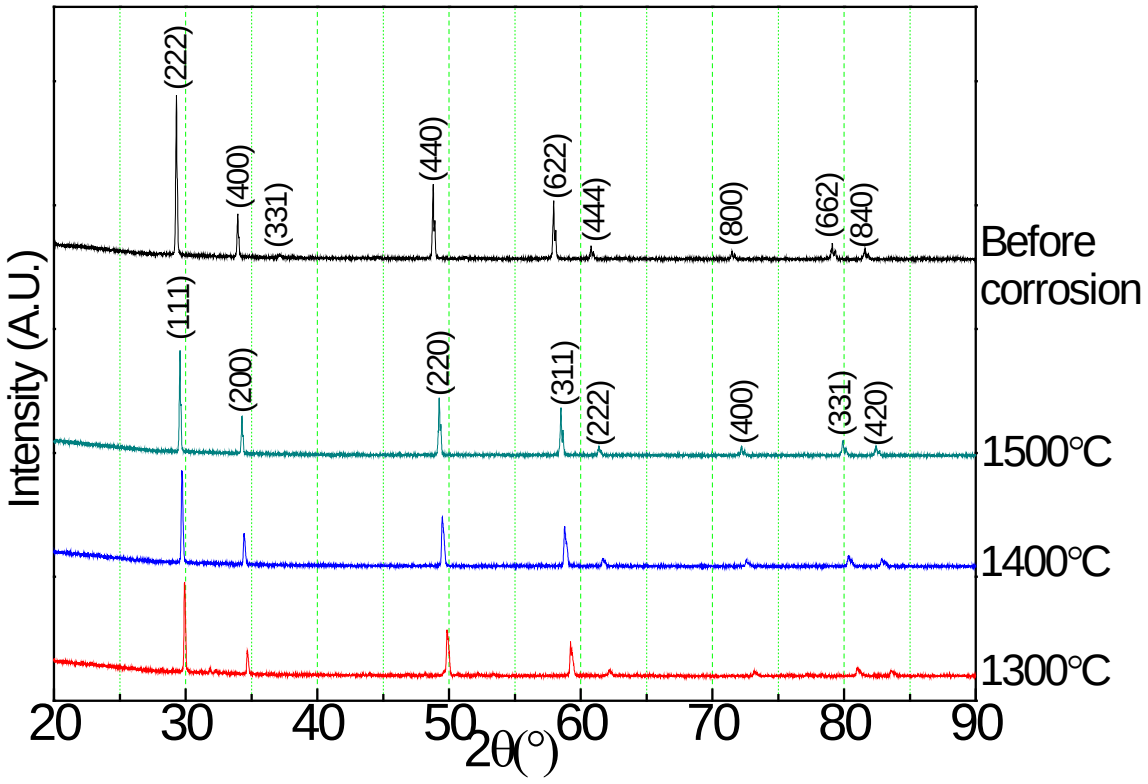

Figure 4.9 Combined XRD pattern of $Gd_2Zr_2O_7$ after corrosion at 1300°C, 1400°C and 1500°C.

Table 4.2 Lattice parameter of $Gd_2Zr_2O_7$ from non-corrosion to corroded at various temperatures.

	Non-corrosion	1500°C	1400°C	1300°C
Lattice parameter (Å)	5.272	5.227	5.201	5.167

The elemental information of the cubic fluorite phase after corrosion at various temperatures are summarized in Table 4.3. The elemental distribution results are consistent with the phase diagram in Figure 1.7. Lower corrosion temperature presented higher Zr/Gd ratio, which means more Zr existed in the reaction products.

Table 4.3 Atomic percentage of Zr and Gd in cubic fluorite phase after corrosion at various temperature (data from EDS).

Spectrum	1500°C		1400°C		1300°C	
	Zr	Gd	Zr	Gd	Zr	Gd
1	22	15	25	12	22	6
2	26	21	25	12	24	7
3	22	16	27	13	21	6
4	17	10	24	10	22	6
5	20	15	24	12	21	6
Average	21.4	15.4	25	11.8	22	6.2

4.1.2.2. $Sm_2Zr_2O_7$

The combined XRD pattern of $Sm_2Zr_2O_7$ after corrosion at 1300°C, 1400°C, 1500°C and non-corrosion $Sm_2Zr_2O_7$ are shown in Figure 4.10. $Sm_2Zr_2O_7$ presented

similar result as $Gd_2Zr_2O_7$. After corrosion, all peaks shifted to right due to the formation of cubic fluorite phase and lower corrosion temperature (1300°C) shifted more than higher corrosion temperature (1500°C). The lattice parameter data calculated from XRD pattern are shown in Table 4.4. The decreasing lattice parameter meant more Zr existed in the cubic fluorite phase because Zr^{4+} had a smaller radii than Sm^{3+} (see Table 4.1). Furthermore, smaller d-spacing in lower corrosion temperature (1300°C) meant the cubic fluorite phase had more Zr than the phase formed at higher corrosion temperature (1500°C), which was consistent with the Sm_2O_3-ZrO_2 phase diagram (see Figure 1.8).

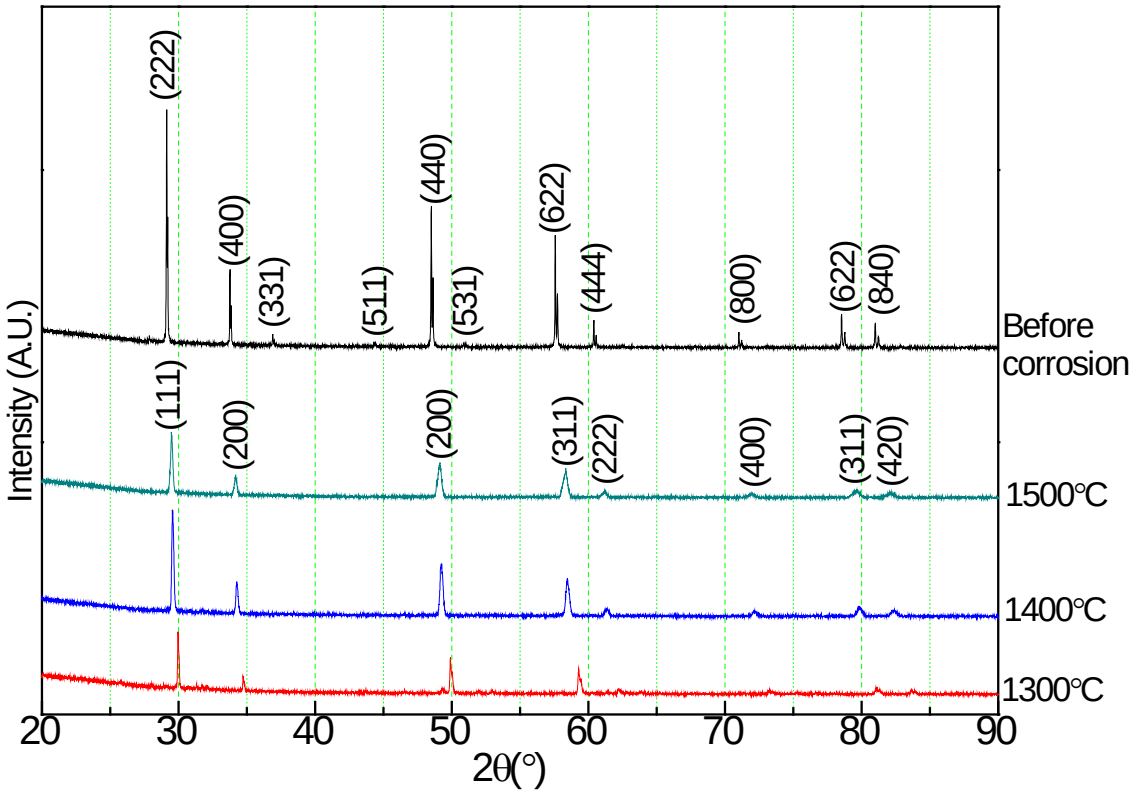

Figure 4.10 XRD pattern of $Sm_2Zr_2O_7$ after corrosion at various temperature.

Table 4.4 Lattice parameter of $Sm_2Zr_2O_7$ from non-corrosion to corroded at various temperatures.

	Non-corrosion	1500°C	1400°C	1300°C
Lattice parameter (Å)	5.304	5.242	5.230	5.159

The elemental information of cubic fluorite phase after corrosion at various temperatures are summarized in Table 4.5. The elemental distribution results are consistent with the phase diagram in Figure 1.8.

Table 4.5 Atomic percentage of Zr and Sm in cubic fluorite phase after corrosion at various temperatures (data from EDS).

Spectrum	1500°C		1400°C		1300°C	
	Zr	Sm	Zr	Sm	Zr	Sm
1	20	13	24	13	26	4
2	23	17	22	12	31	5
3	23	24	22	12	28	5
4	24	21	22	13	33	6
5	21	15	22	12		
6			23	12		
Average	22.2	18	22.5	12.33	29.5	5

4.2. Low temperature (<1250°C) CMAS corrosion property

4.2.1. Reaction product

Surface morphology and elemental distribution of $Gd_2Zr_2O_7$ after CMAS corrosion at 1200°C are shown in Figure 4.11 and Figure 4.14. In Figure 4.11, the spectra 1, 2 and 3 were the long shape grains with small amount of Zr and certain amount of Si, Ca and Gd close to $Ca_2Gd_8(SiO_4)_6O_2$. The round grains in spectra 9, 10 and 11 contained much more Zr than other spectra and the Zr rich cubic fluorite phase forms after corrosion. The cubic fluorite zirconia phase and silicate phase corresponded to the phases in corrosion test at higher temperature (>1250°C) and showed the basic reaction between pyrochlore materials and CMAS keeps the same either above or below the melting point of CMAS. While in Figure 4.14, the longer corrosion time forms the same phases and reaction product. Spectra 2, 3 and 4 represented round shape grains that contained more Zr and meant the cubic fluorite structure. Spectra 5, 6 and 7 represented long shape grains contained close ratio of Ca, Gd and Si as $Ca_2Gd_8(SiO_4)_6O_2$. Extra Zr detected in spectra 5, 6 and 7 might come from nearby fluorite grains because the X-ray used in EDS had a diameter around 1 μm.

However, it is also clear to see that some new phases besides cubic fluorite structure and $Ca_2Gd_8(SiO_4)_6O_2$ formed after corrosion at 1200°C. In Figure 4.11, there is a much longer grain than normal $Ca_2Gd_8(SiO_4)_6O_2$ phase with almost zero Zr and Gd inside. The data from spectra 4 to spectra 8 shows this kind of grains. The average ratio of Al:Si:Ca was close to 2:2:1 and the rod-like phase can be defined as $CaAl_2Si_2O_8$. Some recent research also found that enriching Al in CMAS composition contributes to forming anorthite platelets crystal [75]. While in Figure 4.14, another phase that has a much larger size than normal cubic fluorite and gadolinium silicate presented after corrosion at 1200°C.

This crystal also appears at same corrosion at 1200°C for 20 hours and 40 hours, and the EDS data are shown from Figure 4.12 to Figure 4.14. The spectra 1 to spectra 10 in Figure 4.12, spectra 1 in Figure 4.13 and spectra 1 in Figure 4.14 represented this crystal. It illustrated that the shape of this new phase could be either long stick shape or square shape and its size could be hundreds of microns, which was much larger than the normal reaction product, cubic fluorite zirconia and gadolinium silicate, and even much larger than anorthite $CaAl_2Si_2O_8$. The amount of Mg, Al, Si and Ca kept similar and the average ratio was close to 1:1:3:3 and it can be defined as $Mg_2Al_2Si_6Ca_6O_{23}$. Since almost none Zr and Gd are detected in this two phases, they are mainly from the molten CMAS and re-crystallization.

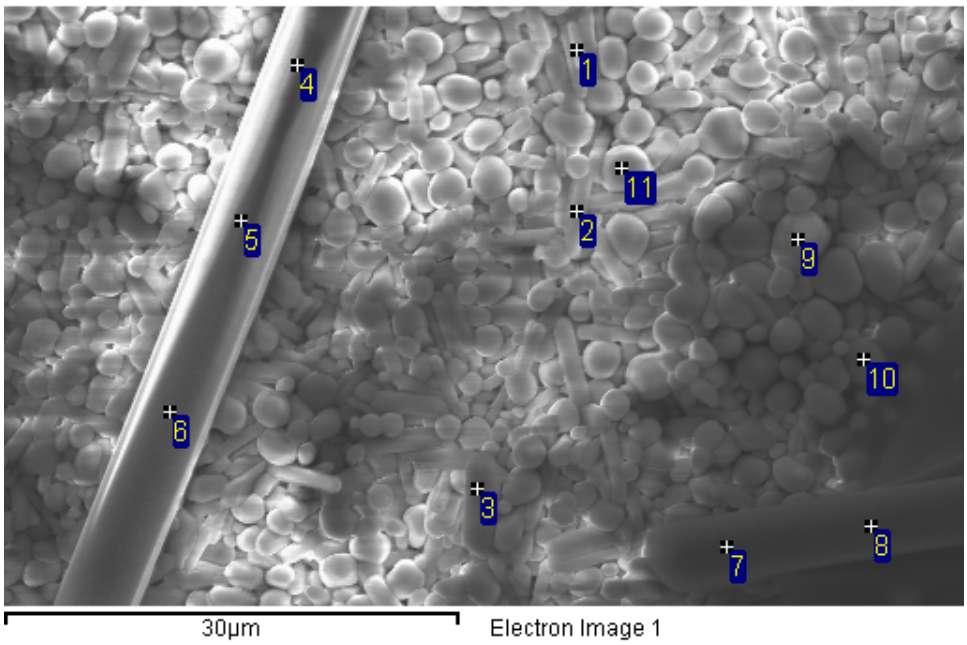

Spectrum	Al	Si	Ca	Zr	Gd
1	4	12	5	4	10
2	1	11	5	3	9
3	1	13	5	3	13
4	15	15	9	0	0
5	13	14	7	0	0
6	13	14	6	0	0
7	14	15	7	0	0
8	14	15	7	0	0
9	0	1	2	28	4
10	1	2	3	28	4
11	1	1	2	23	3

Figure 4.11 Surface morphology and elemental distribution of $Gd_2Zr_2O_7$ after CMAS exposure at 1200°C for 10 hours – 1. All values are in atomic ratio.

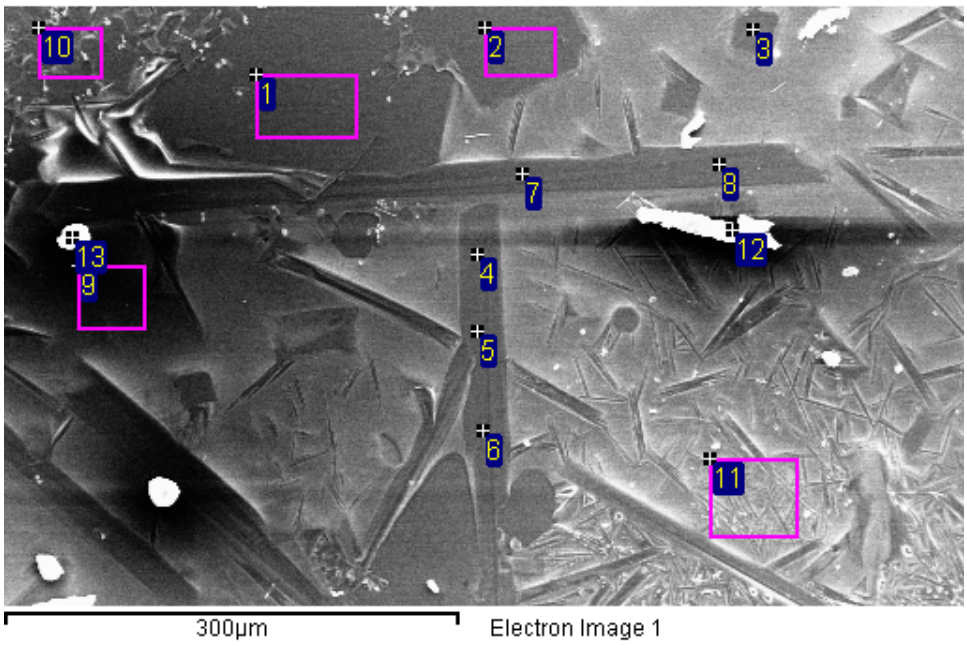

Spectrum	Mg	Al	Si	Ca	Zr	Gd
1	5	5	15	14	0	0
2	5	5	14	14	0	0
3	5	4	15	14	0	0
4	5	5	14	14	0	0
5	5	5	15	14	0	0
6	6	4	15	14	0	0
7	5	5	14	13	0	0
8	5	5	14	14	0	0
9	3	7	15	9	1	1
10	5	5	13	12	1	0
11	5	8	16	7	1	1
12	1	1	1	4	5	0
13	2	5	14	18	2	2

Figure 4.12 Surface morphology and elemental distribution of $Gd_2Zr_2O_7$ after CMAS exposure at 1200°C for 10 hours – 2. All values are in atomic ratio.

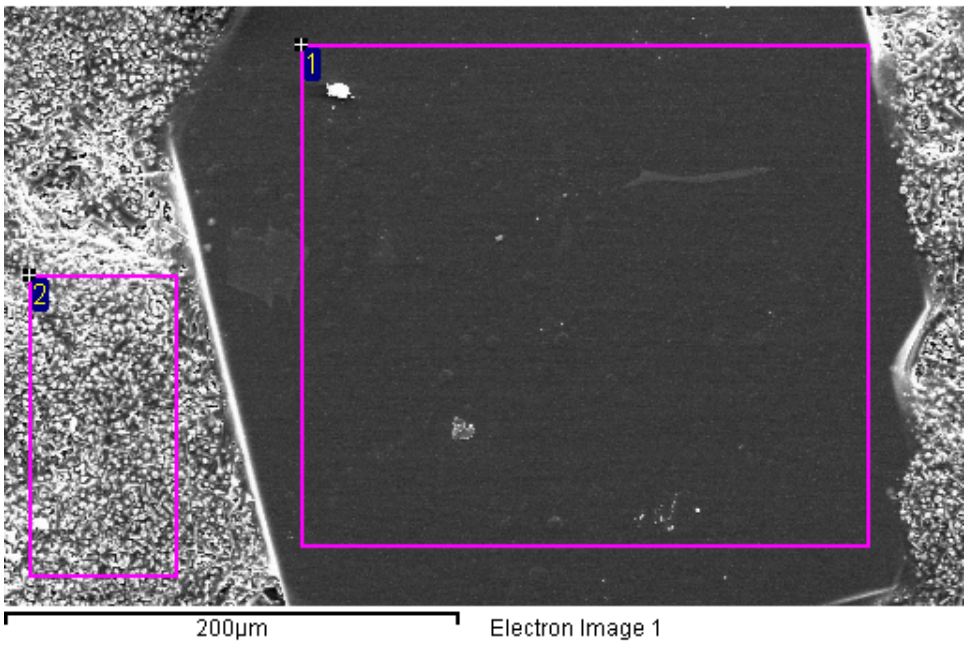

Spectrum	Mg	Al	Si	Ca	Zr	Sm
1	6	5	18	19	0	0
2	4	6	13	7	6	5

Figure 4.13 Surface morphology and elemental distribution of $Gd_2Zr_2O_7$ after CMAS corrosion at 1200°C for 20 hours. All values are in atomic ratio.

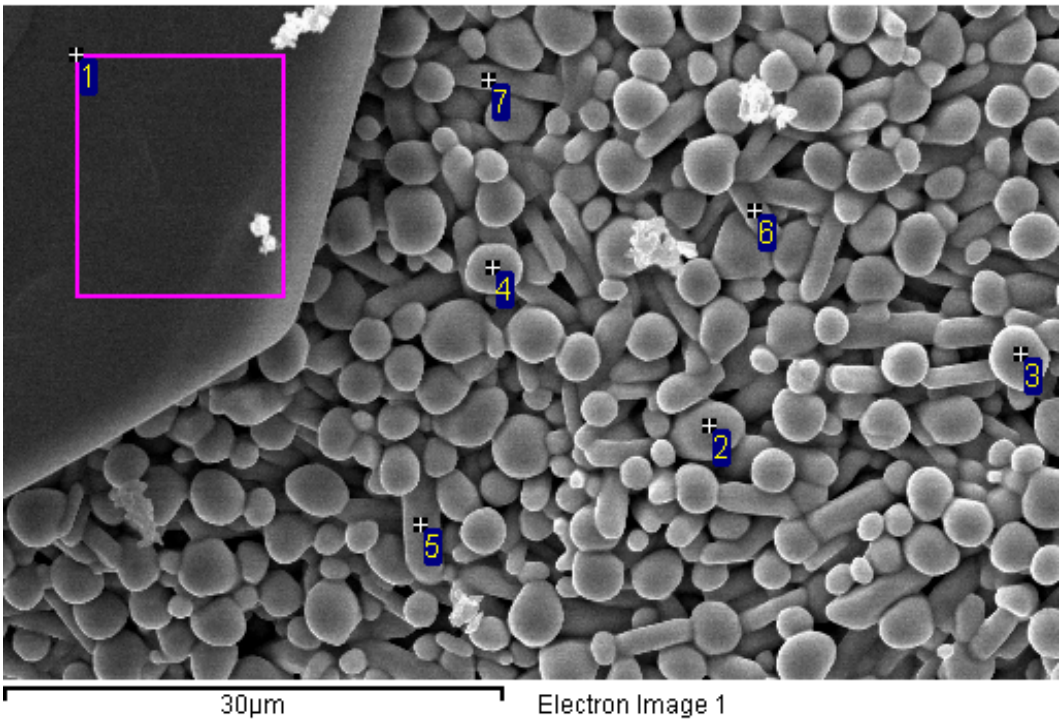

Spectrum	Mg	Al	Si	Ca	Zr	Gd
1	6	5	18	15	1	0
2	0	0	1	3	43	7
3	0	0	2	2	34	5
4	0	0	2	3	33	5
5	0	0	13	7	13	14
6	0	0	7	5	23	17
7	0	0	8	3	15	8

Figure 4.14 Surface morphology and elemental distribution of $Gd_2Zr_2O_7$ after CMAS exposure at 1200°C for 40 hours. All values are in atomic ratio.

To understand the phases after lower temperature corrosion, the XRD pattern of $Gd_2Zr_2O_7$ after CMAS corrosion at 1200°C for 10 hours are shown in Figure 4.15. Phases detected in the XRD spectrum include calcium gadolinium silicate, anorthite calcium

aluminum silicate, cubic fluorite zirconia, gadolinium silicate and the single crystal $Mg_2Al_2Si_6Ca_6O_{23}$. Most peaks can be labeled and indexed by standard JCPDS card 00-028-0212 ($Ca_2Gd_8(SiO_4)_6O_2$), 00-041-1486 ($CaAl_2Si_2O_8$), 01-080-0471 (fluorite $Zr_2Gd_2O_7$) and 01-070-7964 ($Gd_2(Si_2O_7)$).

However, there is no standard JCPDS card that can match $Mg_2Al_2Si_6Ca_6O_{23}$ well because the composition of silicates can vary and no matched card is found in the updated database. Higher intensity of $Mg_2Al_2Si_6Ca_6O_{23}$ crystal shows larger grains and this corresponded to the SEM and EDS images mentioned before. Five main peaks of $Mg_2Al_2Si_6Ca_6O_{23}$ located at 17.67°, 35.75°, 39.04°, 54.82° and 75.72°. The d-spacing data of each peak were calculated and shown in Table 4.6. The peaks located at 17.67°, 35.75° and 75.72° had integer multiple d-spacing value, which meant this three peaks represented parallel lattice planes.

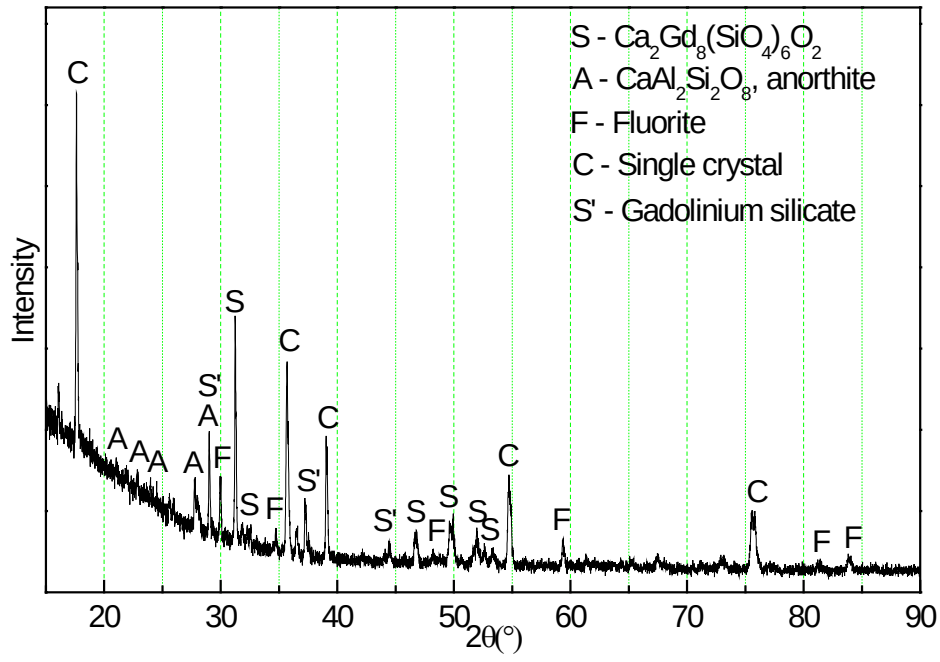

Figure 4.15 XRD spectrum of $Gd_2Zr_2O_7$ after CMAS exposure at 1200°C for 10 hours.

Table 4.6 d-spacing of $Mg_2Al_2Si_6Ca_6O_{23}$ crystal (calculated by Bragg's law).

	θ_1	θ_2	θ_3	θ_4	θ_5
2θ(°)	17.67	35.75	39.04	54.82	75.72
θ(°)	8.84	17.88	19.52	27.41	37.86
θ(π)	0.15	0.31	0.34	0.48	0.66
sinθ	0.15	0.31	0.33	0.46	0.61
λ(Å)	1.54				
d(n=1)	5.02	2.51	2.31	1.67	1.26
d(n=2)	10.04	5.02	4.61	3.35	2.51

The $Mg_2Al_2Si_6Ca_6O_{23}$ single crystal appeared not only at $Gd_2Zr_2O_7$, but also at Gd-Sm-Zr-O compositions. Figure 4.16 shows surface morphology and elemental distribution information of $(Gd_{0.6}Sm_{0.4})_2Zr_2O_7$ after CMAS exposure at 1200°C for 40 hours. The crystal appeared in this image in spectrum 1 had a size in hundreds of microns and the composition was also approximately as same as $Gd_2Zr_2O_7$ after CMAS corrosion. The XRD pattern of $(Gd_{0.6}Sm_{0.4})_2Zr_2O_7$ and $(Gd_{0.8}Sm_{0.2})_2Zr_2O_7$ after CMAS corrosion at 1200°C for 40 hours are shown in Figure 4.17 and Figure 4.18 individually. It is clear to see that after corrosion at 1200°C, five peaks that cannot match the standard JCPDS card locate at the same angle as $Mg_2Al_2Si_6Ca_6O_{23}$ crystal in Figure 4.15. Since the original CMAS glass was in amorphous phase, all the new phases formed after corrosion. So the lanthanide zirconia can act as nucleation and accelerate the formation of $Mg_2Al_2Si_6Ca_6O_{23}$ crystal.

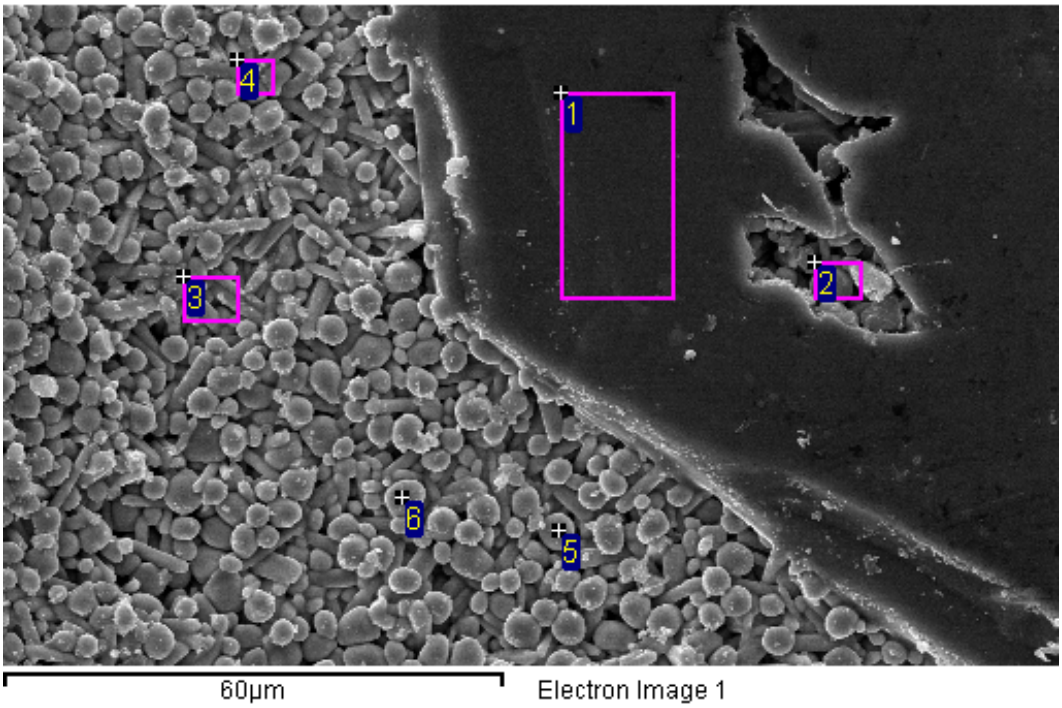

Spectrum	Mg	Al	Si	Ca	Zr	Sm	Gd
1	5	6	18	20	1	0	0
2	0	1	5	6	26	3	6
3	0	0	10	5	10	4	7
4	0	0	10	5	13	5	7
5	0	0	1	2	29	1	3
6	0	0	0	2	33	1	3

Figure 4.16 Surface morphology and elemental distribution of $(Gd_{0.6}Sm_{0.4})_2Zr_2O_7$ after CMAS exposure at 1200°C for 40 hours.

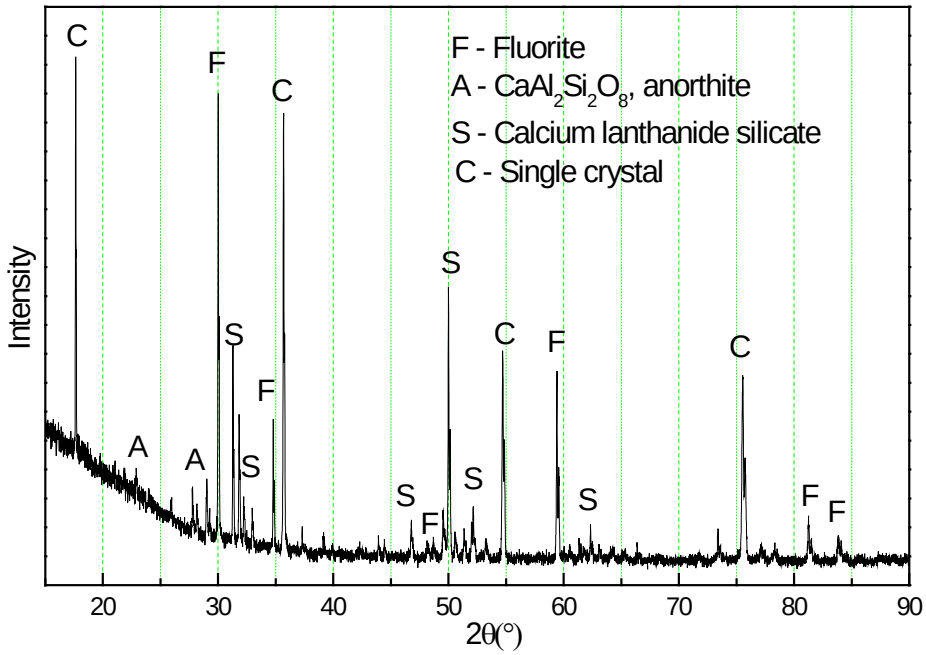

Figure 4.17 XRD pattern of $(Gd_{0.6}Sm_{0.4})_2Zr_2O_7$ after CMAS exposure at 1200°C for 40 hours.

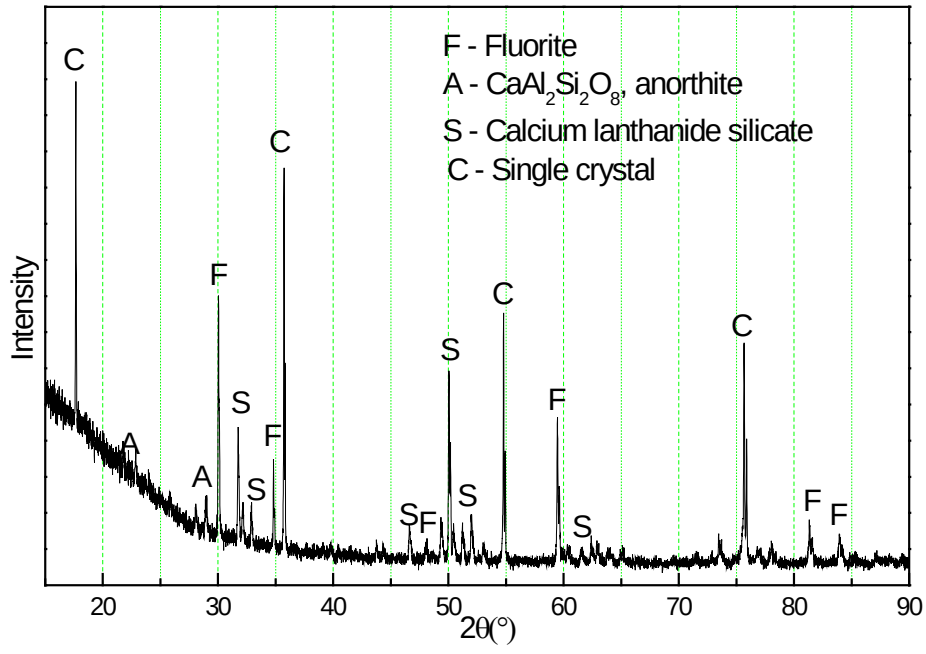

Figure 4.18 XRD pattern of $(Gd_{0.8}Sm_{0.2})_2Zr_2O_7$ after CMAS exposure at 1200°C for 40 hours.

Furthermore, the $Mg_2Al_2Si_6Ca_6O_{23}$ also formed at other low temperature corrosion. The XRD pattern of $Gd_2Zr_2O_7$ in low porosity (19%) with CMAS – 1 exposure at 1215°C for 10 hours are shown in Figure 4.19. Single crystal peaks at 17.67°, 35.75°, 39.04°, 54.82° and 75.72° appeared.

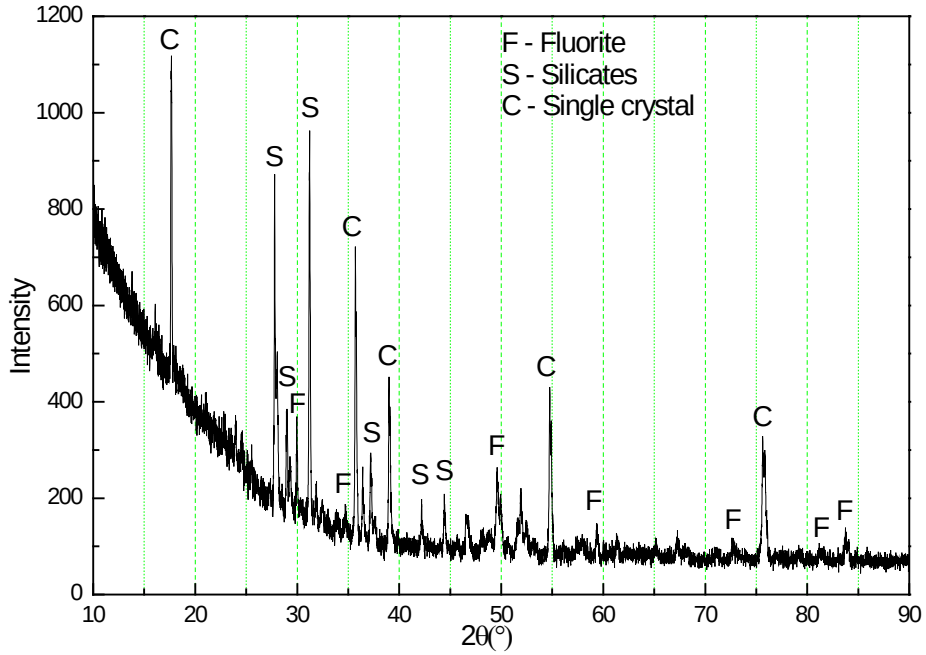

Figure 4.19 XRD pattern of $Gd_2Zr_2O_7$ in low porosity (19%) with CMAS – 1 exposure for 10 hours at 1215°C.

To understand the formation mechanism of $Mg_2Al_2Si_6Ca_6O_{23}$ single crystal, extra experiments were needed. Corrosion experiment with small amount of CMAS – 1 was taken at 1200°C for 10 hours. The XRD pattern of $Gd_2Zr_2O_7$ in low porosity (19%) with 5 mg/cm^2 CMAS – 1 exposure at 1200°C for 10 hours is shown in Figure 4.20. The surface was mixed by pyrochlore phase, cubic fluorite phase and silicates. The pyrochlore phase was the uncovered surface due to the small amount of CMAS. No $Mg_2Al_2Si_6Ca_6O_{23}$ single

crystal formed according to the XRD pattern. Compared with Figure 4.15, the $Mg_2Al_2Si_6Ca_6O_{23}$ single crystal formed by the extra CMAS during corrosion process.

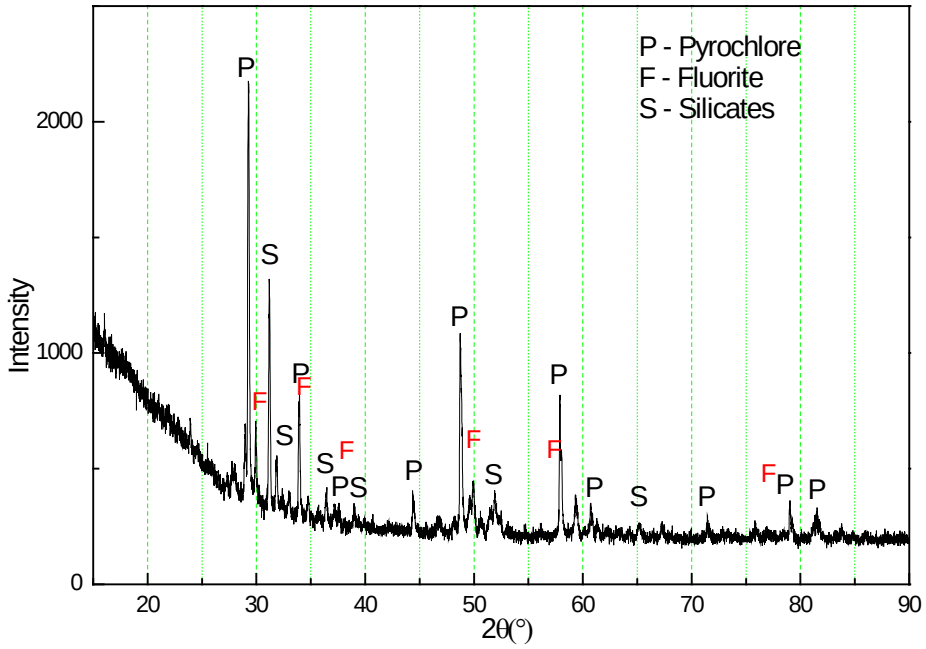

Figure 4.20 XRD pattern of $Gd_2Zr_2O_7$ in low porosity (19%) with small amount of CMAS – 1 (5 mg/cm^2) exposure at 1200°C for 10 hours.

4.2.2. Trends in grain size as corrosion time increased

The grain size of $Gd_2Zr_2O_7$, $(Gd_6Sm_4)_{0.2}Zr_2O_7$ and $(Gd_8Sm_2)_{0.2}Zr_2O_7$ was analyzed. The grain size was analyzed by measurement in SEM images. Cubic fluorite zirconia was in round shape, so it was presented by the diameter. Meanwhile, lanthanide calcium silicate was measured in length due to its stick shape phase. 20 fluorite grains and 20 silicate grains were picked to calculate the grain size in each sample. More images related to grain size calculation are shown from Appendix II to Appendix IV.

$Gd_2Zr_2O_7$ after CMAS – 1 corrosion at 1200°C for 20h, 40h and 60h are shown in Figure 4.21 and the grain size of fluorite and silicate phase are shown in Figure 4.22.

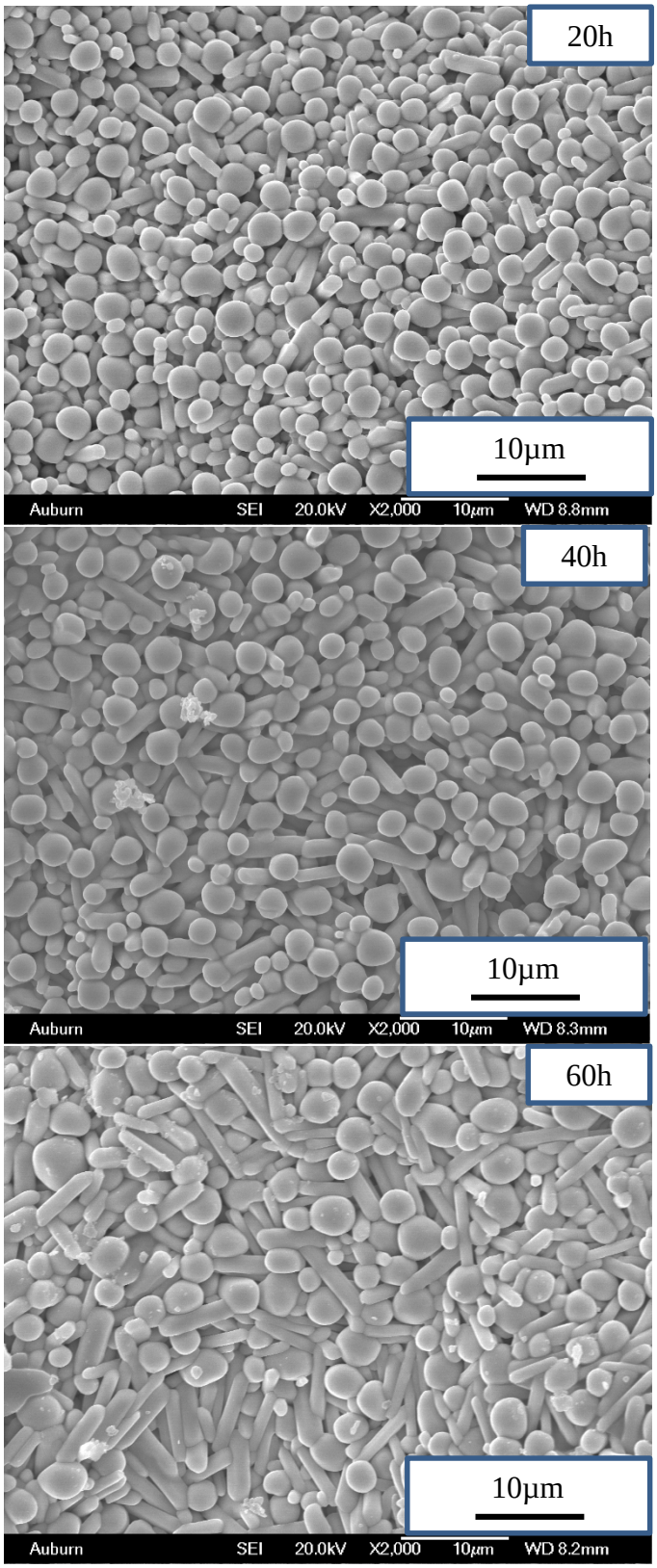

Figure 4.21 $Gd_2Zr_2O_7$ after CMAS corrosion at 1200°C for 20h, 40h and 60h.

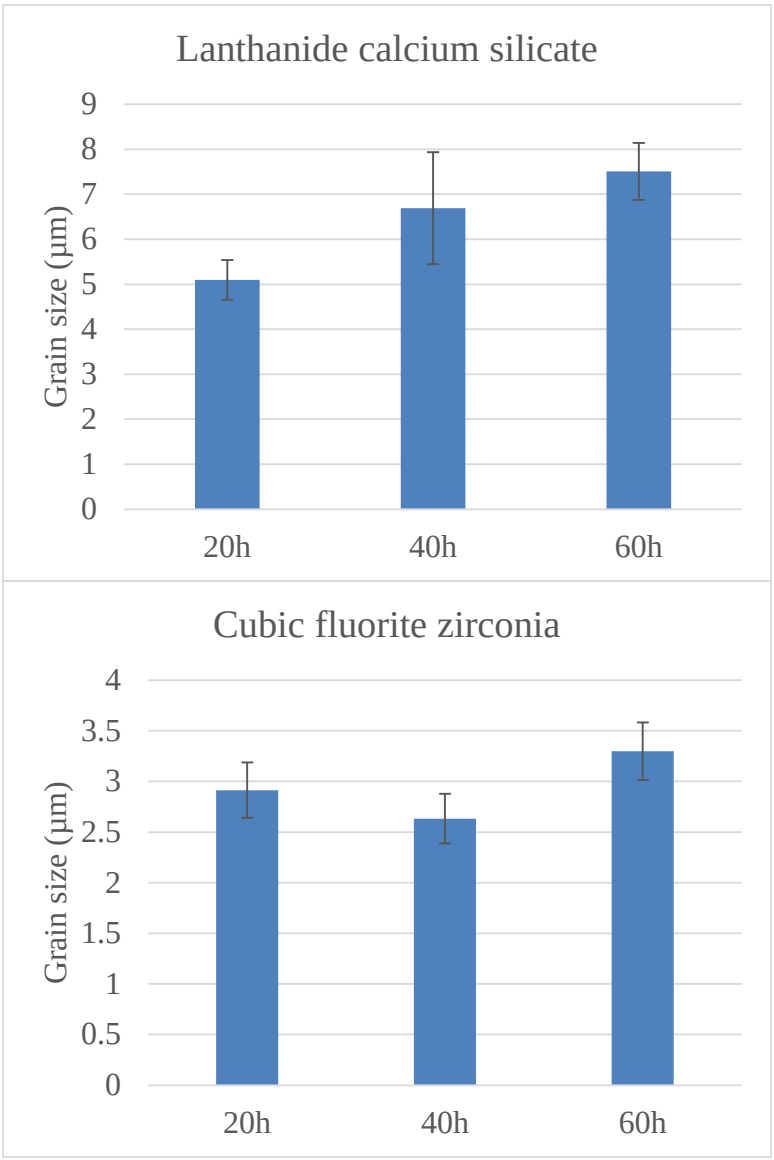

Figure 4.22 Grain size of silicate and fluorite zirconia phases in $Gd_2Zr_2O_7$ after corrosion (data calculated from SEM images). Error bar represents standard deviation. 20 grains were picked for each phase.

$(Gd_6Sm_4)_{0.2}Zr_2O7$ after CMAS – 1 corrosion for 20h, 40h and 60h at 1200°C are shown in Figure 4.23 and the grain size data are shown in Figure 4.24.

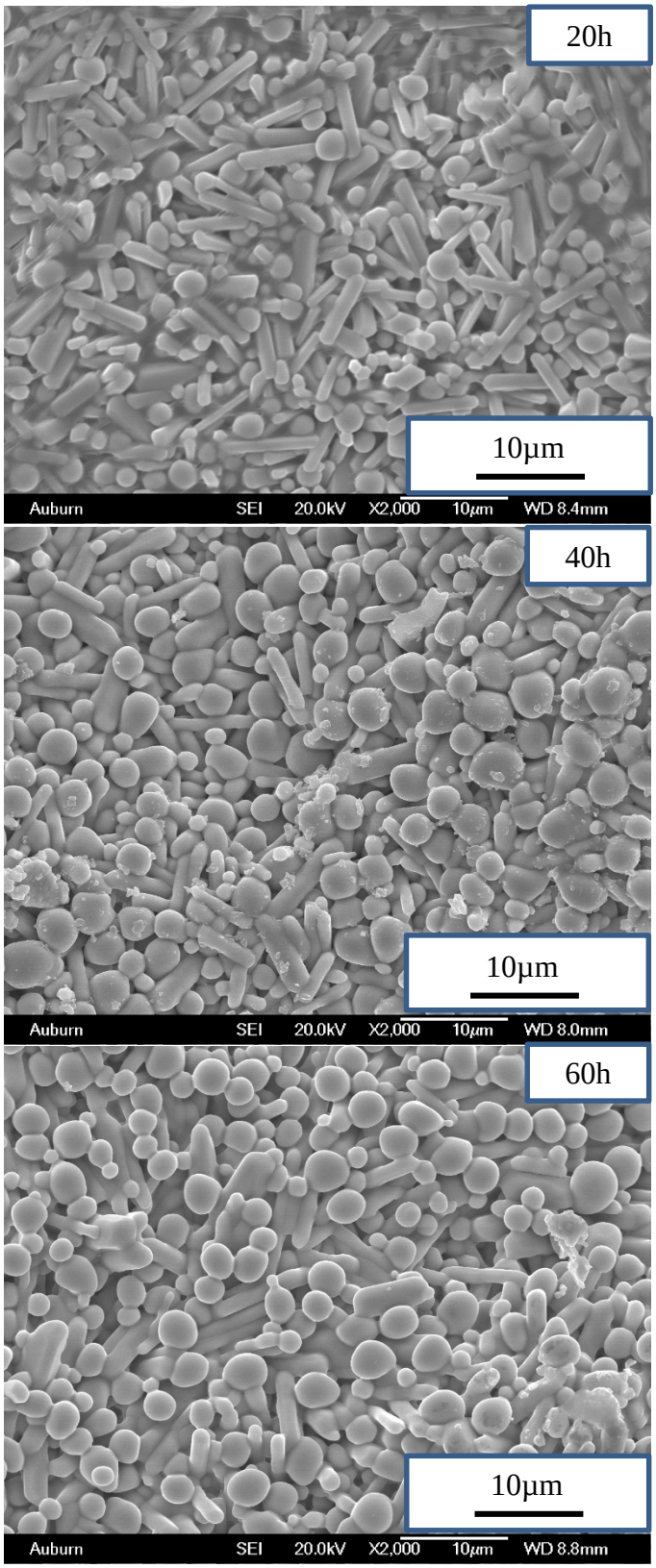

Figure 4.23 $(Gd_6Sm_4)_{0.2}Zr_2O_7$ after CMAS corrosion at 1200°C for 20h, 40h and 60h.

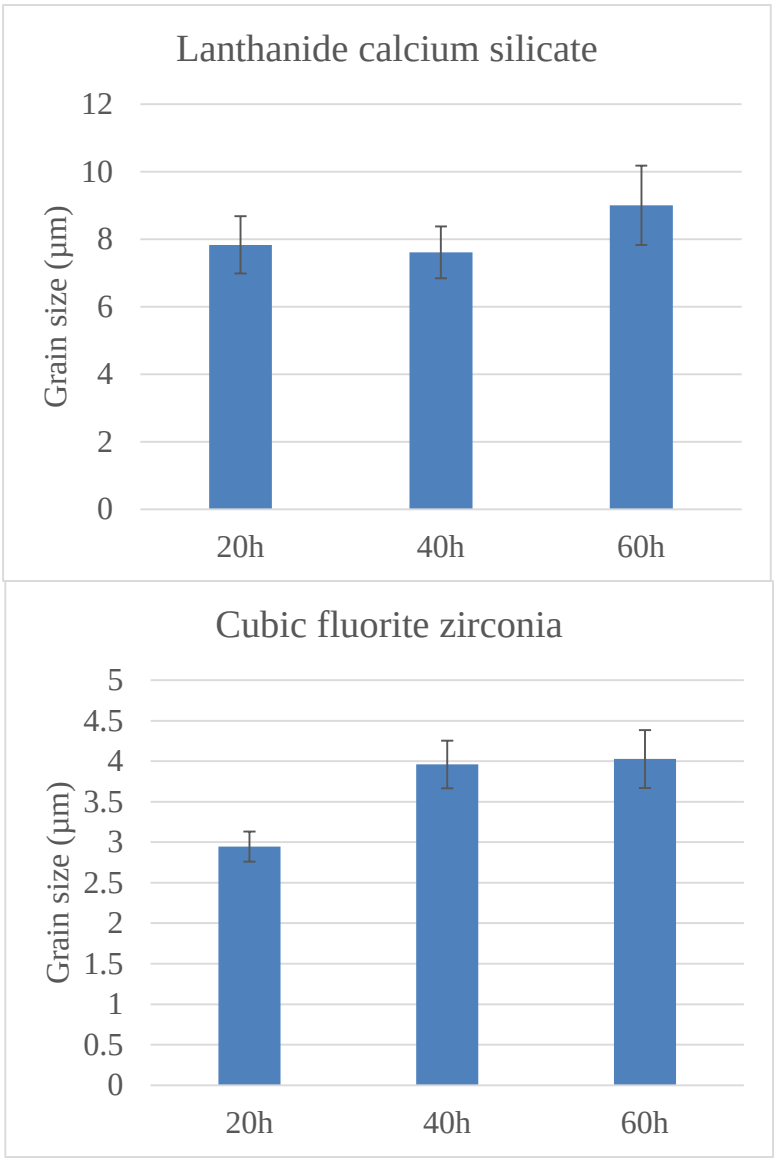

Figure 4.24 Grain size of lanthanide calcium silicate and cubic fluorite zirconia in $(Gd_6Sm_4)_{0.2}Zr_2O_7$ after corrosion (data calculated from SEM images). Error bar represents standard deviation. 20 grains were picked for each phase.

$(Gd_8Sm_2)_{0.2}Zr_2O7$ after CMAS – 1 corrosion for 20h, 40h and 60h at 1200°C are shown in Figure 4.25 and the grain size data are shown in Figure 4.26.

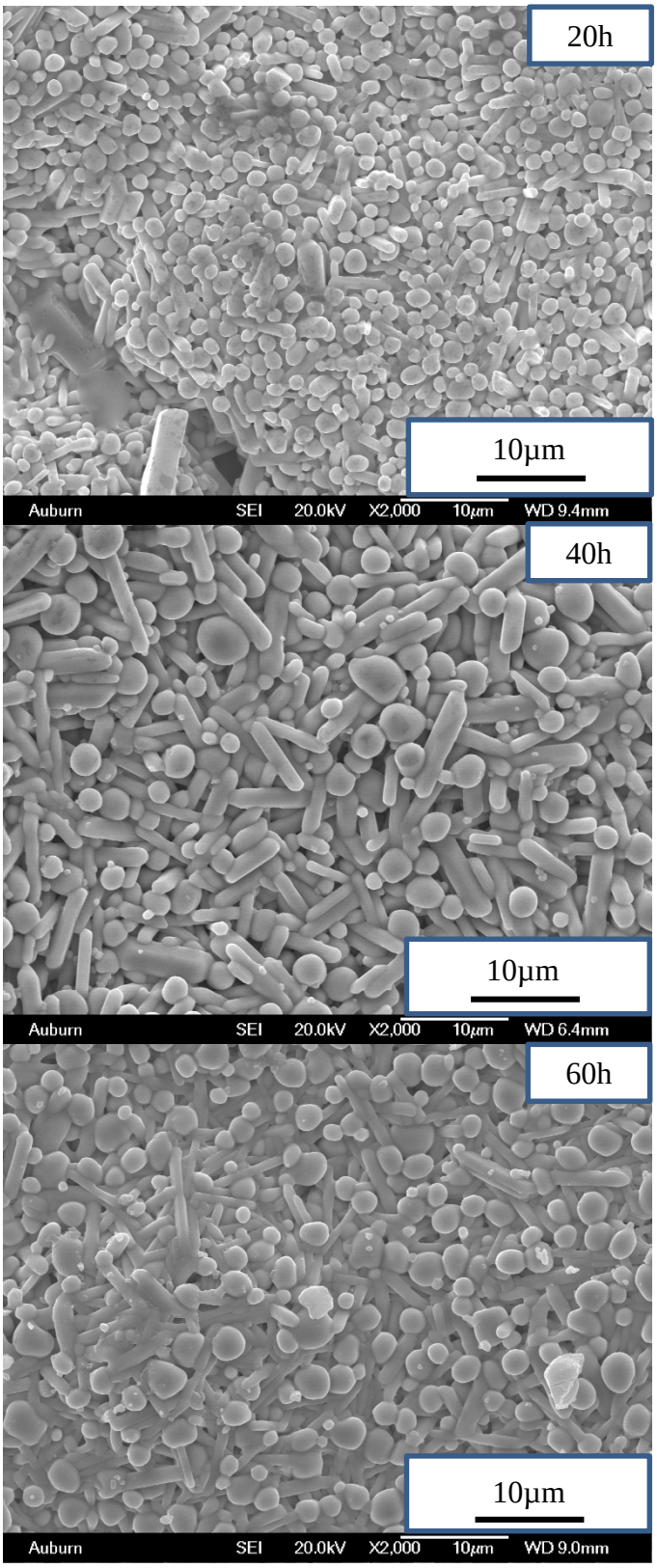

Figure 4.25 $(Gd_8Sm_2)_{0.2}Zr_2O_7$ after CMAS corrosion at 1200°C for 20h, 40h and 60h.

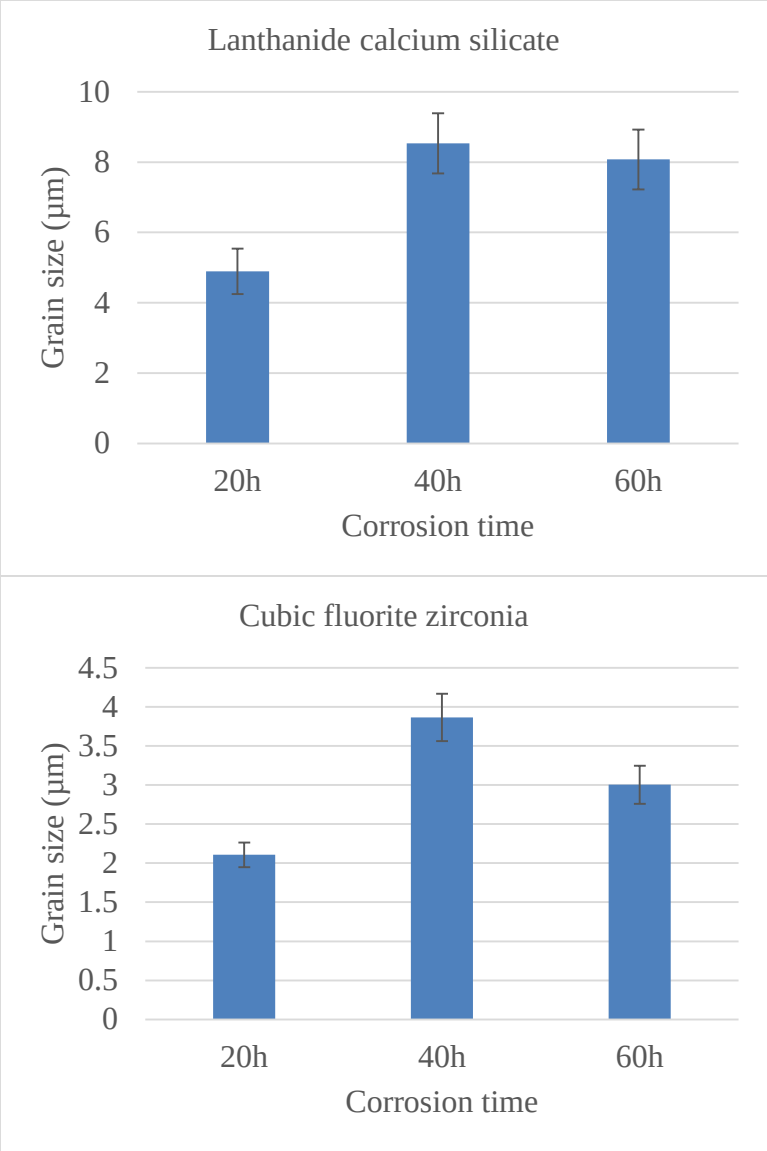

Figure 4.26 Grain size of lanthanide calcium silicate and cubic fluorite zirconia in $(Gd_8Sm_2)_{0.2}Zr_2O_7$ after corrosion (data calculated from SEM images). Error bar represents standard deviation. 20 grains were picked for each phase.

From Figure 4.22, Figure 4.24 and Figure 4.26, it is shown that all the grain size in 60 hours is larger than that in 20 hours for every composition. It can be concluded that although the grain size might drop in some certain circumstances, the grain size still has a trend in increasing, both for lanthanide calcium silicates and cubic fluorite zirconia.

4.3. Mixed temperature

To understand the reaction mechanism more clearly, the pyrochlore samples were exposed with CMAS at 1300°C first to make sure the CMAS was molten totally. Then the corrosion temperature dropped to 1200°C for desired durations.

Figure 4.27 and Figure 4.28 show $Gd_2Zr_2O_7$ and $Sm_2Zr_2O_7$ corroded at 1300°C for 15 minutes first and then corroded at 1200°C for 20 hours. For $Gd_2Zr_2O_7$ samples, the reaction products were similar as the products in higher corrosion temperature. The long stick grains were gadolinium calcium silicate phase and the round shape grains were cubic fluorite zirconia phase. Additionally, the average ratio of Zr:Gd in cubic fluorite phase was close to the cubic fluorite zirconia phase corroded in 1300°C. For $Sm_2Zr_2O_7$ samples in Figure 4.28, the round shape phase in spectra 2, 4 and 6 were rich in Zr and it corresponded to the cubic fluorite zirconia. The long stick phase in spectra 1 and 5 were rich in Gd, Si and Ca, which corresponded to the gadolinium calcium silicate. The elemental ratio of gadolinium calcium silicate presented different as $Ca_2Gd_8(SiO_4)_6O_2$ and $Ca_2Sm_8(SiO_4)_6O_2$. The XRD pattern of this sample are shown in Figure 4.29. The single crystal $Mg_2Al_2Si_6Ca_6O_{23}$ did not appear in the samples corroded at 1300°C first. This illustrated that once the cubic fluorite zirconia and gadolinium calcium silicate phase were formed at higher temperature, $Mg_2Al_2Si_6Ca_6O_{23}$ single crystal would not form again. The reaction product cubic fluorite zirconia and lanthanide calcium silicate formed at higher temperature were stable to prevent forming $Mg_2Al_2Si_6Ca_6O_{23}$ single crystal.

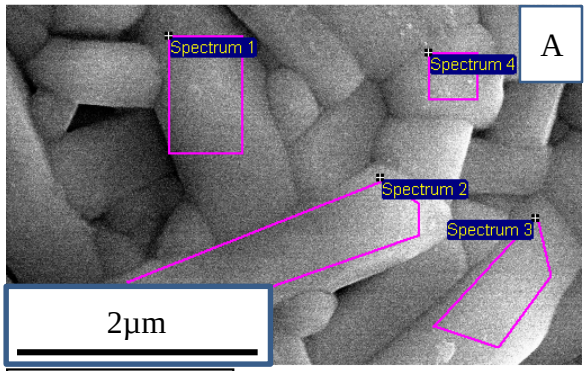

Spectrum	Al	Si	Ca	Zr	Gd
1	0	14	7	1	18
2	3	12	5	1	13
3	1	13	5	1	12
4	1	13	5	0	13

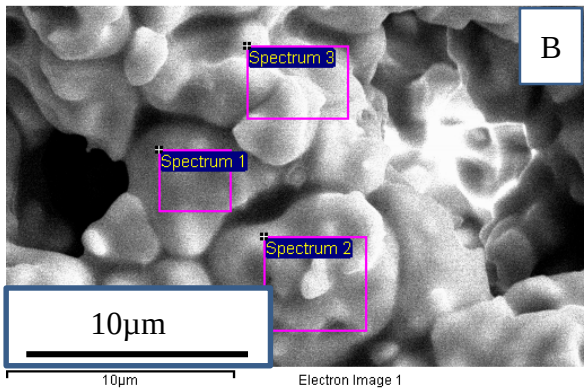

Spectrum	Al	Si	Ca	Zr	Gd
1	1	1	2	27	5
2	1	1	2	23	4
3	1	2	2	25	6

Figure 4.27 Elemental distribution of different phases in $Gd_2Zr_2O_7$ after corrosion at 1300°C for 15 minutes and 1200°C for 20 hours. (A) is the long shape grains and (B) is the round shape grains. All the values are in atomic ratio.

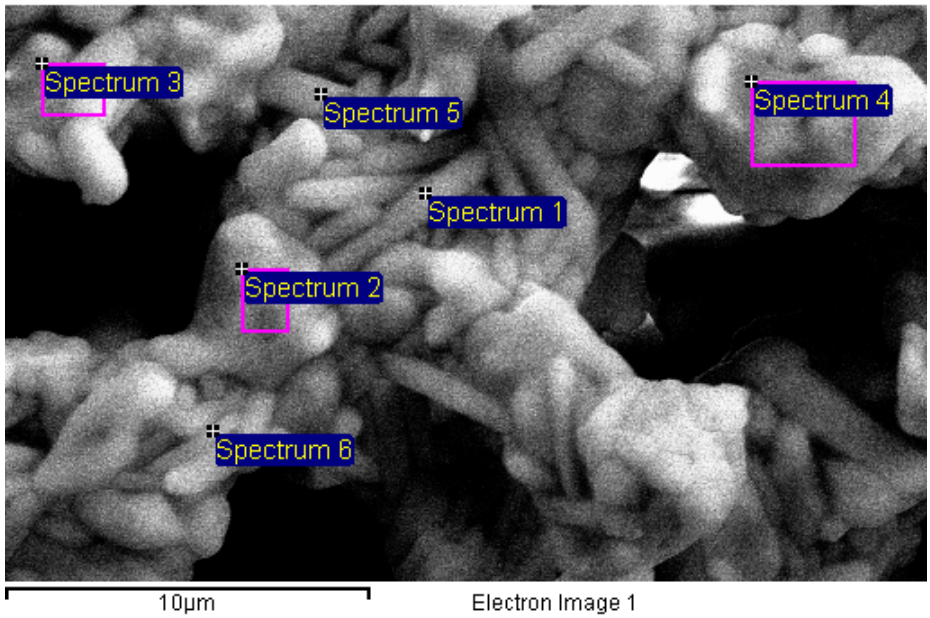

Spectrum	Al	Si	Ca	Zr	Gd
1	0	10	6	6	23
2	0	2	4	38	7
3	0	7	7	15	15
4	0	2	3	32	6
5	0	8	7	12	25
6	1	4	4	26	7

Figure 4.28 Elemental distribution of different phases in $Sm_2Zr_2O_7$ after corrosion at 1300°C for 15 minutes and 1200°C for 20 hours.

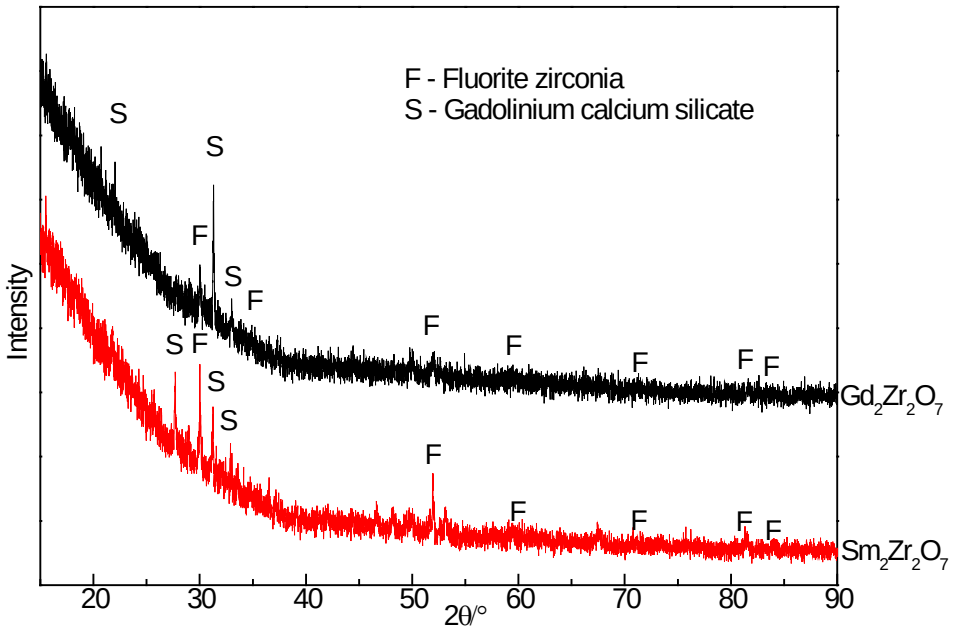

Figure 4.29 XRD pattern of $Gd_2Zr_2O_7$ and $Sm_2Zr_2O_7$ after two steps of corrosion: 1300°C for 15 minutes and then 1200°C for 20 hours.

4.4. CMAS corrosion with high porosity materials

4.4.1. Low temperature (<1250°C)

The XRD pattern of $Gd_2Zr_2O_7$ in different porosities after CMAS corrosion at 1215°C are shown in Figure 4.30 and Figure 4.31. The CMAS were also in two compositions: CMAS – 1 and CMAS – 2 (see in 2.1.3). The single crystal $Mg_2Al_2Si_6Ca_6O_{23}$ only appeared after CMAS – 1 corrosion on low porosity (19%) samples. Lower porosity means less CMAS infiltration into the ceramics and the remaining CMAS on top of pyrochlore materials could form $Mg_2Al_2Si_6Ca_6O_{23}$ single crystal in the cooling process. Additionally, since no $Mg_2Al_2Si_6Ca_6O_{23}$ single crystal formed after CMAS – 2 corrosion, no matter for high porosity and low porosity, it is believed that higher Al amount in CMAS inhibited formation of $Mg_2Al_2Si_6Ca_6O_{23}$ single crystal.

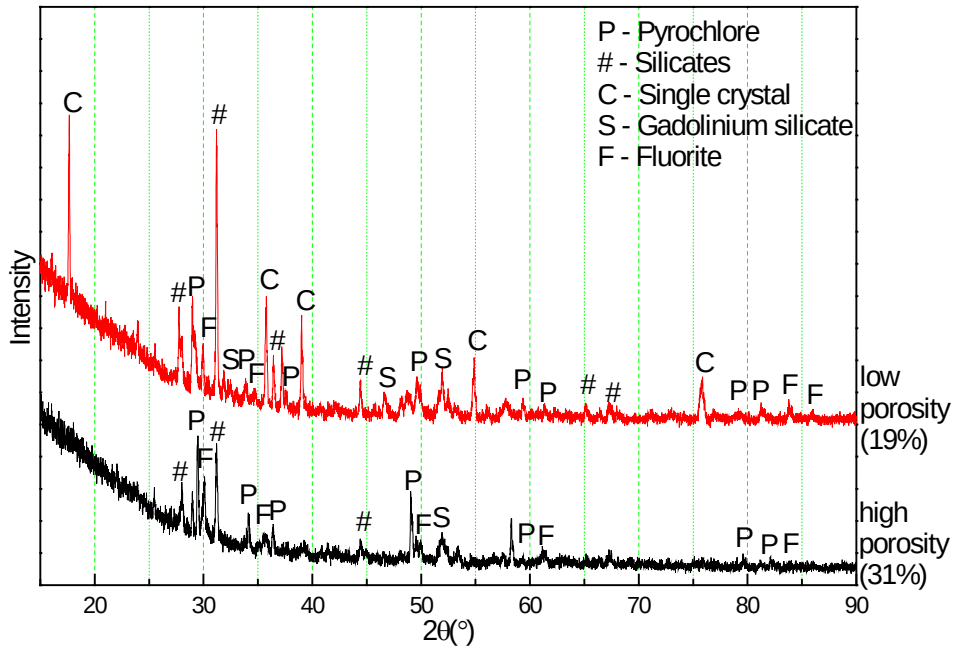

Figure 4.30 XRD pattern of $Gd_2Zr_2O_7$ with different porosities after CMAS – 1 corrosion at 1215°C for 10 hours.

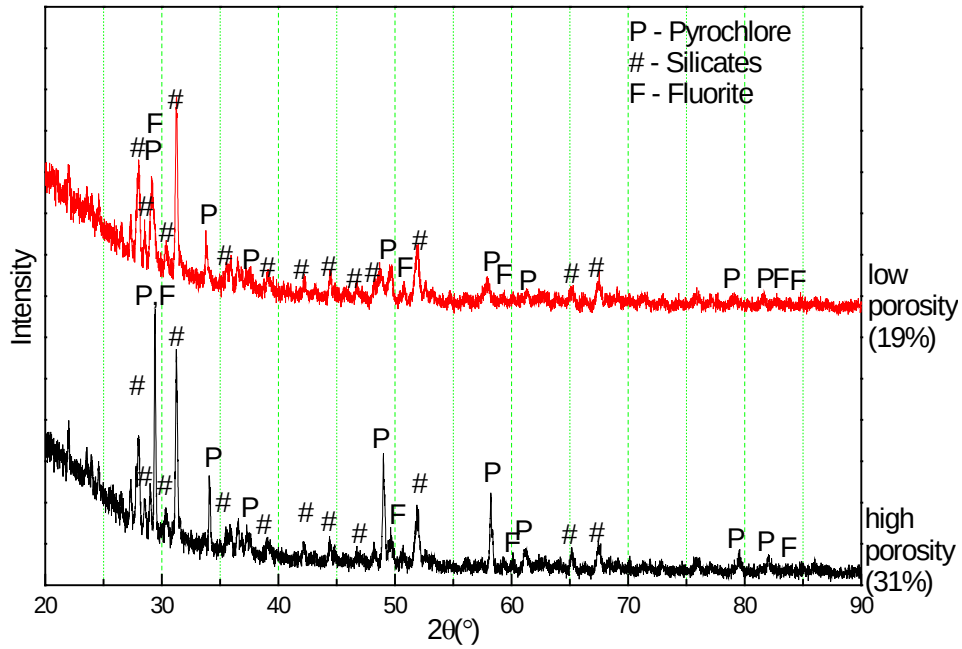

Figure 4.31 XRD pattern of $Gd_2Zr_2O_7$ with different porosities after CMAS – 2 corrosion at 1215°C for 10 hours.

4.4.2. High temperature (>1250°C)

The XRD pattern of $Gd_2Zr_2O_7$ in different porosities (19% and 31%) after CMAS corrosion at 1300°C are shown in Figure 4.32 and Figure 4.33. The CMAS were divided into two compositions: CMAS – 1 and CMAS – 2 (composition was shown in 2.1.3). The reaction products did not change much as the CMAS compositions and ceramic porosities changed. So compared with low temperature corrosion (<1250°C), the composition in molten CMAS did not affect the reaction products.

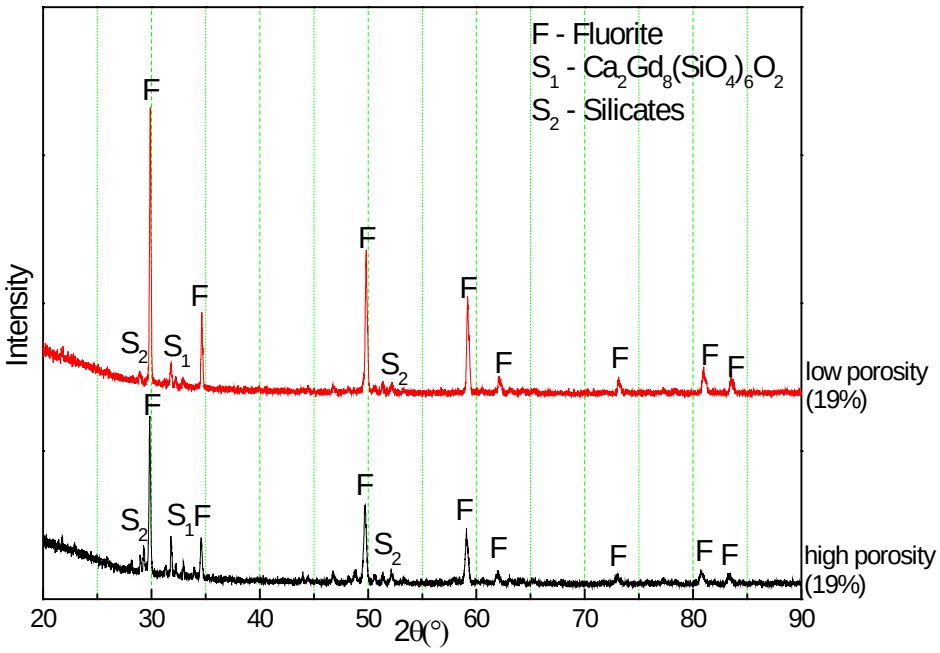

Figure 4.32 XRD pattern of $Gd_2Zr_2O_7$ with different porosities after CMAS – 1 corrosion at 1300°C for 20 hours.

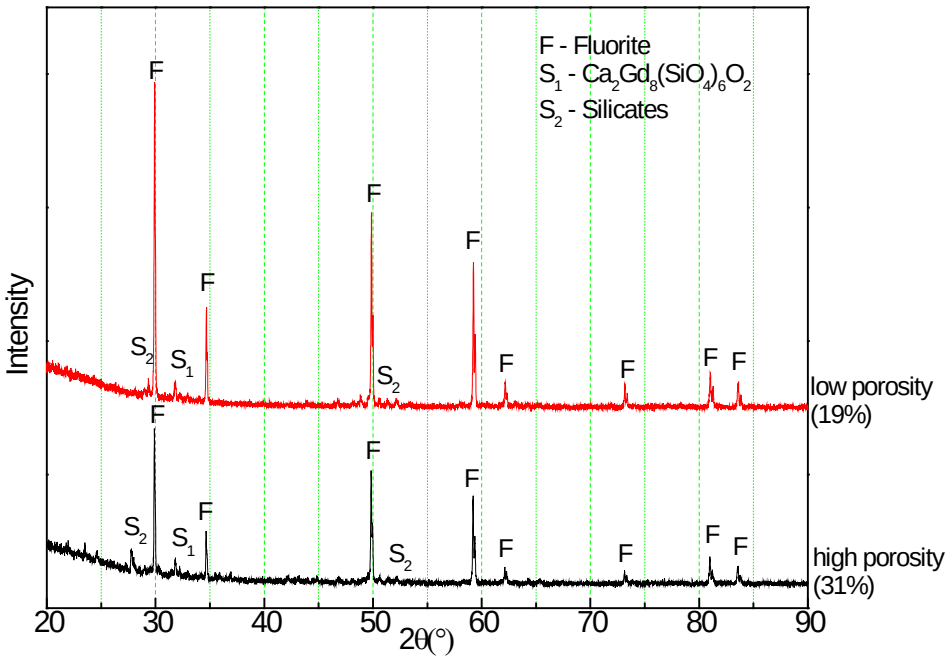

Figure 4.33 XRD pattern of $Gd_2Zr_2O_7$ with different porosities after CMAS – 2 corrosion at 1300°C for 20 hours.

4.5. CMAS corrosion at moisture atmosphere

Water could be injected into the engines and then affect the engines' working condition. So the CMAS corrosion mechanism at moisture atmosphere needs to be studied.

4.5.1. Low temperature (<1250°C)

The XRD pattern of $Gd_2Zr_2O_7$ with low porosity (19%) after CMAS – 1 corrosion with and without water flow are shown in Figure 4.34. The peaks of cubic fluorite phase and silicates had similar strength but the peaks of $Mg_2Al_2Si_6Ca_6O_{23}$ had a much larger strength when corroded with water flow. This illustrated that the cubic fluorite phase and silicates did not change much in grain size with and without water flow, but the $Mg_2Al_2Si_6Ca_6O_{23}$ tended to form much larger grains in moisture atmosphere corrosion.

This is constituent with the data shown in Figure 4.35. The grain size of $Mg_2Al_2Si_6Ca_6O_{23}$ single crystal was calculated in the same method mentioned in 4.2.2.

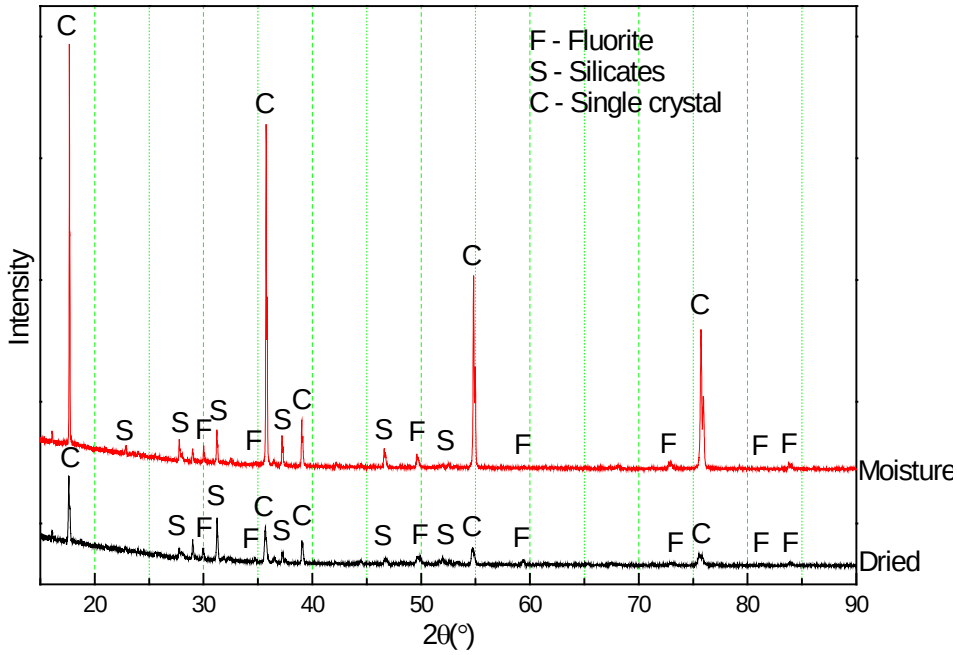

Figure 4.34 XRD pattern of $Gd_2Zr_2O_7$ after CMAS corrosion at 1200°C for 10 hours. The up line is corrosion with water flow and the bottom line is corrosion without water flow.

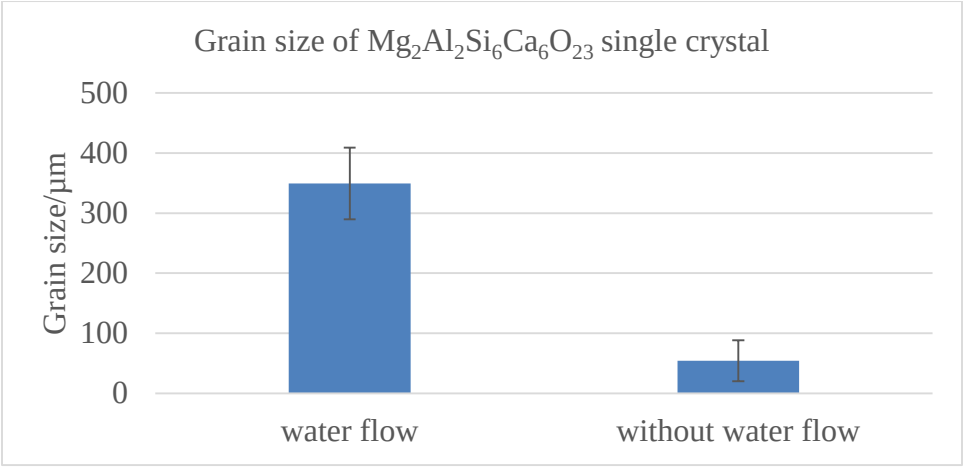

Figure 4.35 Grain size of $Mg_2Al_2Si_6Ca_6O_{23}$ single crystal in microns. Samples are $Gd_2Zr_2O_7$ after CMAS – 1 corrosion at 1200°C for 10 hours. Error bar represents

standard deviation (related images can be found in Appendix V). 20 grains were picked for each phase.

4.5.2. High temperature (>1250°C)

The compared XRD pattern of $Gd_2Zr_2O_7$ corrosion at moisture atmosphere and dried atmosphere at various conditions are shown from Figure 4.36 to Figure 4.39. The reaction products were cubic fluorite phase and silicates phases both at moisture atmosphere and dried atmosphere. The peaks' position and strength did not have obvious difference in the corrosion process with and without water flow, which were consistent with the corrosion test at lower temperature (1200°C).

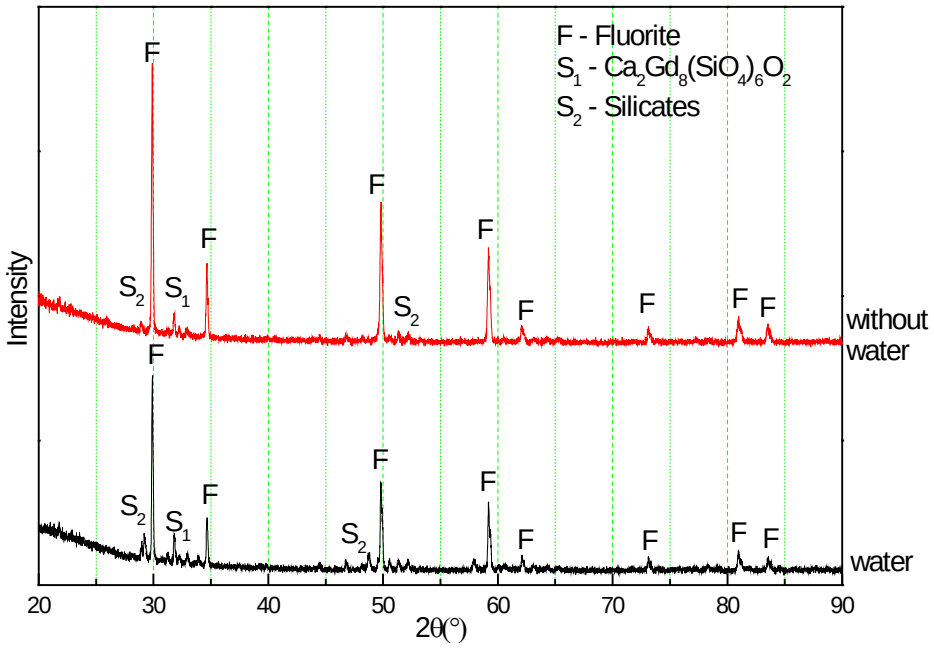

Figure 4.36 XRD pattern of $Gd_2Zr_2O_7$ in low porosity (19%) with CMAS – 1 exposure at 1300°C for 10 hours.

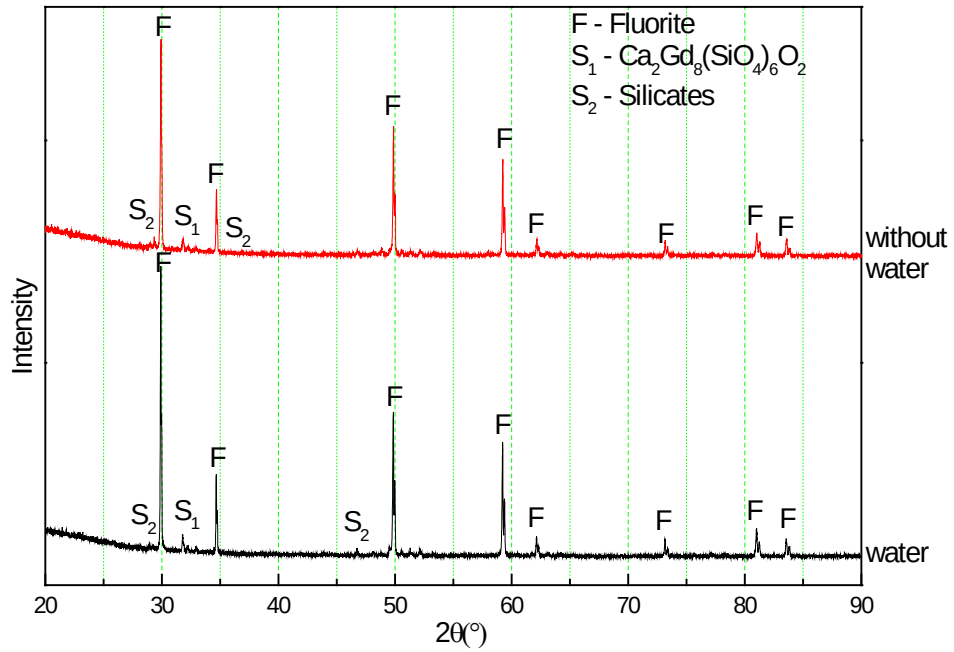

Figure 4.37 XRD pattern of $Gd_2Zr_2O_7$ in low porosity (19%) with CMAS – 2 exposure at 1300°C for 10 hours.

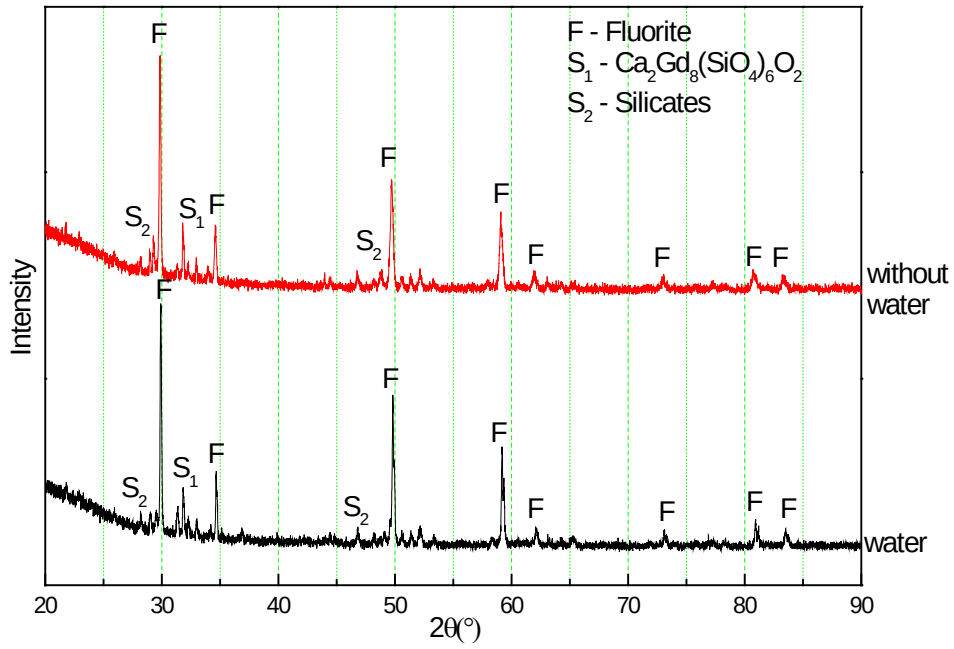

Figure 4.38 XRD pattern of $Gd_2Zr_2O_7$ in high porosity (31%) with CMAS – 1 exposure at 1300°C for 10 hours.

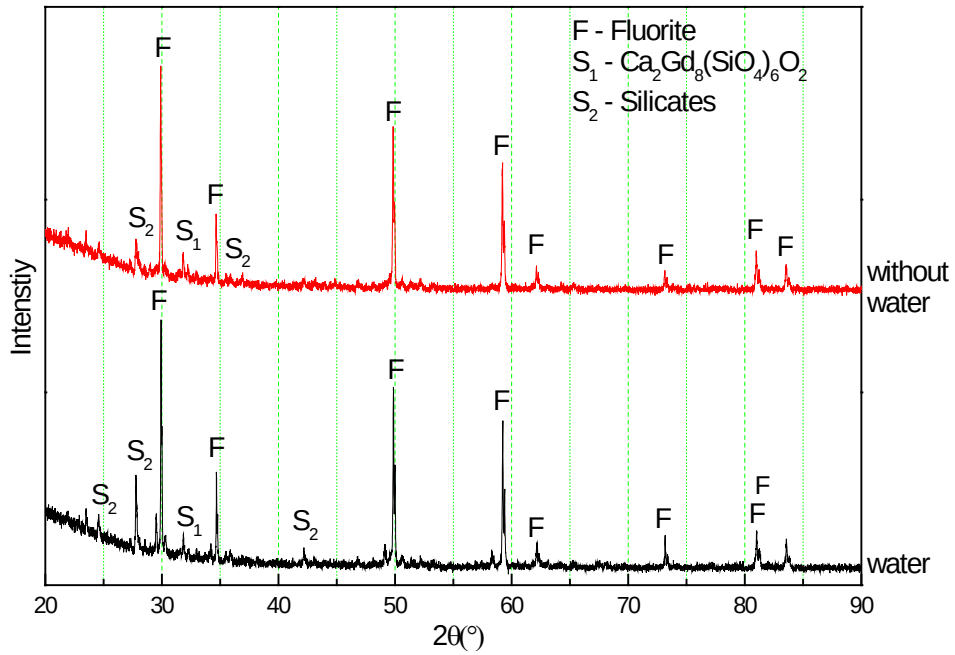

Figure 4.39 XRD pattern of $Gd_2Zr_2O_7$ in high porosity (31%) with CMAS – 2 exposure at 1300°C for 10 hours.

4.6. Conclusion

The reaction mechanism between CMAS and pyrochlore materials keeps similar at either high temperature (>1250°C) or low temperature (<1250°C). As mentioned in section 4.1 and section 4.2. The lanthanide element in pyrochlore materials would dissolve in molten CMAS and then reacted with CMAS to form calcium lanthanide silicate. This silicate phase was rich in lanthanide, calcium and silicon elements. The rest part of pyrochlore materials would form a cubic fluorite phase rich zirconia. Due to the decreased in ionic radius, the lattice parameter of cubic fluorite structure was also lower than the pyrochlore structure. Additionally, as discussed in section 4.1.2, the ratio of Zr:Gd/Sm would decrease which was consistent with the phase diagram.

Although the reaction mechanism keeps similar, extra CMAS would form another phases at lower corrosion temperature (<1250°C) which is shown in section 4.2.1. $CaAl_2Si_2O_8$ and $Mg_2Al_2Si_6Ca_6O_{23}$ single crystal with large grain size could form after CMAS corrosion at 1200°C and these phases have a much larger size than calcium lanthanide silicate and cubic fluorite zirconia. Additionally, combined the discussion in section 4.2.1 and section 4.4, the formation of $Mg_2Al_2Si_6Ca_6O_{23}$ single crystal should meet the requirements simultaneously:

- Pyrochlore materials with relatively lower porosity (about 19%);
- CMAS that contained less Al;
- Lower corrosion temperature (<1250°C).

As mentioned in section 4.3, once the CMAS was molten at elevated temperatures, the reaction product cubic fluorite zirconia and lanthanide calcium silicate were stable and the single crystal would not form again, even when the corrosion temperature decreased. The CMAS corrosion reaction products could be concluded as Table 4.7 and Table 4.8 shows.

Table 4.7. Corrosion reaction between CMAS and pyrochlore materials at high corrosion temperature (>1250°C)

Materials	Corrosion temperature	Reaction product	Grain size
$Gd_2Zr_2O_7$	1300°C	Cubic fluorite zirconia	2~4 μm
		$Ca_2Gd_8(SiO_4)_6O_2$	10 μm
	1400°C	Cubic fluorite zirconia	2~3 μm
		$Ca_2Gd_8(SiO_4)_6O_2$	5~8 μm

	1500°C	Cubic fluorite zirconia	10 μm
		$Ca_2Gd_8(SiO_4)_6O_2$	30~50 μm
$Sm_2Zr_2O_7$	1300°C	Cubic fluorite zirconia	2~4 μm
		$Ca_2Sm_8(SiO_4)_6O_2$	10 μm
	1400°C	Cubic fluorite zirconia	2~3 μm
		$Ca_2Sm_8(SiO_4)_6O_2$	5~8 μm
	1500°C	Cubic fluorite zirconia	4~6 μm
		$Ca_2Sm_8(SiO_4)_6O_2$	15~20 μm

Table 4.8. Corrosion reaction between CMAS and pyrochlore materials at low temperature (1200°C)

Materials	Reaction product	Shape	Grain size
$Gd_2Zr_2O_7$	Cubic fluorite zirconia	Round	2~5 μm
	$Ca_2Gd_8(SiO_4)_6O_2$	Bar	10~15 μm
	$CaAl_2Si_2O_8$	Bar	50 μm
	$Mg_2Al_2Si_6Ca_6O_{23}$	Cubic or bar	>100 μm

Furthermore, the moisture atmosphere only affected the formation of $Mg_2Al_2Si_6Ca_6O_{23}$ single crystal, which is shown in section 4.5. Water flow helped to form much larger crystal size than the dried atmosphere. But the water flow had almost none effect in forming other phases.

CHAPTER 5. Quantification of corrosion

Quantification of CMAS corrosion on thermal barrier materials was determined by the depth of reaction layer and the images of cross-section were used. The properties of YSZ and pyrochlore materials' reaction layer are discussed in this chapter.

5.1. Cross-section of YSZ

A detailed cross-section image of YSZ after corrosion at 1200°C for 20 hours is shown in Figure 5.1. The cross-section of YSZ was divided into three layers, including a dense reaction layer, porous transaction layer and YSZ layer. A clear boundary existed between reaction layer and transition layer. The linear elemental distribution of cross-section is shown in Figure 5.2. CMAS dominated in the top layer and dropped slowly. Then the transition layer was mixed with CMAS and zirconia. Furthermore, the pores in transition layer would allow the infiltration of extra CMAS in the future corrosion process and did not have the function of preventing further corrosion. In the YSZ layer, the amount of CMAS dropped to almost zero and the amount of Zr raised to normal value.

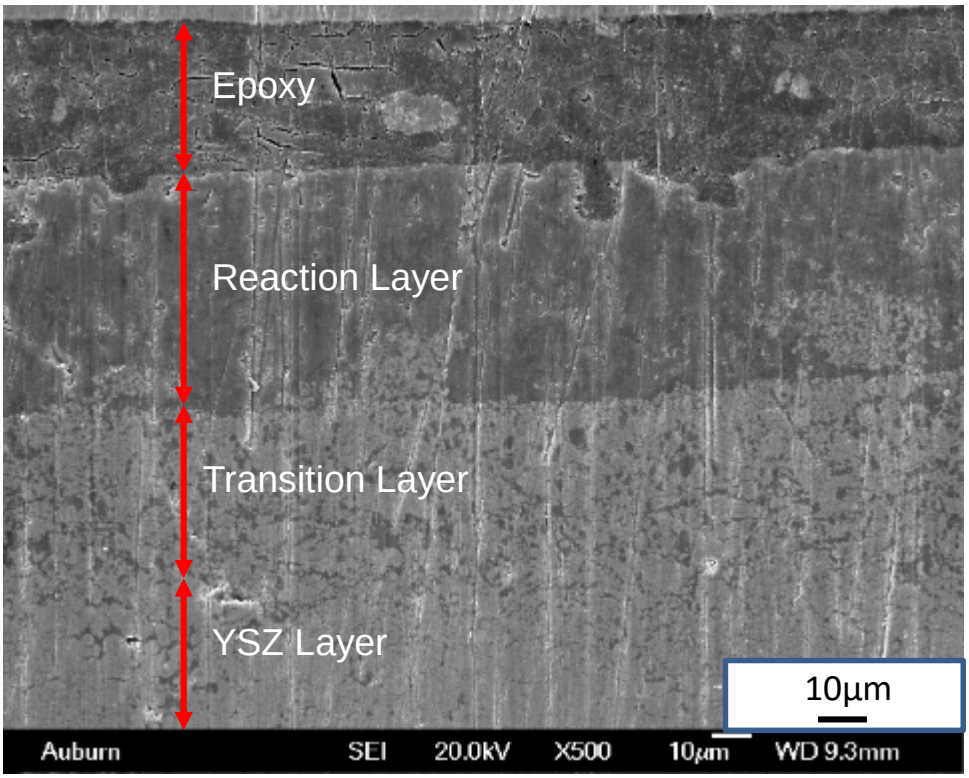

Figure 5.1 Cross-section of YSZ after corrosion at 1200°C for 20 hours.

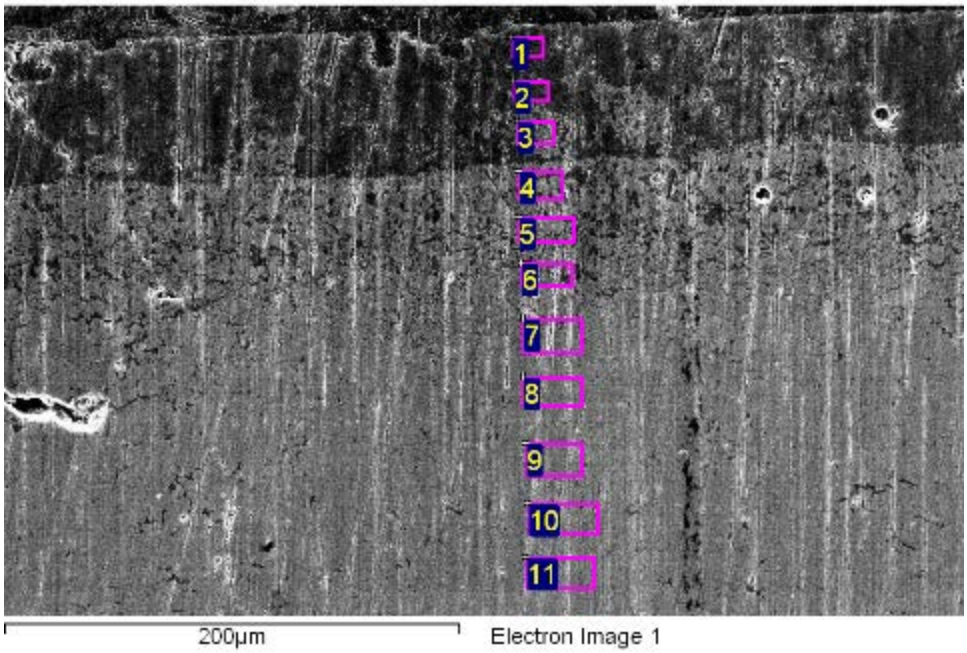

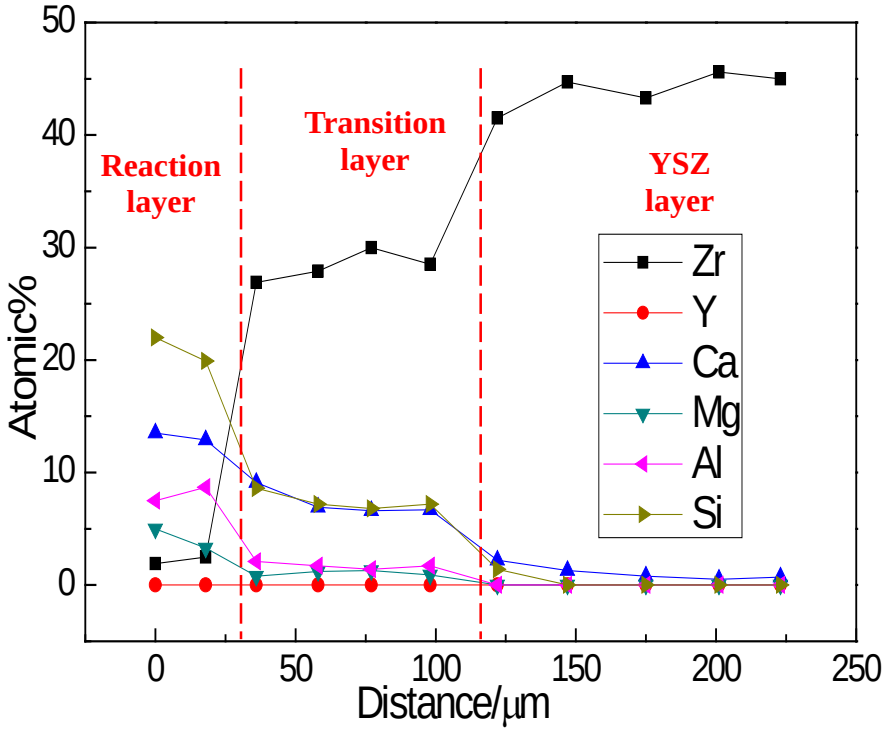

Figure 5.2 Linear elemental distribution of YSZ after corrosion at 1200°C for 20 hours.

5.2. Cross-section of pyrochlore materials

The cross-section images of $Gd_2Zr_2O_7$ and $Sm_2Zr_2O_7$ after corrosion at 1200°C for 20 hours are shown in Figure 5.3 and Figure 5.4. Different as YSZ, no porous transition layers existed both in $Gd_2Zr_2O_7$ and $Sm_2Zr_2O_7$ after corrosion. A clear boundary separated the reaction layer and pyrochlore layer. The linear elemental distribution images done by EDS are shown in Figure 5.5 and Figure 5.6. The reaction layers of pyrochlore materials presented similar result as the reaction layer of YSZ. CMAS dominated in the top layer and dropped slowly. When crossing the clear boundary, the amount of CMAS suddenly dropped to almost zero and the value of Gd and Zr raised to normal value. The dense reaction layer can prevent further infiltration of extra CMAS and improve corrosion resistance.

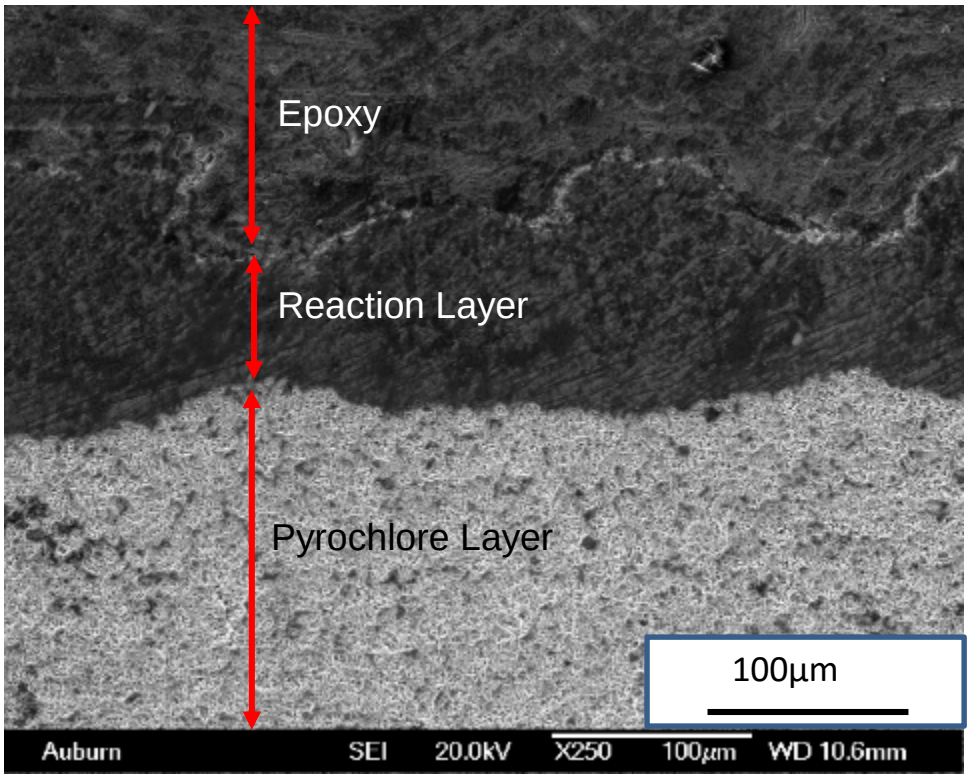

Figure 5.3 Cross-section of $Gd_2Zr_2O_7$ after corrosion at 1200°C for 20 hours.

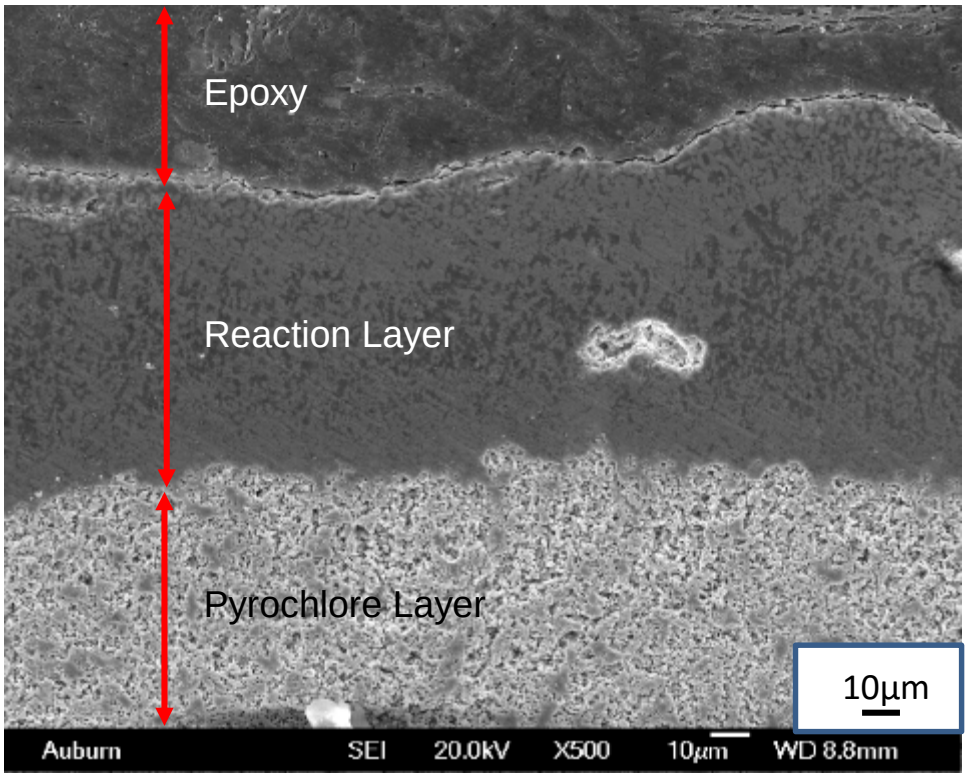

Figure 5.4 Cross-section of $Sm_2Zr_2O_7$ after corrosion at 1200°C for 20 hours.

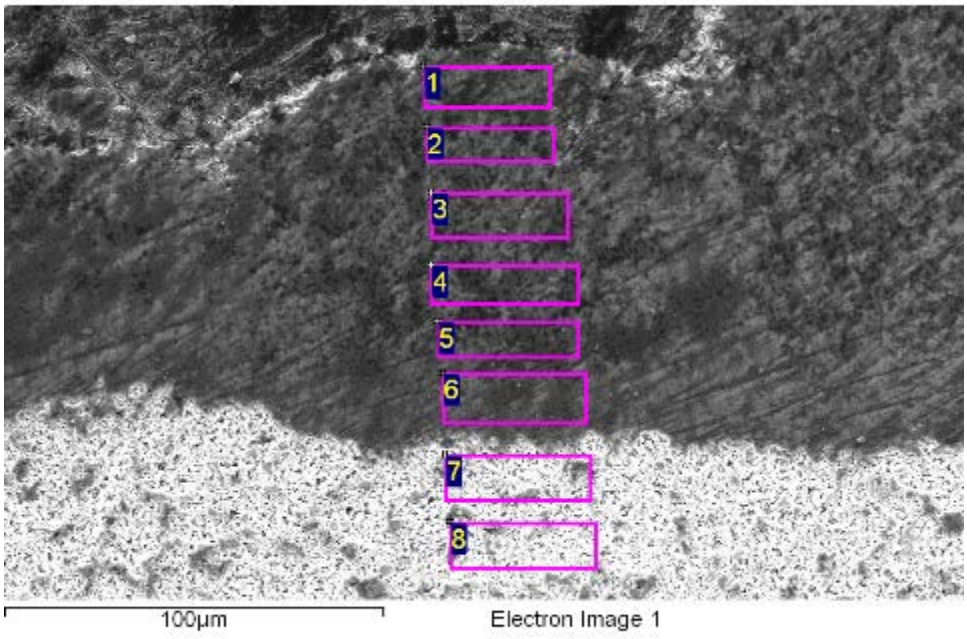

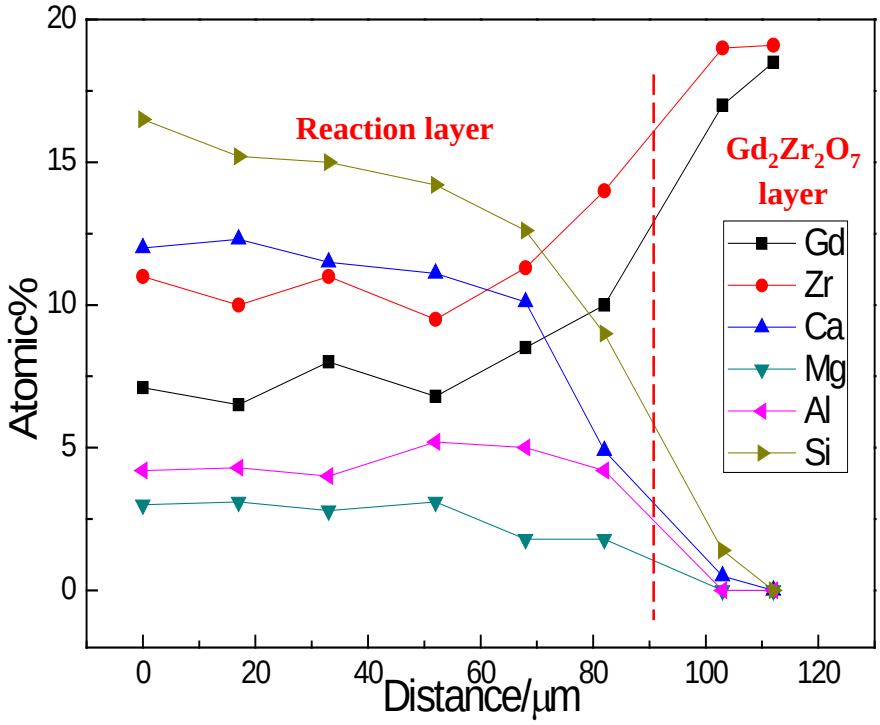

Figure 5.5 Linear elemental distribution of $Gd_2Zr_2O_7$ after corrosion at 1200°C for 20 hours.

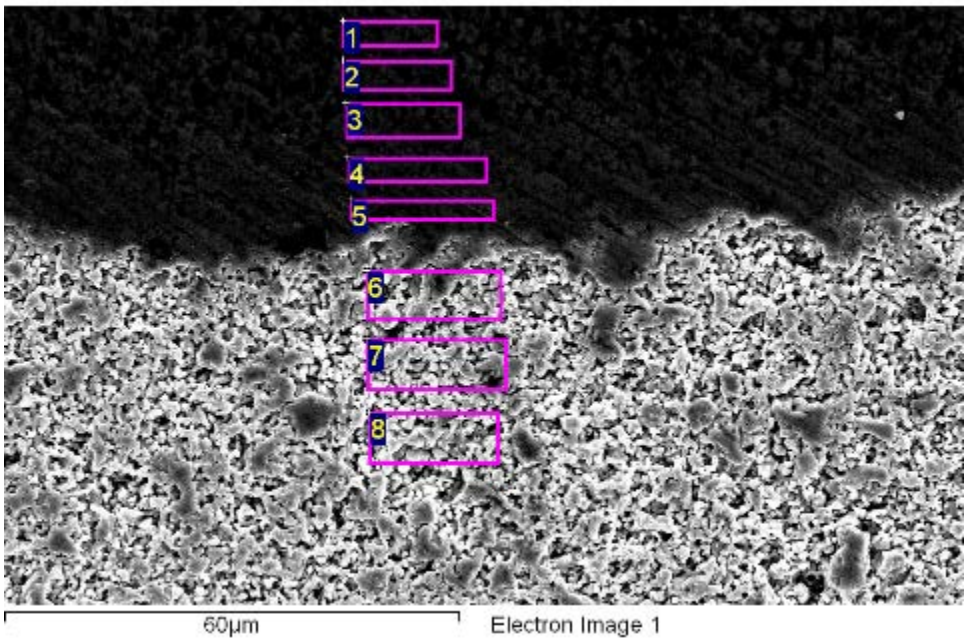

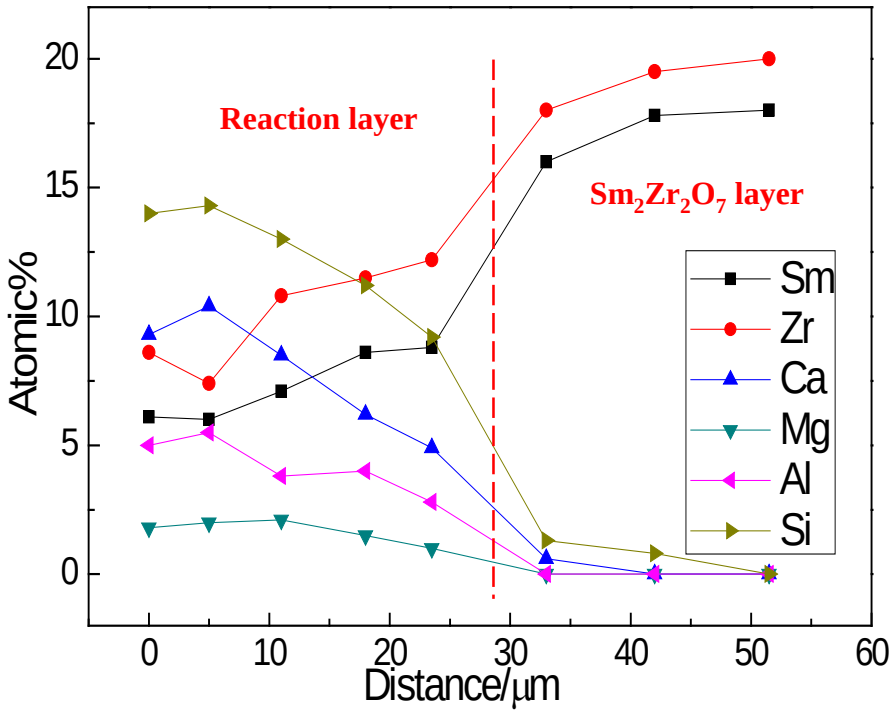

Figure 5.6 Linear elemental distribution of $Sm_2Zr_2O_7$ after corrosion at 1200°C for 20 hours.

Detailed images focused on the boundaries of reaction layer and pyrochlore layer are shown in Figure 5.7 and Figure 5.8. The boundary separate the reaction layer which contained most CMAS and dropped to almost zero in the pyrochlore layer.

Figure 5.9 shows the reaction layer of $Sm_2Zr_2O_7$ after corrosion at high magnification. The appeared spherical phase and bar-shaped phase corresponded to the morphology in the surface. The ball-shaped phase is mainly fluorite phase which is rich in Zr; the bar-shaped phase is apatite silicate phase which is rich in Si, Ca and Sm. The black background is CMAS glass.

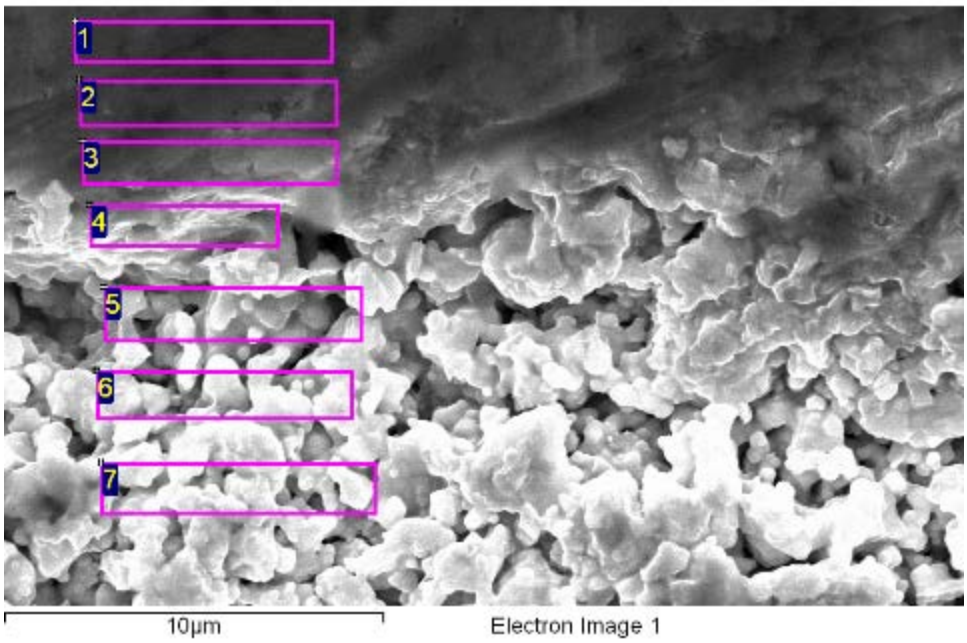

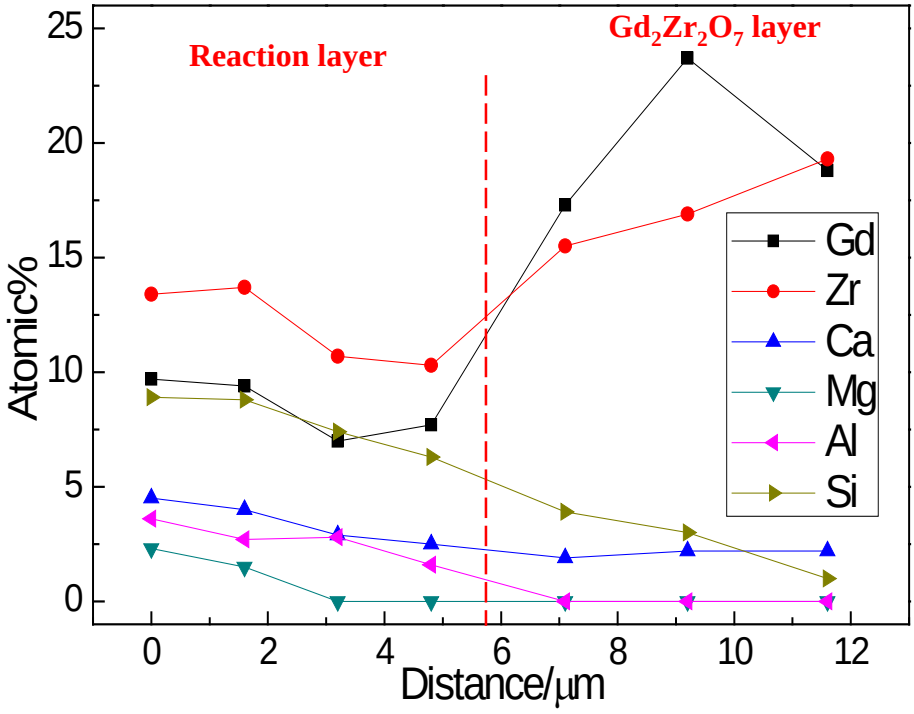

Figure 5.7 Elemental distribution at the boundary of reaction layer and $Gd_2Zr_2O_7$.

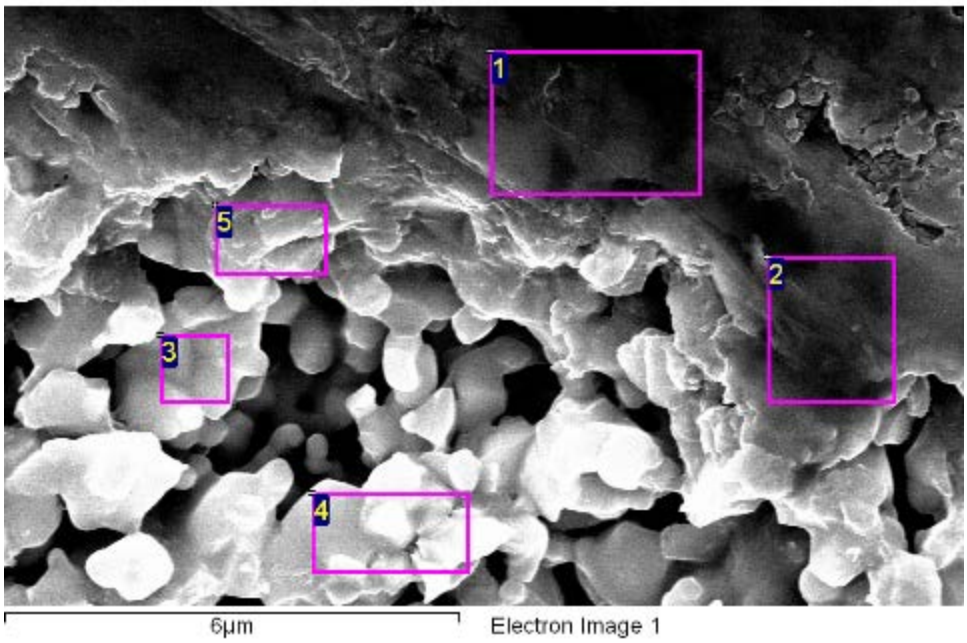

Spectrum	Mg	Al	Si	Ca	Zr	Sm
1	2	4	10	5	11	9
2	0	3	4	2	15	11
3	0	0	1	0	17	12
4	0	0	1	1	17	13
5	0	1	4	1	12	9

Figure 5.8 Elemental distribution of boundary between reaction layer and $Sm_2Zr_2O_7$.

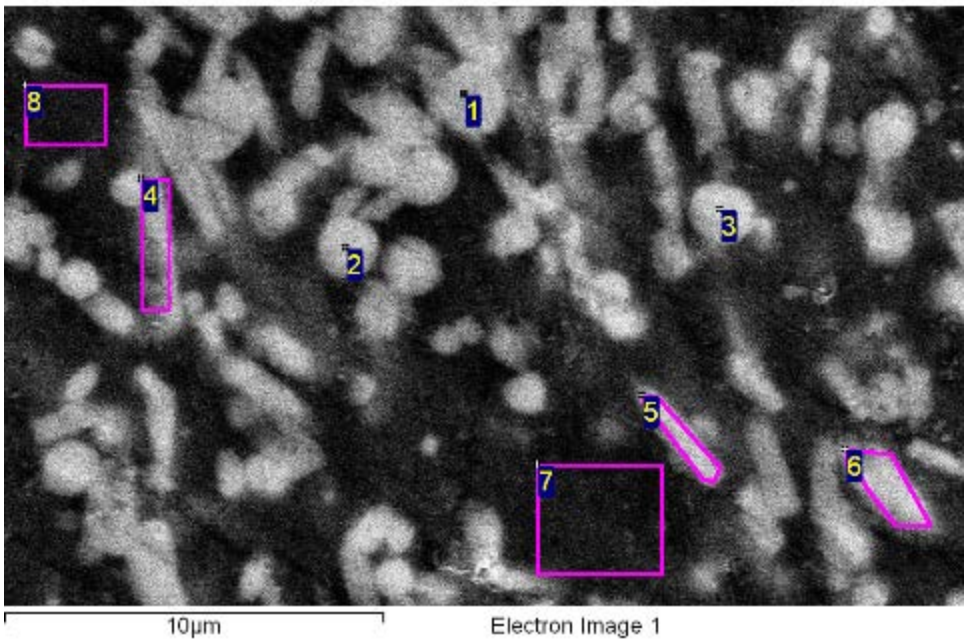

Spectrum	Mg	Al	Si	Ca	Zr	Sm
1	0	1	3	4	29	4
2	1	1	5	5	26	3
3	1	1	6	6	24	4
4	3	5	18	10	5	8
5	2	5	18	8	3	8
6	0	5	18	8	4	9
7	5	6	17	16	1	1
8	3	9	18	14	1	1

Figure 5.9 Reaction layer at high magnification of $Sm_2Zr_2O_7$ after corrosion at 1200°C for 20 hours.

5.3. Re-corrosion with extra CMAS

To understand the function of reaction layer well, the re-corrosion test with extra CMAS is necessary. Firstly, the $Gd_2Zr_2O_7$ sample was corroded with CMAS in 20mg/cm_2. After reaction the sample was broken to two parts. Then extra CMAS powders with same amount of 20mg/cm_2 were applied on one part and corroded again. After second corrosion process, the two parts were both mounted in epoxy and grinded up to 2000 grits and then observed by SEM and EDS. The thickness of reaction layer was calculated by picking up 40 locations and the Student t-test is used to determine if the two thicknesses have significant difference.

The results of two processes' corrosion are shown in Figure 5.10 and Figure 5.11. From Figure 5.11, it is clear to see that a dense thin layer existed above the reaction layer. The detailed image of the boundary in sample 2 with elemental information is shown in Figure 5.12. The dense layer had almost zero Zr and Gd and this layer was CMAS layer. Since sample 2 was corroded with extra CMAS powders, the dense reaction layer formed in the first corrosion step prevent further infiltration of extra CMAS powders and the extra CMAS formed an another dense layer above the reaction layer. The spherical phase and stick phase in the reaction layer also represented cubic fluorite zirconia and gadolinium silicate. The thickness of reaction layers are shown in Figure 5.13 (calculated from Figure 5.10 and Figure 5.11). The thickness of this two reaction layer were very close and the difference is less than 1 μm. According to the student t-test, the p-value equals 0.4976 (>0.05), which means this two layers did not have significant difference in thickness.

Compared with the reaction layer, the extra CMAS layer is much thinner (around 15 μm). Since the amount of CMAS used in the two corrosion steps were the same, it can be concluded that the infiltration depth of CMAS is much larger than the thickness of itself.

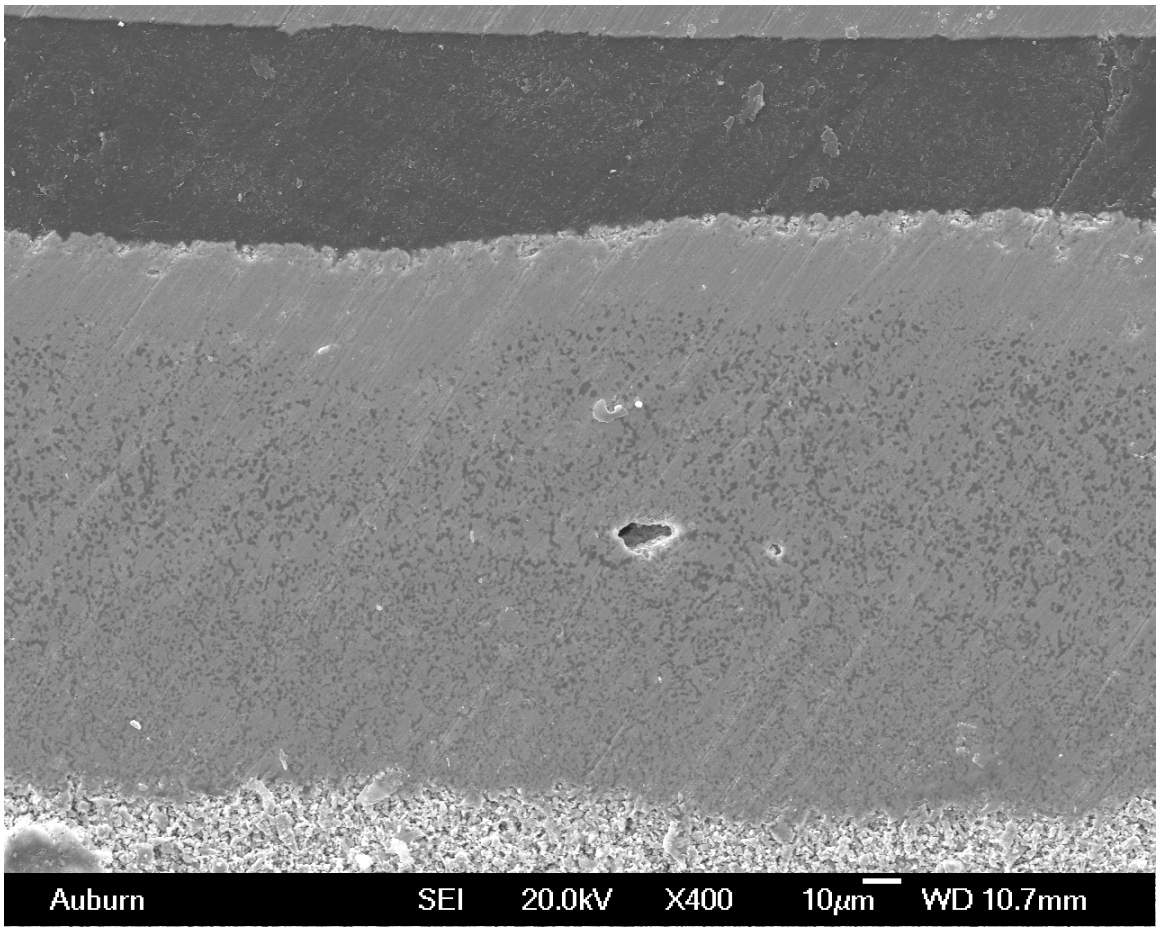

Figure 5.10 $Gd_2Zr_2O_7$ (sample 1) after CMAS – 1 corrosion at 1200°C for 20 hours.

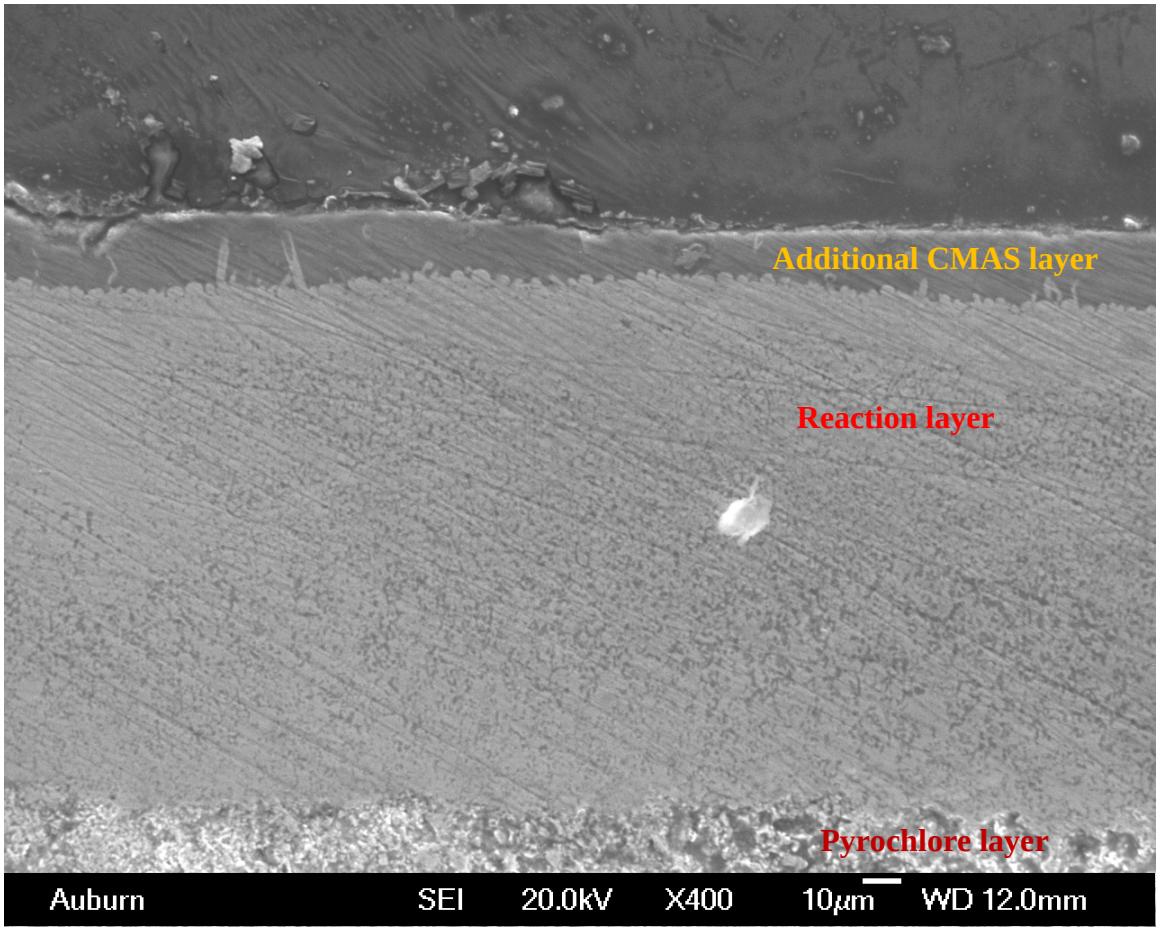

Figure 5.11 $Gd_2Zr_2O_7$ (sample 2) with two corrosion processes: firstly corroded with CMAS – 1 at 1200°C for 20 hours; secondly corroded with extra CMAS – 1 at 1200°C for another 20 hours.

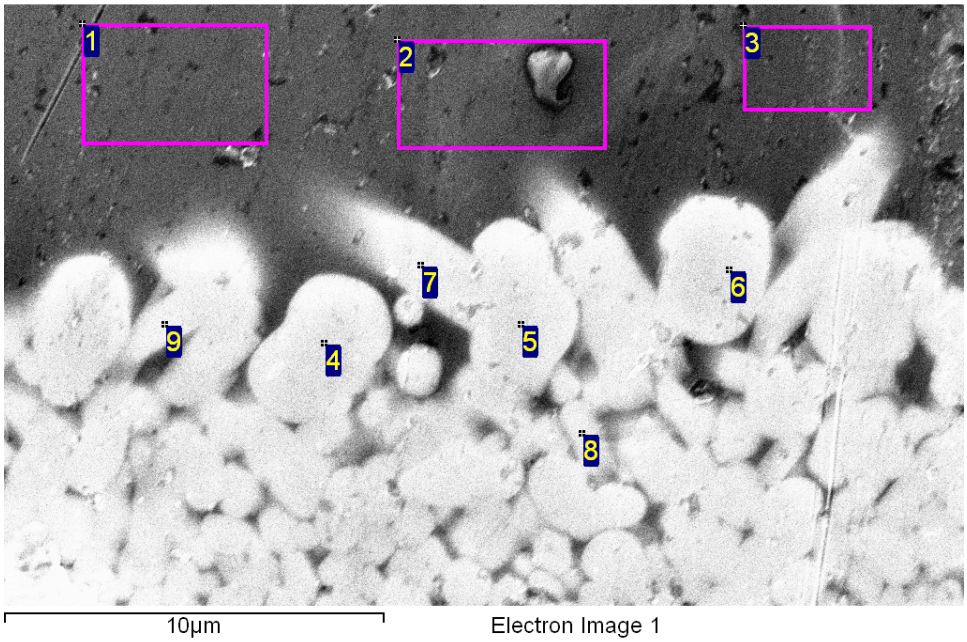

Spectrum	Mg	Al	Si	Ca	Zr	Gd	
1	**4**	**8**	**16**	**11**	1	1	**CMAS**
2	**3**	**8**	**16**	**9**	1	2	
3	**3**	**7**	**15**	**14**	1	0	
4	0	0	1	2	**29**	5	**Cubic fluorite zirconia**
5	0	0	1	2	**28**	5	
6	0	0	0	2	**30**	4	
7	0	1	**15**	7	2	**14**	**Gadolinium silicates**
8	0	2	**12**	5	7	**10**	
9	0	1	**12**	6	7	**11**	

Figure 5.12 Detailed image of CMAS and reaction layer with elemental information.

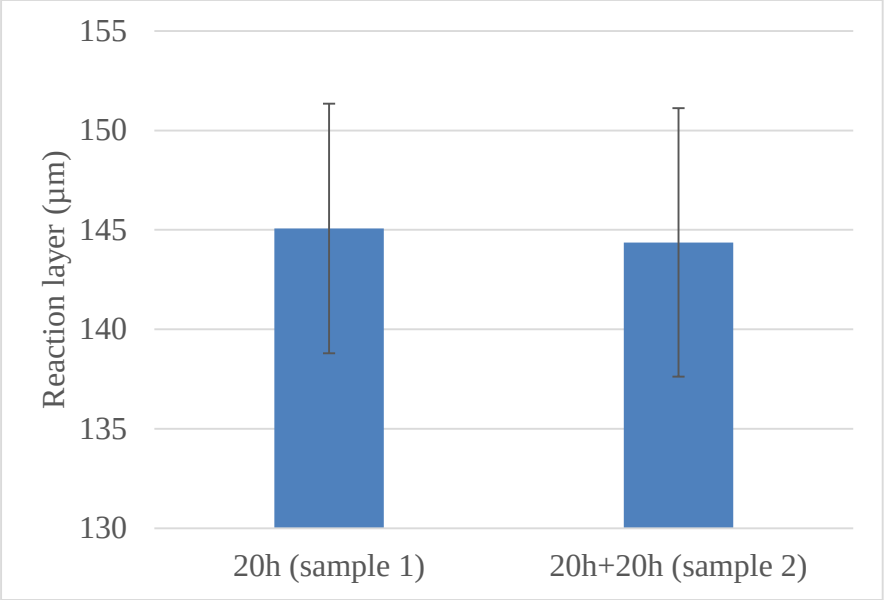

Figure 5.13 Thickness of reaction layers after 20 hours' corrosion and (20 + 20) hours' corrosion with extra CMAS. Error bar represents the standard deviation. P-value equals 0.4976 according to student t-test. 40 locations were picked for each case.

5.4. Re-corrosion without extra CMAS

Two steps of corrosion experiments were taken to study the reaction rate between CMAS and pyrochlore materials without extra CMAS. Firstly $Gd_2Zr_2O_7$ samples were corroded for 10 hours and 20 hours respectively and then the samples were broken into two parts. One part was chosen to take 40 hours' additional corrosion time. After all, the cross-section is observed in optical microscope to study the thickness of reaction layer. 40 locations were picked to calculate the average thickness and standard deviation for each sample. Additionally, the Student t-test is also used to determine the significance of difference.

The cross-section images of $Gd_2Zr_2O_7$ corroded by CMAS at 1200°C for 10 hours and (10 + 40) hours are shown in Figure 5.14. The average thickness of reaction layer is

shown in Figure 5.15. The reaction layer's thickness only increased around 3 μm with 40 additional corrosion hour. Compared with the original thickness (about 45 μm), the increase in thickness is much smaller, which means the reaction layer can stand stable in the further corrosion process.

The cross-section images of $Gd_2Zr_2O_7$ corroded by CMAS at 1200°C for 20 hours and (20+40) hours are shown in Figure 5.16. The average thickness of reaction layer is shown in Figure 5.17. The thickness of reaction layer increased only about 1 μm with 40 additional corrosion hours, and compared with the origin thickness (72 μm), the increase ratio is even smaller than the (10+40) hours' corrosion experiments. Additionally, the p-value of this two sets of data equals 0.1865 (>0.05), which means the thickness of this two reaction layers did not have significant difference.

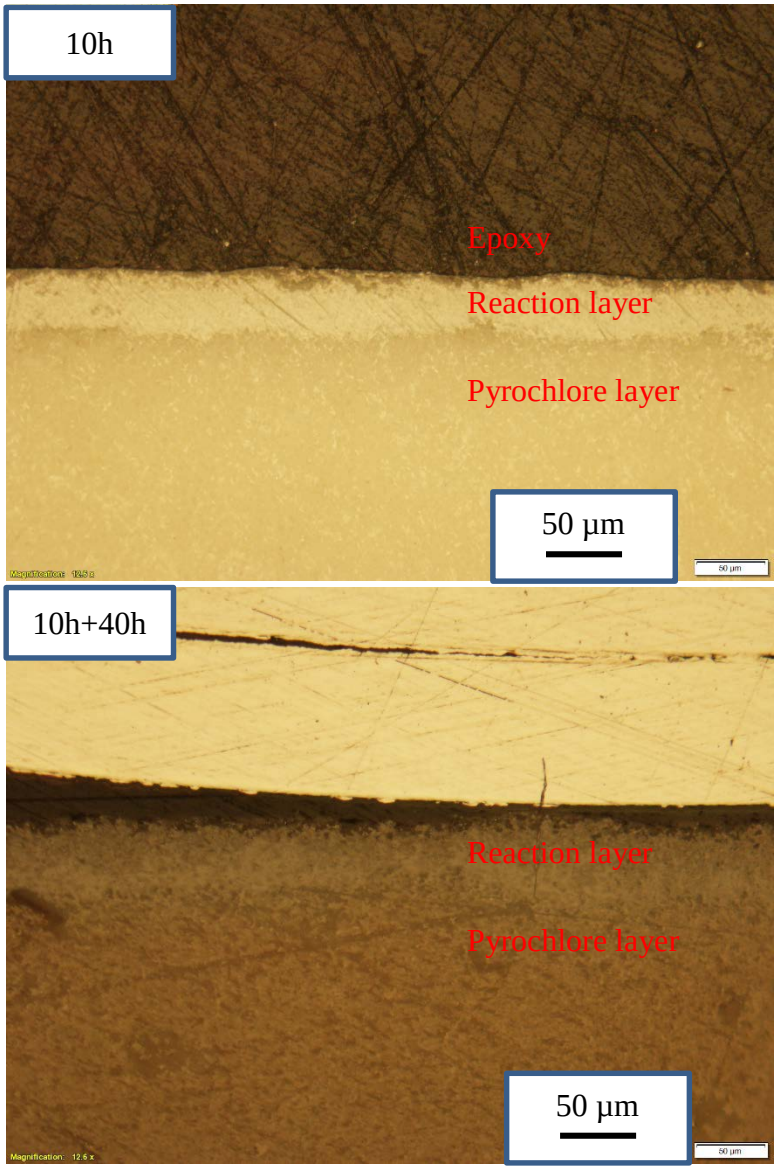

Figure 5.14 Cross-section of $Gd_2Zr_2O_7$ after CMAS corrosion for 10 hours and (10+40) hours.

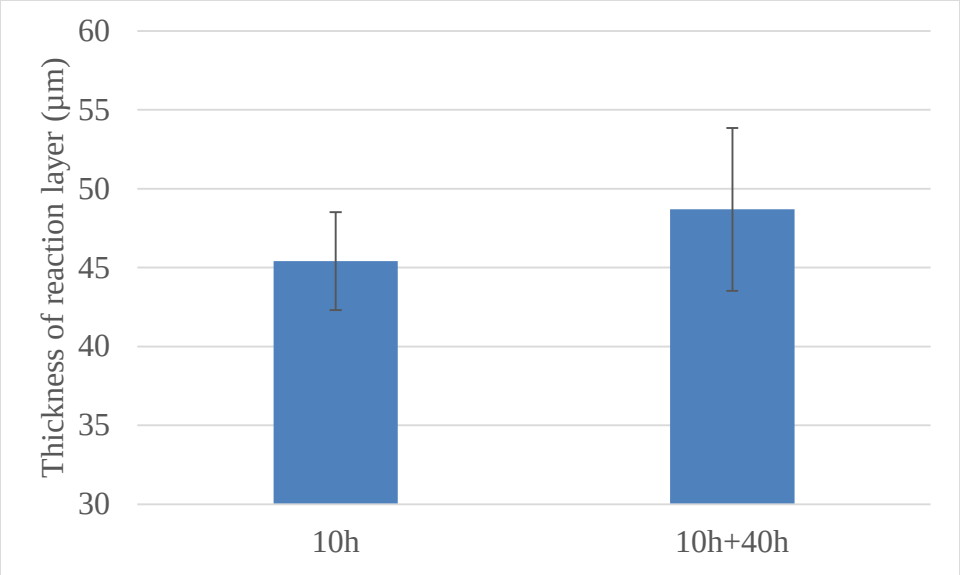

Figure 5.15 Average thickness of reaction layer after CMAS corrosion for 10 hours and (10+40) hours. Error bar represents the standard deviation. P-value equals 0.001. 40 locations were picked for each case.

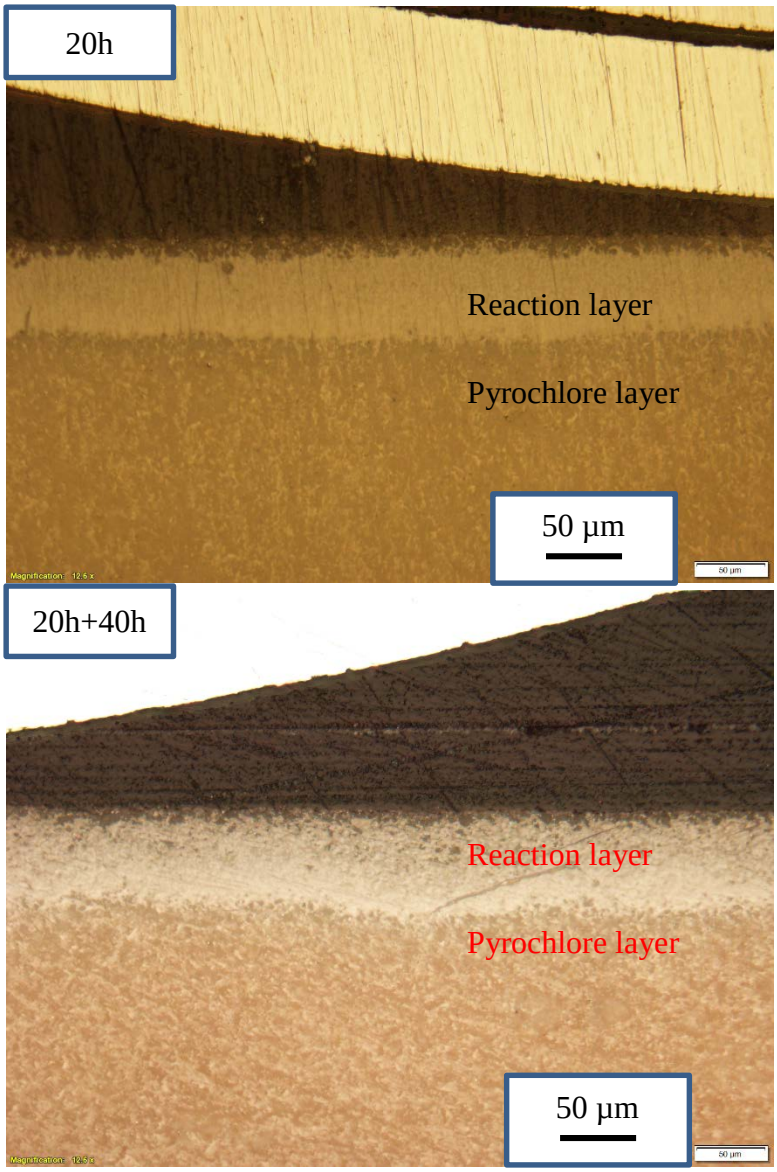

Figure 5.16 Cross-section of $Gd_2Zr_2O_7$ after CMAS corrosion for 20 hours and (20+40) hours.

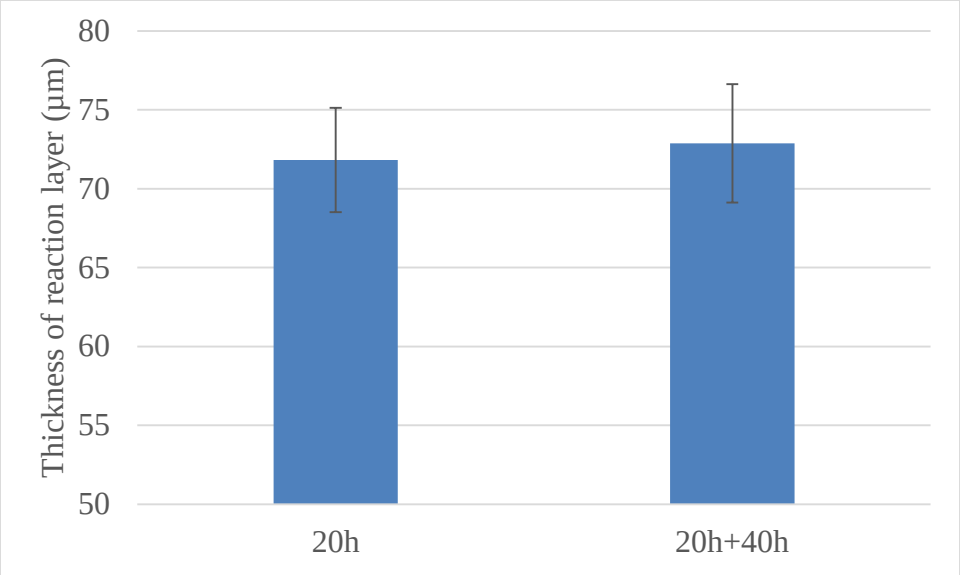

Figure 5.17 Average thickness of reaction layer after CMAS corrosion for 20 hours and (20+40) hours. Error bar represents the standard deviation. P-value equals 0.1865. 40 locations were picked for each case.

5.5. Relationship between thickness of reaction layer and CMAS amount

The relationship between thickness of reaction layer and CMAS amount was studied. $Gd_2Zr_2O_7$ samples were corroded with CMAS – 1 in the amount of 20mg/cm^2, 50mg/cm^2 and 100mg/cm^2 at the same condition respectively. Then the samples' cross-section were observed by optical microscope.

Figure 5.18 shows the optical images of $Gd_2Zr_2O_7$ after CMAS corrosion in different amount. The white layers in the images represent the reaction layer. The data reaction layers' thickness are shown in Figure 5.19. The thickness of reaction layer does not present linear relationship at higher CMAS amount because extra CMAS would melt and flow around the edge of the sample and then not all the CMAS infiltrated into the

pyrochlore layer. So the thickness of reaction layer at CMAS in 100mg/cm^2 is lower than the expected value.

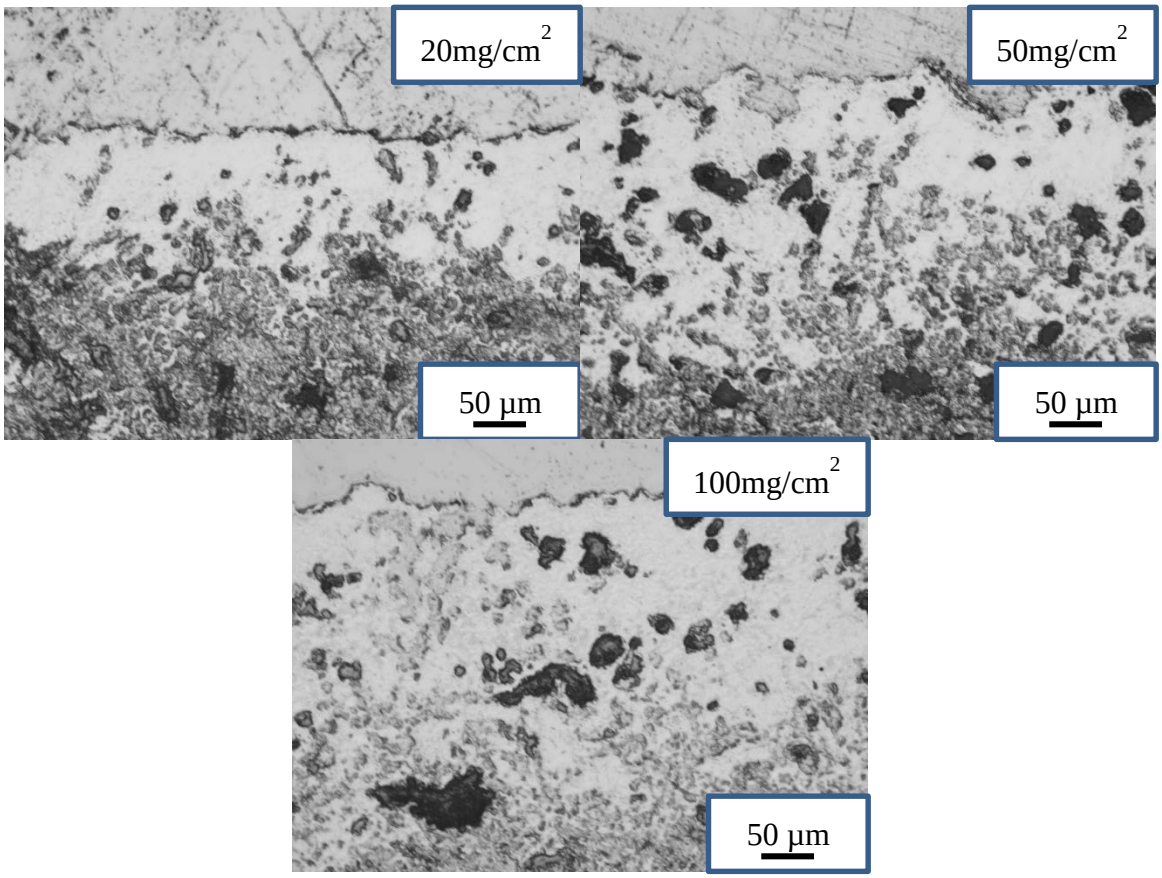

Figure 5.18 Optical images of $Gd_2Zr_2O_7$ after CMAS – 1 corrosion in the amount of 20mg/cm^2, 50mg/cm^2 and 100mg/cm^2.

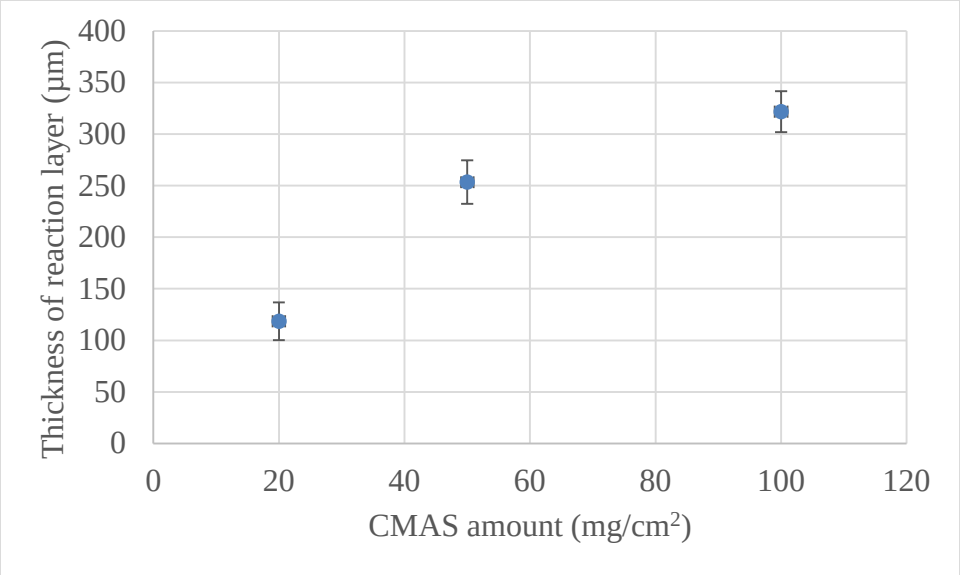

Figure 5.19 Thickness of reaction layers in $Gd_2Zr_2O_7$ after CMAS corrosion in different amount. Error bars represent standard deviation. 40 locations were picked for each case.

5.6. Conclusion

CMAS could infiltrate and react with both YSZ and pyrochlore materials and form a dense reaction layer. According to Figure 5.11, the infiltration depth of CMAS is much larger than the thickness of itself. Combined section 5.1 and section 5.2, the difference is that a porous transition layer existed in YSZ sample after CMAS corrosion. For pyrochlore materials ($Gd_2Zr_2O_7$ and $Sm_2Zr_2O_7$), the reaction layer and TBC layer had a clear boundary and when crossed the clear boundary, the CMAS element dropped to almost zero and the amount of lanthanide element and zirconium increased to normal value. While for YSZ, the boundary between transition layer and YSZ layer was not clear and the porous transition layer allowed more CMAS infiltration. As discussed in section 5.5, the reaction layer formed after CMAS corrosion could stand stable, even for longer additional corrosion time. Additionally, once the dense reaction layer formed, it can prevent further infiltration

and corrosion of extra CMAS, which is shown in section 5.3. Furthermore, as Figure 5.19 shows, the thickness of reaction layer at higher CMAS amount would be lower than the expected value because the extra CMAS would melt and flow across the edge and not all the CMAS would infiltrate the thermal barrier coatings.

CHAPTER 6. Conclusions

Lanthanide zirconates can react with CaO-MgO-Al_2O_3-SiO_2 (CMAS) both above and below the melting point of CMAS. Lanthanide zirconates prepared by co-precipitation method could provide uniform grain size and elemental distribution. In the corrosion process, lanthanide elements dissolved in CMAS and formed lanthanide calcium silicates and the remaining TBC materials formed zirconia in cubic fluorite phase. The reaction formula could be expressed as equation (7-1) shows.

Lanthanide zirconates + CMAS → Lanthanide calcium silicates + Fluorite zirconia (7-1)

After corrosion at higher temperature (>1250°C), lanthanide calcium silicates were in long stick shape and fluorite zirconia were in round shape. The fluorite zirconia phase also contained undissolved lanthanide element and the amount of lanthanide decreased as the corrosion temperature decreased. The increasing in Zr resulted to smaller lattice parameter in fluorite zirconia phase because Zr^{4+} had a lower ionic radius than Gd^{3+}/Sm^{3+}.

The CMAS corrosion at lower temperature (<1250°C), the corrosion presented similar mechanism at higher temperature. The reaction products were calcium lanthanide silicates and cubic fluorite zirconia. However, some new extra CMAS phases formed. $CaAl_2Si_2O_8$ single crystal in long stick shape phase with tens of microns formed after CMAS corrosion. Furthermore, CMAS corrosion on lower porosities' (19%) lanthanide zirconates could form $Mg_2Al_2Si_6Ca_6O_{23}$ single crystal at some certain circumstance and this phase also presented in the XRD pattern with higher intensity. The $Mg_2Al_2Si_6Ca_6O_{23}$

single crystal only formed at lanthanide zirconates with lower porosity and corroded by CMAS with smaller amount of Al.

The calcium lanthanide silicates and cubic fluorite zirconia phases were stable both above and below the melting point of CMAS. However, once the corrosion reaction was taken place at higher temperature, the $Mg_2Al_2Si_6Ca_6O_{23}$ and $CaAl_2Si_2O_8$ single crystals would not form. Additionally, the lanthanide zirconates' porosity can only affect the formation of $Mg_2Al_2Si_6Ca_6O_{23}$ and $CaAl_2Si_2O_8$ single crystals. Reaction products calcium lanthanide zirconates and cubic fluorite zirconia were not influenced by ceramics' porosities and CMAS composition.

The whole process of reaction between CMAS and pyrochlore materials could be summarized in Figure 6.1. CMAS powders could infiltrate the pyrochlore materials through the pores and then react with the zirconates. After reaction, a dense reaction layer formed. The dense reaction layer could stand stable and grows in a low rate in the further corrosion. Moreover, the dense reaction layer could also prevent further corrosion by obstructing the infiltration of extra CMAS. Small amount of CMAS glass backgrounds still exist in the dense reaction layer and it would react with the pyrochlore materials. But according to the Figure 5.15 and Figure 5.17, the reaction layer grows slowly than its formation.

As compared, the schematic diagram of CMAS corrosion on YSZ is shown in Figure 6.2. As similar as pyrochlore materials, CMAS can also infiltrate the YSZ via the pores and react with YSZ. The difference is that a porous transition layer between reaction layer and YSZ layer formed after corrosion.

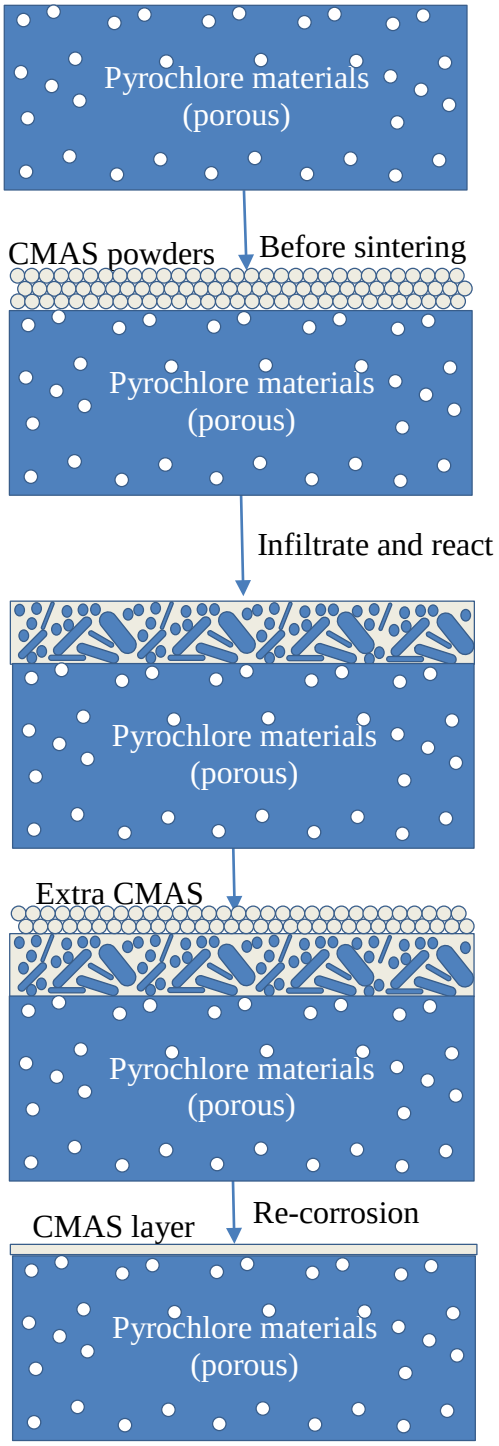

Figure 6.1 Schematic diagram of reaction mechanism between CMAS and lanthanide zirconates pyrochlore materials. The blue spheres represent the cubic fluorite zirconia and the sticks represent silicates.

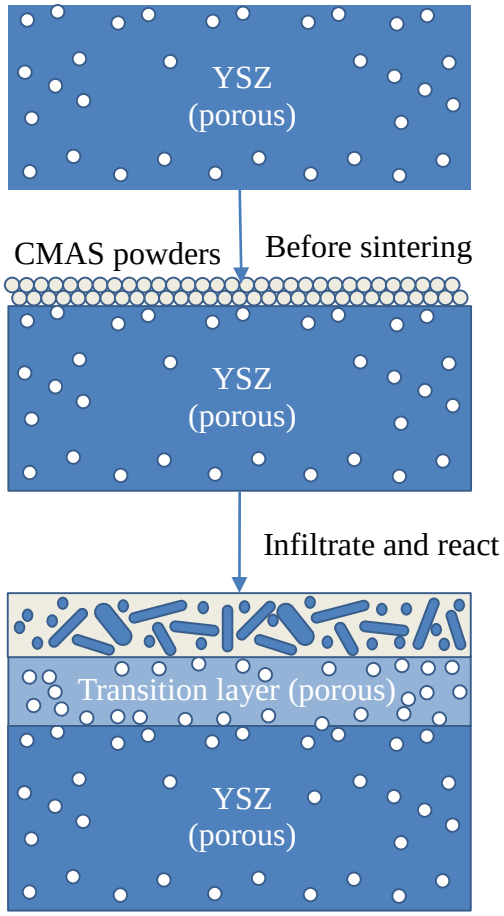

Figure 6.2 Schematic diagram of reaction mechanism between CMAS and yttria stabilized zirconia. The dark blue block represents YSZ material and light blue block means the transition layer.

Water in corrosion process at lower temperature (<1250°C) can also affect the crystal size of $Mg_2Al_2Si_6Ca_6O_{23}$. $Mg_2Al_2Si_6Ca_6O_{23}$ single crystal was much larger than that formed without water. Furthermore, the main reaction products calcium lanthanide zirconates and cubic fluorite zirconia were not influenced by water flow.

Corrosion quantification was also studied in this work. CMAS could react with lanthanide zirconates materials and form a dense layer. The reaction layer and pyrochlore layer were divided by a clear boundary. The reaction layer was rich in Ca, Mg, Al and Si

and the amount of lanthanide and zirconium element was small. However, the amount of CMAS would drop to almost zero when crossed the clear boundary and the amount of Gd/Sm and Zr would increase to normal value. As comparison, YSZ could also react with CMAS and formed not only a reaction layer, but also a porous transition layer. The elemental distribution in the three layers (reaction layer, transition layer and YSZ layer) presented like three steps. The porous transition layer also had some amount of CMAS and dropped to almost zero when crossed the boundary between porous layer and YSZ layer. The porous transition layer would allow more CMAS infiltration and react with YSZ layer below. Thus, YSZ presented lower corrosion resistance against CMAS.

CHAPTER 7. Future work

Sulfur and vanadium corrosion have been studied by several researchers and CMAS corrosion mechanism is discussed in this dissertation, but the complex corrosion by sulfur and CMAS haven't been published yet. CMAS corrosion are always combined with sulfur corrosion at different temperatures, especially for the low-quality fuels and marine based turbine engines. To further understand the corrosion process in the real application, a study in CMAS corrosion combined with sulfur corrosion is necessary. Since sulfur corrosion has a lower reaction temperature (650°C~1000°C) than CMAS corrosion (see 1.3.4), the suggested further research will be targeted at building a corrosion system that contains both sulfur, vanadium and CMAS. To achieve this, the pyrochlore lanthanide zirconiates would be corroded by sulfate and vanadium oxide at lower temperature (650°C~1000°C) to form a reaction layer. The corrosion procedures could be designed as similar as CMAS corrosion mentioned in this dissertation. The reaction product can be characterized by XRD, SEM and EDS. Then the corroded materials with reaction layer will be exposed to CMAS to study the CMAS corrosion properties of reaction layer formed in sulfur corrosion. The corrosion can be studied in several valuables, including corrosion temperature, composition of corrosion materials, microstructure of TBC materials, etc.

Additionally, pores are necessary in thermal barrier coatings to reduce the residual stress in thermal cycling, so the dense reaction layer formed after CMAS corrosion should have negative effect in thermal cycling property. Meanwhile, gas turbine engines,

especially the engines used in airplanes always work in “room temperature – high temperature – room temperature” cycles, so cyclic corrosion need attention to simulate the real working environment. The suggested research target will be the effect of reaction layer in thermal cycling property of TBC materials. To achieve this, the thermal expansion coefficient of reaction product after CMAS corrosion should be studied. A modelling mechanism of thermal properties and reaction product deserves further study, which is helpful to the real application. Since water would be often injected into the engines during the raining time in the real application, the fundamental research is necessary in the corrosion process at moisture atmosphere, including formation of larger $Mg_2Al_2Si_6Ca_6O_{23}$ single crystal. This could be achieved by reaction between CMAS powder and pyrochlore materials in powder. Furthermore, the cyclic corrosion experiments are necessary to study the cyclic corrosion property. After cyclic corrosion, the cracks in the corroded materials’ can be observed by SEM to study the effect on residual stress.

Appendix I. d-spacing of pyrochlore materials from non-corrosion to corrosion at various temperatures

Table I.i Angles' value of non-corroded $Gd_2Zr_2O_7$ and corroded at various temperature.

	Non-corrosion	1500°C	1400°C	1300°C
$2\theta_1$(°)/(111)	29.305	29.568	29.717	29.919
$2\theta_2$(°)/(200)	33.966	34.285	34.438	34.69
$2\theta_3$(°)/(220)	48.807	49.357	49.498	49.838
$2\theta_4$(°)/(311)	57.944	58.503	58.777	59.238
$2\theta_5$(°)/(222)	60.807	61.399	61.695	62.145
$2\theta_6$(°)/(400)	71.501	72.225	72.587	73.157
$2\theta_7$(°)/(331)	79.102	79.925	80.375	81.011
$2\theta_8$(°)/(420)	81.603	82.415	82.864	83.599

Table I.ii d-spacing of $Gd_2Zr_2O_7$ before and after corrosion.

	Non-corrosion	1500°C	1400°C	1300°C
d_1(Å)/(111)	3.044	3.018	3.003	2.983
d_2(Å)/(200)	2.636	2.612	2.601	2.583
d_3(Å)/(220)	1.864	1.844	1.839	1.828
d_4(Å)/(311)	1.590	1.576	1.569	1.558
d_5(Å)/(222)	1.521	1.508	1.502	1.492
d_6(Å)/(400)	1.318	1.306	1.301	1.292

d_7(Å)/(331)	1.209	1.199	1.193	1.185
d_8(Å)/(420)	1.178	1.169	1.164	1.155

Table I.iii Angles' value of non-corroded $Sm_2Zr_2O_7$ and corroded at various temperature.

	Non-corrosion	1500°C	1400°C	1300°C
$2\theta_1$(°)/(111)	29.129	29.480	29.546	29.963
$2\theta_2$(°)/(200)	33.769	34.175	34.263	34.723
$2\theta_3$(°)/(220)	48.500	49.103	49.246	49.893
$2\theta_4$(°)/(311)	57.582	58.339	58.470	59.282
$2\theta_5$(°)/(222)	60.401	61.234	61.366	62.189
$2\theta_6$(°)/(400)	71.018	72.027	72.247	73.300
$2\theta_7$(°)/(331)	78.532	79.706	79.804	81.066
$2\theta_8$(°)/(420)	81.000	82.119	82.239	83.643

Table I.iv d-spacing of $Sm_2Zr_2O_7$ before and after corrosion.

	Non-corrosion	1500°C	1400°C	1300°C
d_1(Å)/(111)	3.062	3.026	3.020	2.979
d_2(Å)/(200)	2.651	2.621	2.614	2.580
d_3(Å)/(220)	1.875	1.853	1.848	1.826
d_4(Å)/(311)	1.599	1.580	1.577	1.557
d_5(Å)/(222)	1.531	1.512	1.509	1.491
d_6(Å)/(400)	1.326	1.310	1.306	1.290

d_7(Å)/(331)	1.217	1.202	1.200	1.185
d_8(Å)/(420)	1.186	1.172	1.171	1.155

Appendix II. Grain size of $Gd_2Zr_2O_7$ after CMAS corrosion

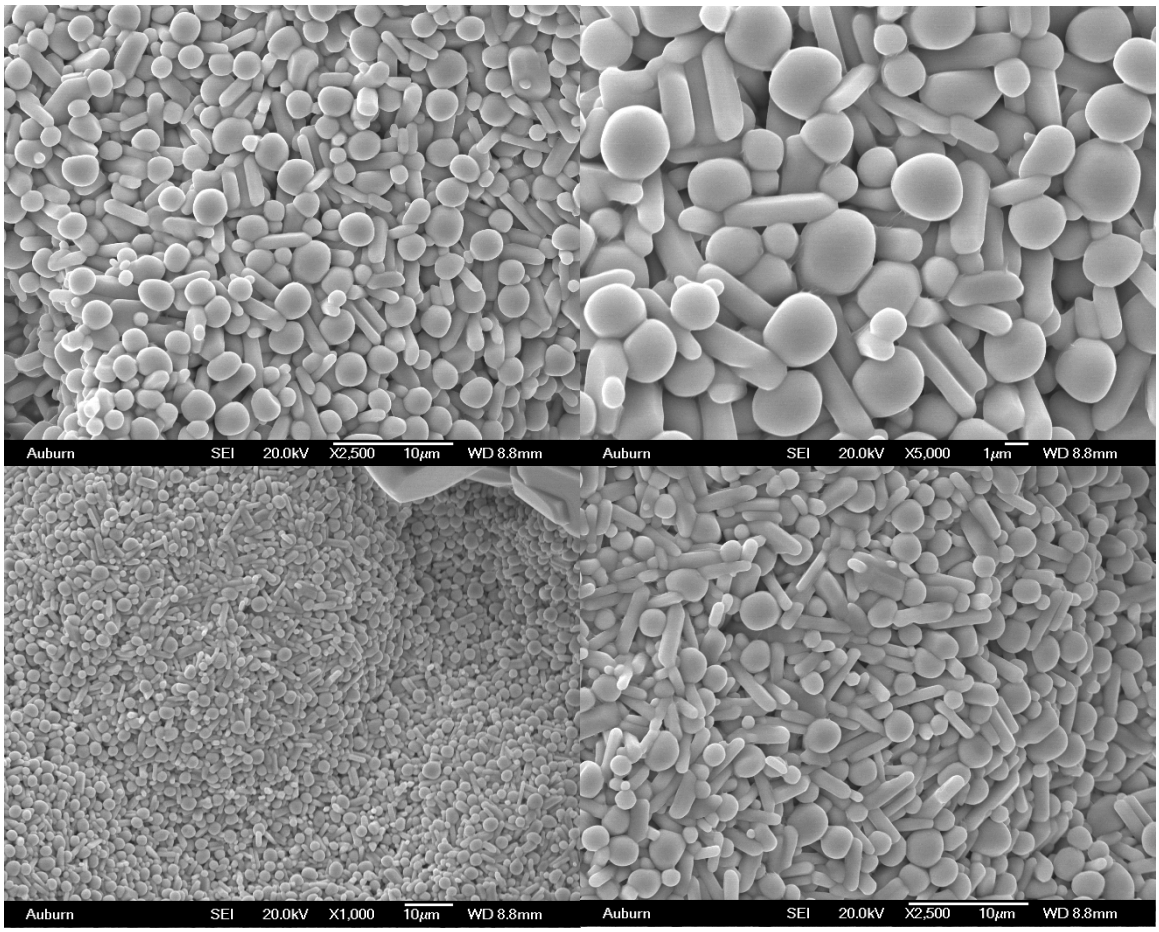

Figure II. i $Gd_2Zr_2O_7$ after CMAS – 1 corrosion at 1200°C for 20 hours.

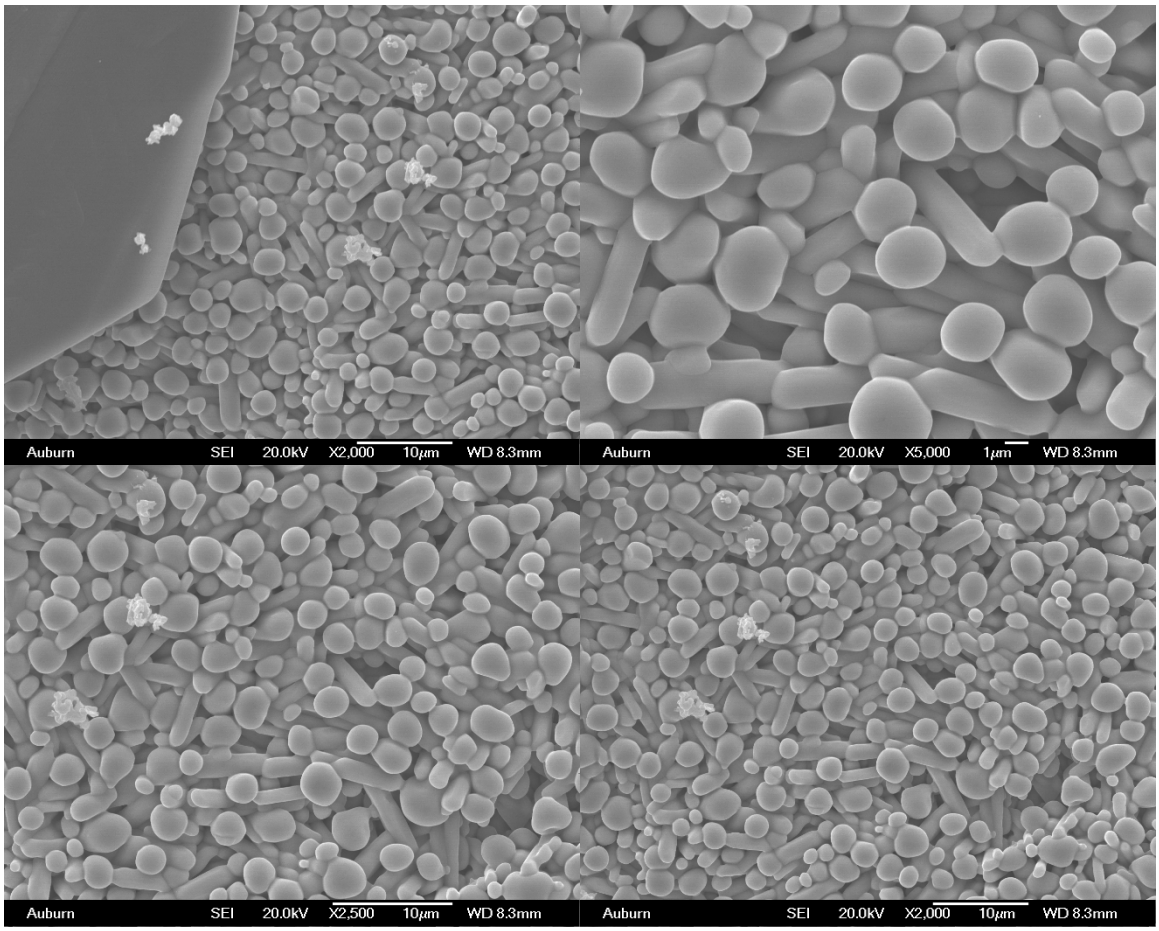

Figure II. ii $Gd_2Zr_2O_7$ after CMAS – 1 corrosion at 1200°C for 40 hours.

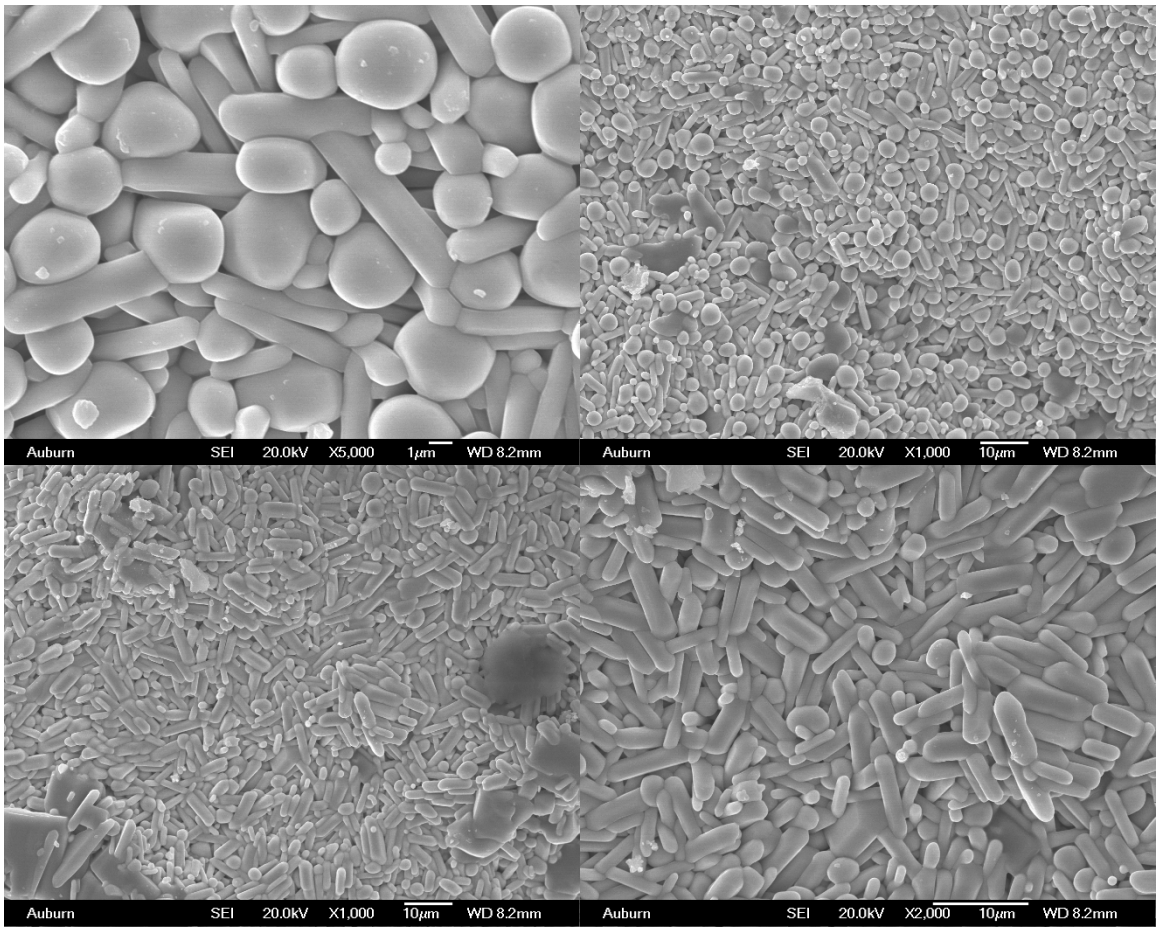

Figure II. iii $Gd_2Zr_2O_7$ after CMAS – 1 corrosion at 1200°C for 60 hours.

Appendix III. Grain size of $(Gd_6Sm_4)_{0.2}Zr_2O_7$ after CMAS corrosion

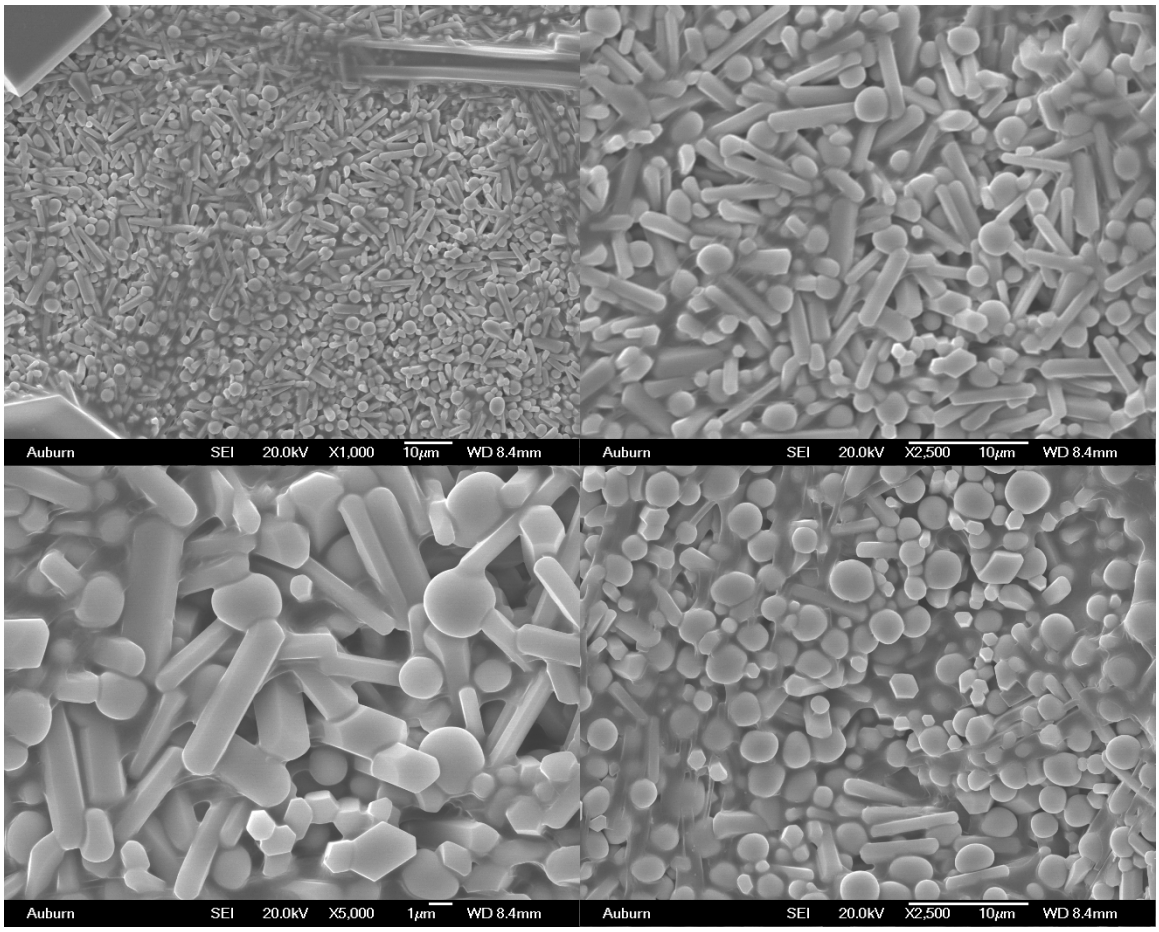

Figure III. i $(Gd_6Sm_4)_{0.2}Zr_2O_7$ after CMAS – 1 corrosion at 1200°C for 20 hours.

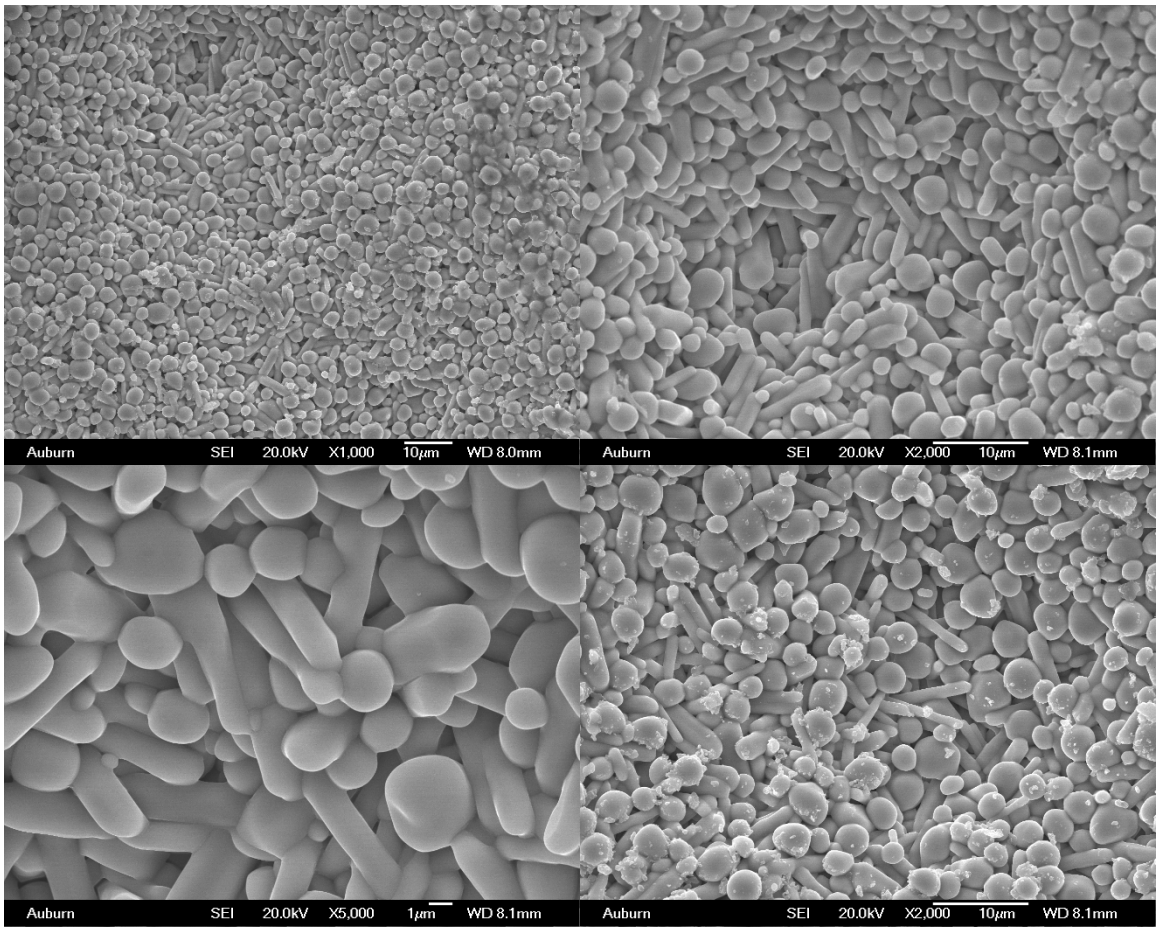

Figure III. ii $(Gd_6Sm_4)_{0.2}Zr_2O_7$ after CMAS – 1 corrosion at 1200°C for 40 hours.

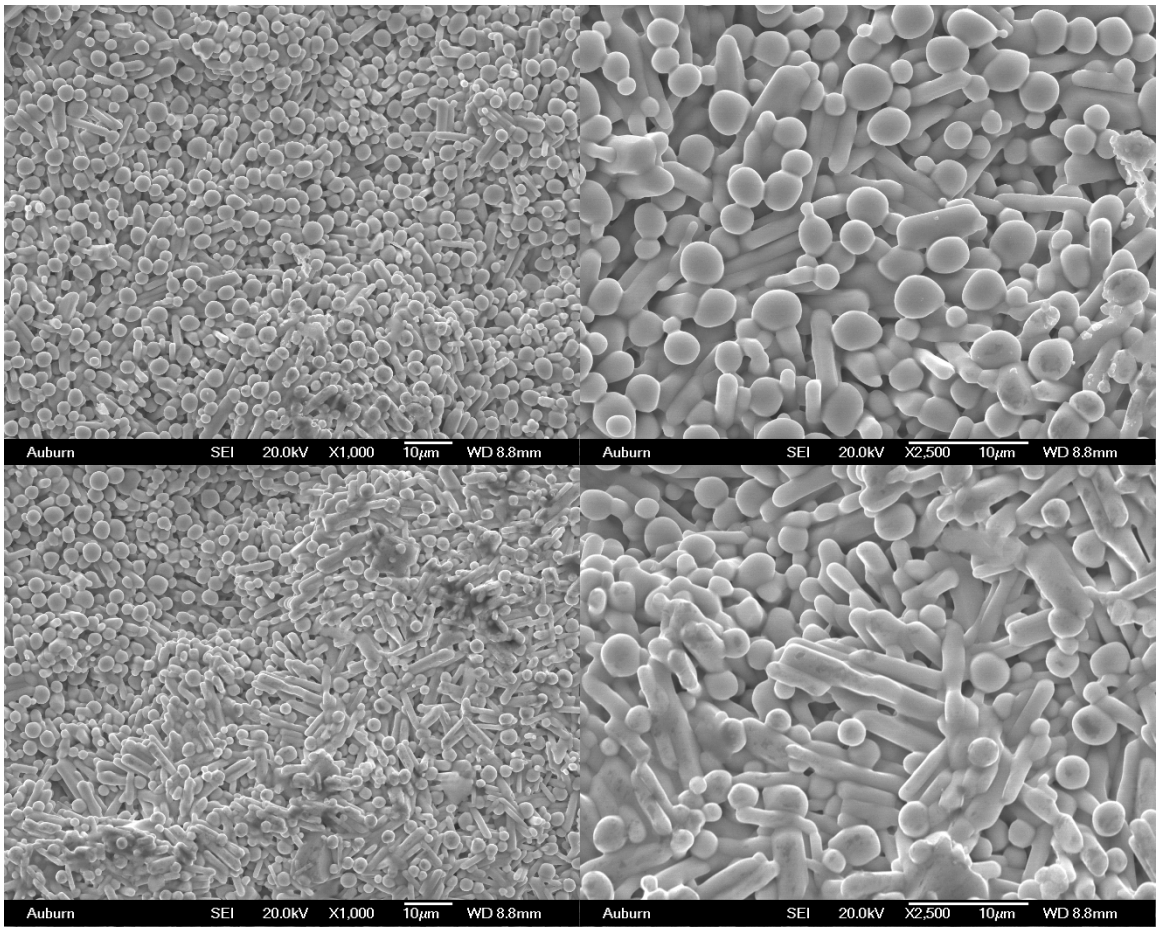

Figure III. iii $(Gd_6Sm_4)_{0.2}Zr_2O_7$ after CMAS – 1 corrosion at 1200°C for 60 hours.

Appendix IV. Grain size of $(Gd_8Sm_2)_{0.2}Zr_2O_7$ after CMAS corrosion

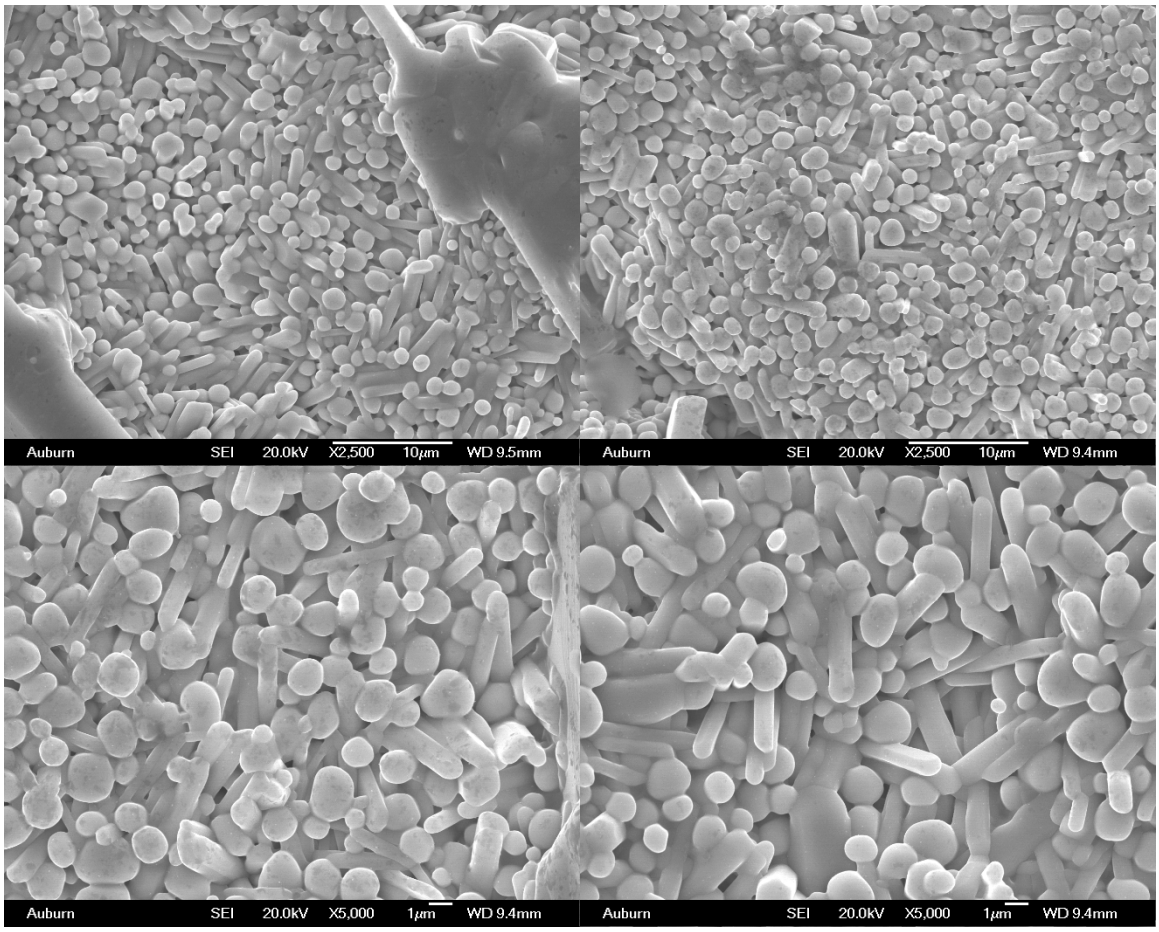

Figure IV. i $(Gd_8Sm_2)_{0.2}Zr_2O_7$ after CMAS – 1 corrosion at 1200°C for 20 hours.

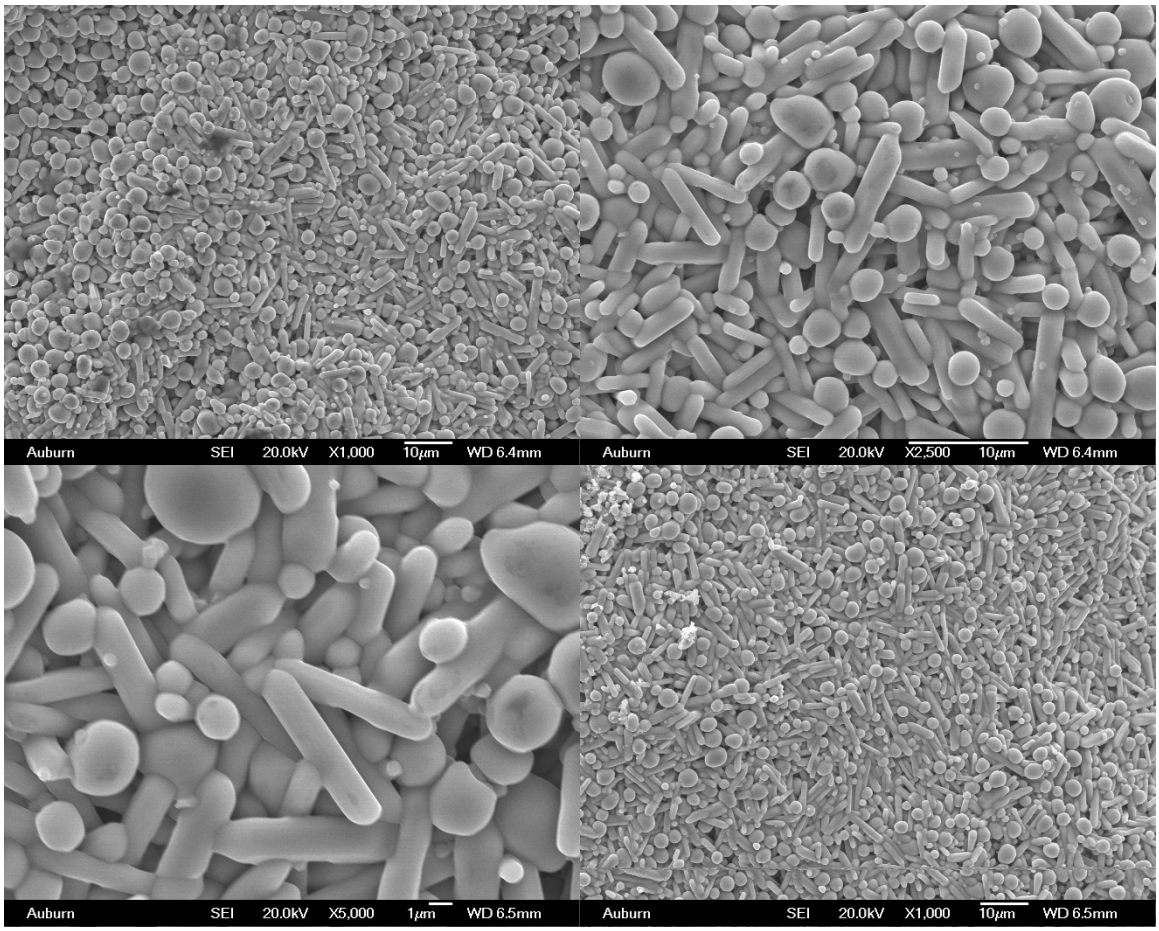

Figure IV. ii $(Gd_8Sm_2)_{0.2}Zr_2O_7$ after CMAS – 1 corrosion at 1200°C for 40 hours.

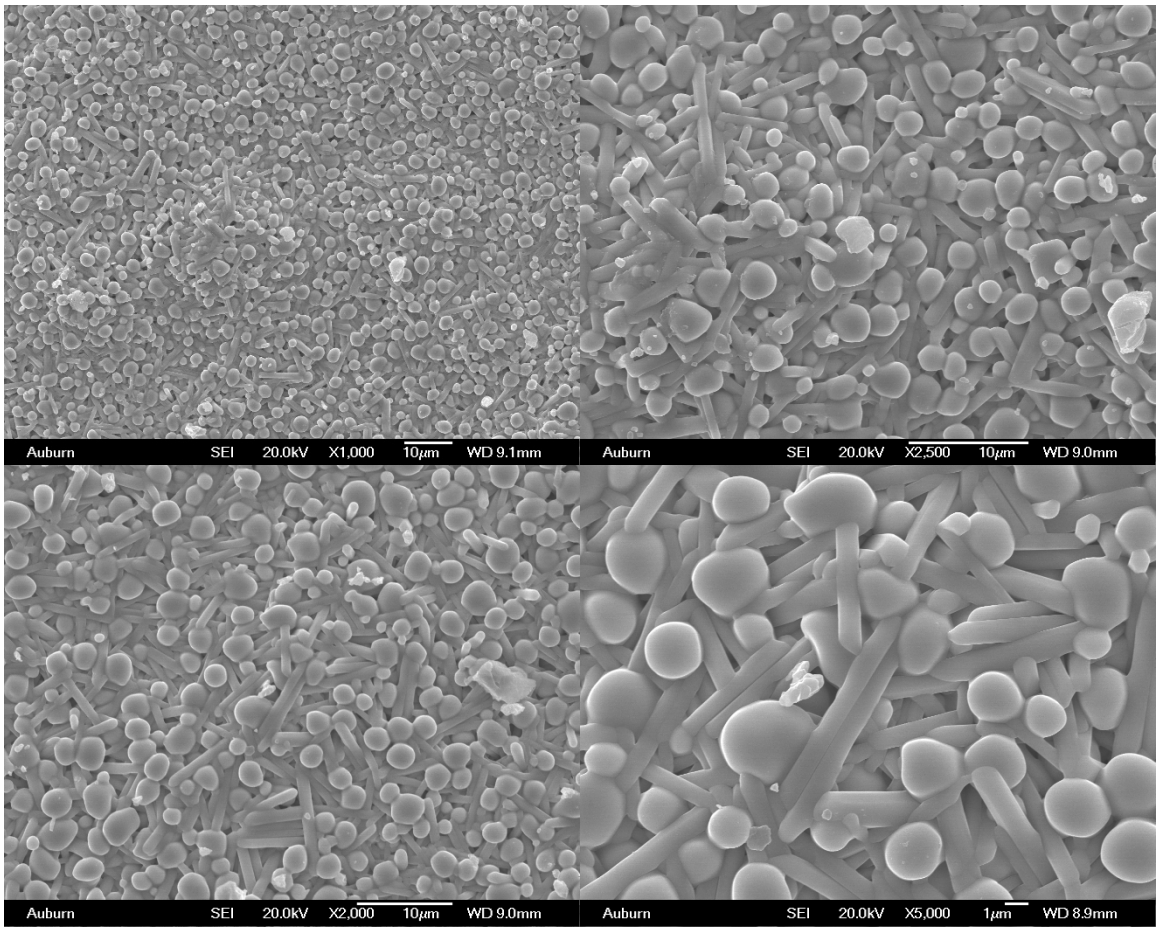

Figure IV. iii $(Gd_8Sm_2)_{0.2}Zr_2O_7$ after CMAS – 1 corrosion at 1200°C for 60 hours.

Appendix V. Grain size of $Mg_2Al_2Si_6Ca_6O_{23}$ single crystal

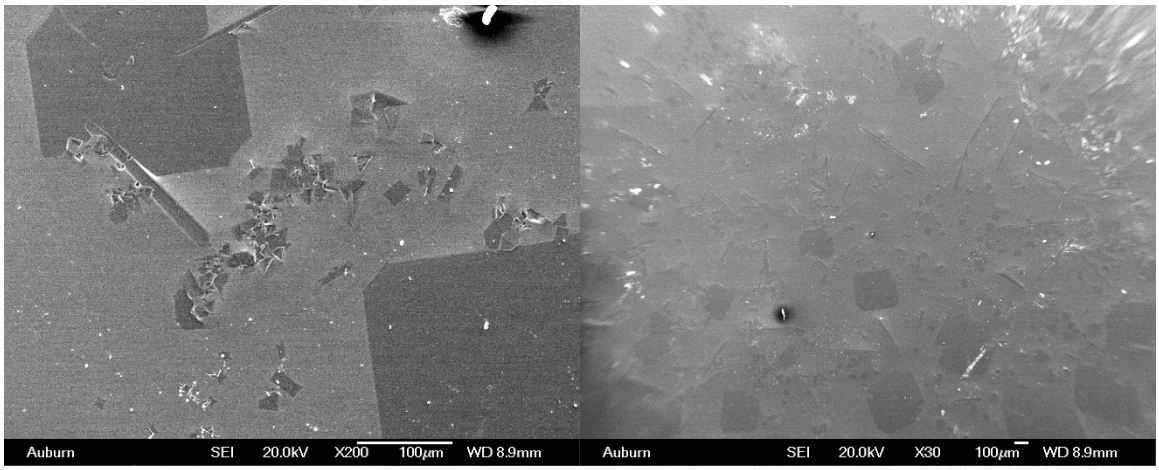

Figure V. i $Mg_2Al_2Si_6Ca_6O_{23}$ single crystal after CMAS corrosion at 1200°C for 10 hours with water flow.

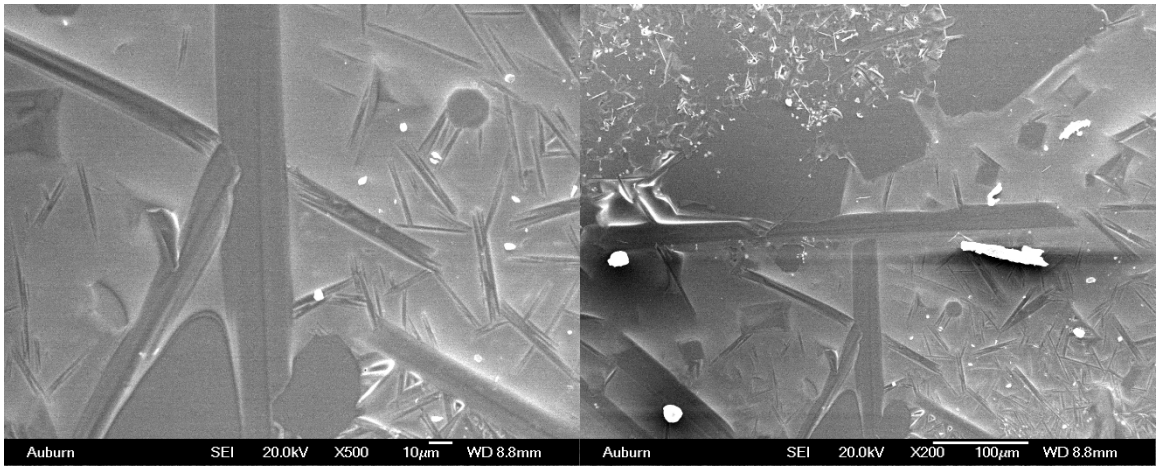

Figure V. ii $Mg_2Al_2Si_6Ca_6O_{23}$ single crystal after CMAS corrosion at 1200°C for 10 hours without water flow.

Reference

[1] J. M. M. Roco, S. Velasco, A. Medina, and A. C. Hernández, "Optimum performance of a regenerative Brayton thermal cycle," *Journal of Applied Physics,* vol. 82, pp. 2735-2741, 1997.

[2] J. C. Han, S. Dutta, and S. Ekkad, *Gas Turbine Heat Transfer and Cooling Technology, Second Edition*: Taylor & Francis, 2012.

[3] J. H. Perepezko, "The Hotter the Engine, the Better," *Science,* vol. 326, pp. 1068-1069, November 20, 2009 2009.

[4] D. R. Clarke, M. Oechsner, and N. P. Padture, "Thermal-barrier coatings for more efficient gas-turbine engines," *MRS Bulletin,* vol. 37, pp. 891-898, 2012.

[5] R. Darolia, "Thermal barrier coatings technology: critical review, progress update, remaining challenges and prospects," *International Materials Reviews,* vol. 58, pp. 315-348, 2013.

[6] A. Feuerstein, J. Knapp, T. Taylor, A. Ashary, A. Bolcavage, and N. Hitchman, "Technical and Economical Aspects of Current Thermal Barrier Coating Systems for Gas Turbine Engines by Thermal Spray and EBPVD: A Review," *Journal of Thermal Spray Technology,* vol. 17, pp. 199-213, 2008/06/01 2008.

[7] S. Meier, D. Gupta, and K. Sheffler, "Ceramic thermal barrier coatings for commercial gas turbine engines," *JOM,* vol. 43, pp. 50-53, 1991/03/01 1991.

[8] V. L. Wiesner and N. P. Bansal, "Mechanical and thermal properties of calcium–magnesium aluminosilicate (CMAS) glass," *Journal of the European Ceramic Society,* vol. 35, pp. 2907-2914, 9// 2015.

[9] J. Wu, H.-b. Guo, Y.-z. Gao, and S.-k. Gong, "Microstructure and thermo-physical properties of yttria stabilized zirconia coatings with CMAS deposits," *Journal of the European Ceramic Society,* vol. 31, pp. 1881-1888.

[10] S. Kramer, S. Faulhaber, M. Chambers, D. R. Clarke, C. G. Levi, J. W. Hutchinson, *et al.*, "Mechanisms of cracking and delamination within thick thermal barrier systems in aero-engines subject to calcium-magnesium-alumino-silicate (CMAS) penetration," *Materials Science and Engineering: A,* vol. 490, pp. 26-35, 2008.

[11] E. Lugscheider, K. Bobzin, S. Bärwulf, and A. Etzkorn, "Mechanical properties of EB-PVD-thermal barrier coatings by nanoindentation," *Surface and Coatings Technology,* vol. 138, pp. 9-13, 4/2/ 2001.

[12] U. Schulz, K. Fritscher, and M. Peters, "EB-PVD Y_2O_3- and $CeO_2Y_2O_3$-stabilized zirconia thermal barrier coatings — crystal habit and phase composition," *Surface and Coatings Technology,* vol. 82, pp. 259-269, 8// 1996.

[13] A. D. Jadhav, N. P. Padture, E. H. Jordan, M. Gell, P. Miranzo, and E. R. Fuller Jr, "Low-thermal-conductivity plasma-sprayed thermal barrier coatings with engineered microstructures," *Acta Materialia,* vol. 54, pp. 3343-3349, 2006.

[14] A. Kulkarni, Z. Wang, T. Nakamura, S. Sampath, A. Goland, H. Herman, *et al.*, "Comprehensive microstructural characterization and predictive property modeling

of plasma-sprayed zirconia coatings," *Acta Materialia,* vol. 51, pp. 2457-2475, 5/23/ 2003.

[15] A. F. Renteria, B. Saruhan, U. Schulz, H. J. Raetzer-Scheibe, J. Haug, and A. Wiedenmann, "Effect of morphology on thermal conductivity of EB-PVD PYSZ TBCs," *Surface and Coatings Technology,* vol. 201, pp. 2611-2620, 12/4/ 2006.

[16] H. Peng, L. Wang, L. Guo, W. Miao, H. Guo, and S. Gong, "Degradation of EB-PVD thermal barrier coatings caused by CMAS deposits," *Progress in Natural Science: Materials International,* vol. 22, pp. 461-467.

[17] S. Sampath, U. Schulz, M. O. Jarligo, and S. Kuroda, "Processing science of advanced thermal-barrier systems," *MRS Bulletin,* vol. 37, pp. 903-910, 2012.

[18] J. M. Drexler, C.-H. Chen, A. D. Gledhill, K. Shinoda, S. Sampath, and N. P. Padture, "Plasma sprayed gadolinium zirconate thermal barrier coatings that are resistant to damage by molten Ca-Mg-Al-silicate glass," *Surface and Coatings Technology,* vol. 206, pp. 3911-3916.

[19] T. Koomparkping, S. Damrongrat, and P. Niranatlumpong, "Al-rich precipitation in CoNiCrAlY bondcoat at high temperature," *Journal of Thermal Spray Technology,* vol. 14, pp. 264-267, 2005/06/01 2005.

[20] P. Niranatlumpong, C. B. Ponton, and H. E. Evans, "The Failure of Protective Oxides on Plasma-Sprayed NiCrAlY Overlay Coatings," *Oxidation of Metals,* vol. 53, pp. 241-258, 2000/04/01 2000.

[21] Z. Xu, J. Dai, J. Niu, N. Li, G. Huang, and L. He, "Thermal shock behavior of platinum aluminide bond coat/electron beam-physical vapor deposited thermal barrier coatings," *Journal of Alloys and Compounds,* vol. 617, pp. 185-191, 12/25/ 2014.

[22] Y. Zhang, W. Y. Lee, J. A. Haynes, I. G. Wright, K. M. Cooley, and P. K. Liaw, "Synthesis and cyclic oxidation behavior of a (Ni, Pt) Al coating on a desulfurized Ni-base superalloy," *Metallurgical and Materials Transactions A,* vol. 30, pp. 2679-2687, 1999/10/01 1999.

[23] S. J. Laney, "Effect of surface conditioning of platinum aluminide bond coats on thermal barrier coating life," Master, University of Pittsburgh, 2004.

[24] B. Gleeson, N. Mu, and S. Hayashi, "Compositional factors affecting the establishment and maintenance of Al2O3 scales on Ni–Al–Pt systems," *Journal of Materials Science,* vol. 44, pp. 1704-1710, 2009/04/01 2009.

[25] P. Y. Hou and K. F. McCarty, "Surface and interface segregation in β-NiAl with and without Pt addition," *Scripta Materialia,* vol. 54, pp. 937-941, 3// 2006.

[26] Y. Zhang, J. A. Haynes, G. Wright, B. A. Pint, K. M. Cooley, W. Y. Lee, *et al.*, "Effects of Pt incorporation on the isothermal oxidation behavior of chemical vapor deposition aluminide coatings," *Metallurgical and Materials Transactions A,* vol. 32, pp. 1727-1741, 2001/07/01 2001.

[27] J. L. S. Yongqing Wang, Marc Suneson, "Oxidation behavior of Hf-modified aluminide coatings on Inconel-718 at 1050°C," *Journal of Coating Science and Technology,* vol. 1, pp. 25-45, 2014.

[28] B. A. Pint, I. G. Wright, W. Y. Lee, Y. Zhang, K. Prüßner, and K. B. Alexander, "Substrate and bond coat compositions: factors affecting alumina scale adhesion," *Materials Science and Engineering: A,* vol. 245, pp. 201-211, 5/1/ 1998.

[29] B. A. Pint, K. L. More, and I. G. Wright, "Effect of Quaternary Additions on the Oxidation Behavior of Hf-Doped NiAl," *Oxidation of Metals*, vol. 59, pp. 257-283, 2003/04/01 2003.

[30] J. Rösler, M. Bäker, and M. Volgmann, "Stress state and failure mechanisms of thermal barrier coatings: role of creep in thermally grown oxide," *Acta Materialia*, vol. 49, pp. 3659-3670, 10/26/ 2001.

[31] D. R. Mumm, A. G. Evans, and I. T. Spitsberg, "Characterization of a cyclic displacement instability for a thermally grown oxide in a thermal barrier system," *Acta Materialia*, vol. 49, pp. 2329-2340, 2001.

[32] W. R. Chen, X. Wu, B. R. Marple, and P. C. Patnaik, "The growth and influence of thermally grown oxide in a thermal barrier coating," *Surface and Coatings Technology*, vol. 201, pp. 1074-1079, 10/5/ 2006.

[33] A. M. Karlsson, J. W. Hutchinson, and A. G. Evans, "The displacement of the thermally grown oxide in thermal barrier systems upon temperature cycling," *Materials Science and Engineering: A*, vol. 351, pp. 244-257, 6/25/ 2003.

[34] A. G. Evans, D. R. Mumm, J. W. Hutchinson, G. H. Meier, and F. S. Pettit, "Mechanisms controlling the durability of thermal barrier coatings," *Progress in Materials Science*, vol. 46, pp. 505-553, // 2001.

[35] R. A. Miller, "Thermal barrier coatings for aircraft engines: history and directions," *Journal of Thermal Spray Technology*, vol. 6, pp. 35-42, 1997/03/01 1997.

[36] R. Mévrel, J.-C. Laizet, A. Azzopardi, B. Leclercq, M. Poulain, O. Lavigne, *et al.*, "Thermal diffusivity and conductivity of $Zr_{1-x}Y_xO_{2-x/2}$ (x=0, 0.084 and 0.179) single crystals," *Journal of the European Ceramic Society*, vol. 24, pp. 3081-3089, 9// 2004.

[37] W. Pan, S. R. Phillpot, C. Wan, A. Chernatynskiy, and Z. Qu, "Low thermal conductivity oxides," *MRS Bulletin*, vol. 37, pp. 917-922, 2012.

[38] W. Chi, S. Sampath, and H. Wang, "Microstructure–Thermal Conductivity Relationships for Plasma-Sprayed Yttria-Stabilized Zirconia Coatings," *Journal of the American Ceramic Society*, vol. 91, pp. 2636-2645, 2008.

[39] K. Bobzin, N. Bagcivan, T. Brögelmann, and B. Yildirim, "Influence of temperature on phase stability and thermal conductivity of single- and double-ceramic-layer EB–PVD TBC top coats consisting of 7YSZ, $Gd_2Zr_2O_7$ and $La_2Zr_2O_7$," *Surface and Coatings Technology*, vol. 237, pp. 56-64, 12/25/ 2013.

[40] H. Liu, S. Li, Q. Li, Y. Li, and W. Zhou, "Microstructure, phase stability and thermal conductivity of plasma sprayed Yb_2O_3, Y_2O_3 co-stabilized ZrO_2 coatings," *Solid State Sciences*, vol. 13, pp. 513-519, 3// 2011.

[41] S. Raghavan, H. Wang, R. B. Dinwiddie, W. D. Porter, and M. J. Mayo, "The effect of grain size, porosity and yttria content on the thermal conductivity of nanocrystalline zirconia," *Scripta Materialia*, vol. 39, pp. 1119-1125, 9/15/ 1998.

[42] S. Stecura, "New ZrO_2 Yb_2O_3 plasma-sprayed coatings for thermal barrier applications," *Thin Solid Films*, vol. 150, pp. 15-40, 6/22/ 1987.

[43] G. Witz, V. Shklover, W. Steurer, S. Bachegowda, and H.-P. Bossmann, "Phase Evolution in Yttria-Stabilized Zirconia Thermal Barrier Coatings Studied by Rietveld Refinement of X-Ray Powder Diffraction Patterns," *Journal of the American Ceramic Society*, vol. 90, pp. 2935-2940, 2007.

[44] J. A. Krogstad, S. Krämer, D. M. Lipkin, C. A. Johnson, D. R. G. Mitchell, J. M. Cairney, *et al.*, "Phase Stability of t′ -Zirconia-Based Thermal Barrier Coatings: Mechanistic Insights," *Journal of the American Ceramic Society,* vol. 94, pp. s168-s177, 2011.

[45] J. Chevalier, L. Gremillard, A. V. Virkar, and D. R. Clarke, "The Tetragonal-Monoclinic Transformation in Zirconia: Lessons Learned and Future Trends," *Journal of the American Ceramic Society,* vol. 92, pp. 1901-1920, 2009.

[46] M. P. Borom, C. A. Johnson, and L. A. Peluso, "Role of environment deposits and operating surface temperature in spallation of air plasma sprayed thermal barrier coatings," *Surface and Coatings Technology,* vol. 86–87, Part 1, pp. 116-126, 12/1/ 1996.

[47] P. Mohan, B. Yuan, T. Patterson, V. H. Desai, and Y. H. Sohn, "Degradation of Yttria-Stabilized Zirconia Thermal Barrier Coatings by Vanadium Pentoxide, Phosphorous Pentoxide, and Sodium Sulfate," *Journal of the American Ceramic Society,* vol. 90, pp. 3601-3607, 2007.

[48] "Figure 14171 in Phase Equilibrium Diagrams for Ceramic Systems, Version 4.0, (American Ceramic Society, Westerville, OH, 2013).", ed.

[49] "Figure 14384 in Phase Equilibrium Diagrams for Ceramic Systems, Version 4.0, (American Ceramic Society, Westerville, OH, 2013).", ed.

[50] A. R. Cleave, "Atomic Scale Simulations for Waste Form Applications," Doctor of Philosophy, Department of Materials, Imperial College of Science, Technology and Medicine, 2006.

[51] R. Vassen, X. Cao, F. Tietz, D. Basu, and D. Stöver, "Zirconates as New Materials for Thermal Barrier Coatings," *Journal of the American Ceramic Society,* vol. 83, pp. 2023-2028, 2000.

[52] H. Lehmann, D. Pitzer, G. Pracht, R. Vassen, and D. Stöver, "Thermal Conductivity and Thermal Expansion Coefficients of the Lanthanum Rare-Earth-Element Zirconate System," *Journal of the American Ceramic Society,* vol. 86, pp. 1338-1344, 2003.

[53] W. Ma, D. Wang, H. Dong, W. Lun, W. He, and X. Zheng, "Double Rare-Earth Oxides Co-doped Strontium Zirconate as a New Thermal Barrier Coating Material," *Journal of Thermal Spray Technology,* vol. 22, pp. 104-109, 2013/03/01 2013.

[54] G. Suresh, G. Seenivasan, M. V. Krishnaiah, and P. S. Murti, "Investigation of the thermal conductivity of selected compounds of lanthanum, samarium and europium," *Journal of Alloys and Compounds,* vol. 269, pp. L9-L12, 5/1/ 1998.

[55] R. Vaßen, G. Kerkhoff, and D. Stöver, "Development of a micromechanical life prediction model for plasma sprayed thermal barrier coatings," *Materials Science and Engineering: A,* vol. 303, pp. 100-109, 5/15/ 2001.

[56] D. M. Lipkin and D. R. Clarke, "Measurement of the stress in oxide scales formed by oxidation of alumina-forming alloys," *Oxidation of Metals,* vol. 45, pp. 267-280, 1996/04/01 1996.

[57] S. Sodeoka, M. Suzuki, K. Ueno, H. Sakuramoto, T. Shibata, and M. Ando, "Thermal and mechanical properties of ZrO_2-CeO_2 plasma-sprayed coatings," *Journal of Thermal Spray Technology,* vol. 6, pp. 361-367, 1997/09/01 1997.

[58] X. Cao, R. Vassen, W. Fischer, F. Tietz, W. Jungen, and D. Stöver, "Lanthanum–Cerium Oxide as a Thermal Barrier-Coating Material for High-Temperature Applications," *Advanced Materials,* vol. 15, pp. 1438-1442, 2003.

[59] L. Ajdelsztajn, J. A. Picas, G. E. Kim, F. L. Bastian, J. Schoenung, and V. Provenzano, "Oxidation behavior of HVOF sprayed nanocrystalline NiCrAlY powder," *Materials Science and Engineering: A,* vol. 338, pp. 33-43, 12/15/ 2002.

[60] A. Rabiei and A. G. Evans, "Failure mechanisms associated with the thermally grown oxide in plasma-sprayed thermal barrier coatings," *Acta Materialia,* vol. 48, pp. 3963-3976, 9/25/ 2000.

[61] E. A. G. Shillington and D. R. Clarke, "Spalling failure of a thermal barrier coating associated with aluminum depletion in the bond-coat," *Acta Materialia,* vol. 47, pp. 1297-1305, 3/10/ 1999.

[62] R. A. Miller and C. E. Lowell, "Failure mechanisms of thermal barrier coatings exposed to elevated temperatures," *Thin Solid Films,* vol. 95, pp. 265-273, 9/17/ 1982.

[63] D. Naumenko, V. Shemet, L. Singheiser, and W. Quadakkers, "Failure mechanisms of thermal barrier coatings on MCrAlY-type bondcoats associated with the formation of the thermally grown oxide," *Journal of Materials Science,* vol. 44, pp. 1687-1703, 2009/04/01 2009.

[64] W. R. Chen, X. Wu, B. R. Marple, and P. C. Patnaik, "Oxidation and crack nucleation/growth in an air-plasma-sprayed thermal barrier coating with NiCrAlY bond coat," *Surface and Coatings Technology,* vol. 197, pp. 109-115, 7/1/ 2005.

[65] M. Daroonparvar, M. A. M. Yajid, N. M. Yusof, S. Farahany, M. S. Hussain, H. R. Bakhsheshi-Rad, *et al.*, "Improvement of thermally grown oxide layer in thermal barrier coating systems with nano alumina as third layer," *Transactions of Nonferrous Metals Society of China,* vol. 23, pp. 1322-1333, 5// 2013.

[66] Q. Zhang, C.-J. Li, C.-X. Li, G.-J. Yang, and S.-C. Lui, "Study of oxidation behavior of nanostructured NiCrAlY bond coatings deposited by cold spraying," *Surface and Coatings Technology,* vol. 202, pp. 3378-3384, 4/15/ 2008.

[67] X. Lin, Y. Zeng, S. W. Lee, and C. Ding, "Characterization of alumina–3 wt.% titania coating prepared by plasma spraying of nanostructured powders," *Journal of the European Ceramic Society,* vol. 24, pp. 627-634, 4// 2004.

[68] J. Smialek, F. Archer, and R. Garlick, "Turbine airfoil degradation in the persian gulf war," *JOM,* vol. 46, pp. 39-41, 1994/12/01 1994.

[69] J. Wu, H. Guo, M. Abbas, and S. Gong, "Evaluation of plasma sprayed YSZ thermal barrier coatings with the CMAS deposits infiltration using impedance spectroscopy," *Progress in Natural Science: Materials International,* vol. 22, pp. 40-47, 2// 2012.

[70] S. Krämer, J. Yang, C. G. Levi, and C. A. Johnson, "Thermochemical Interaction of Thermal Barrier Coatings with Molten $CaO–MgO–Al_2O_3–SiO_2$ (CMAS) Deposits," *Journal of the American Ceramic Society,* vol. 89, pp. 3167-3175, 2006.

[71] S. Krämer, J. Yang, and C. G. Levi, "Infiltration-Inhibiting Reaction of Gadolinium Zirconate Thermal Barrier Coatings with CMAS Melts," *Journal of the American Ceramic Society,* vol. 91, pp. 576-583, 2008.

[72] R. Wellman, G. Whitman, and J. R. Nicholls, "CMAS corrosion of EB PVD TBCs: Identifying the minimum level to initiate damage," *International Journal of Refractory Metals and Hard Materials,* vol. 28, pp. 124-132, 1// 2010.

[73] J. M. Drexler, A. L. Ortiz, and N. P. Padture, "Composition effects of thermal barrier coating ceramics on their interaction with molten Ca–Mg–Al–silicate (CMAS) glass," *Acta Materialia,* vol. 60, pp. 5437-5447, 9// 2012.

[74] A. R. Krause, H. F. Garces, B. S. Senturk, and N. P. Padture, "$2ZrO_2 \cdot Y_2O_3$ Thermal Barrier Coatings Resistant to Degradation by Molten CMAS: Part II, Interactions with Sand and Fly Ash," *Journal of the American Ceramic Society,* vol. 97, pp. 3950-3957, 2014.

[75] P. Mohan, T. Patterson, B. Yao, and Y. Sohn, "Degradation of Thermal Barrier Coatings by Fuel Impurities and CMAS: Thermochemical Interactions and Mitigation Approaches," *Journal of Thermal Spray Technology,* vol. 19, pp. 156-167, 2010/01/01 2010.

[76] U. Schulz and W. Braue, "Degradation of La2Zr2O7 and other novel EB-PVD thermal barrier coatings by CMAS ($CaO–MgO–Al_2O_3–SiO_2$) and volcanic ash deposits," *Surface and Coatings Technology,* vol. 235, pp. 165-173, 11/25/ 2013.

[77] B. V. Marple, J; Moreau, C; Nagy DR, "Corrosion of thermal barrier coatings by vanadium and sulfur compounds," *Materials at high temperatures,* vol. 17, pp. 397-412, 2000.

[78] Z.-G. Liu, J.-H. Ouyang, Y. Zhou, and X.-L. Xia, "Hot corrosion behavior of V_2O_5-coated $Gd_2Zr_2O_7$ ceramic in air at 700–850 °C," *Journal of the European Ceramic Society,* vol. 29, pp. 2423-2427, 8// 2009.

[79] R. C. Buchanan, "Properties of hot-pressed zirconium pyrovanadate ceramics," *Journal of The Electrochemical Society,* vol. 130, pp. 1905-1910, 1983.

[80] R. L. Jones, "Thermogravimetric study of the 800°C reaction of zirconia stabilizing oxides with SO_3-$NaVO_3$," *Journal of the Electrochemical Society,* vol. 139, pp. 2794-2799, 1992.

[81] M. H. Habibi, L. Wang, and S. M. Guo, "Evolution of hot corrosion resistance of YSZ, Gd2Zr2O7, and Gd2Zr2O7 + YSZ composite thermal barrier coatings in Na2SO4 + V2O5 at 1050 °C," *Journal of the European Ceramic Society,* vol. 32, pp. 1635-1642, 7// 2012.

[82] F. S. P. R. H. Barkalow, "Mechanism of Hot Corrosion Attack of Ceramic Coatings Materials," *Proceedings of the First Conference on Advanced Materials for Alternative Fuel Capable Directly Fired Heat Engines,* pp. 704-414, 1979.

[83] J. C. Hamilton and A. S. Nagelberg, "In Situ Raman Spectroscopic Study of Yttria-Stabilized Zirconia Attack by Molten Sodium Vanadate," *Journal of the American Ceramic Society,* vol. 67, pp. 686-690, 1984.

[84] M. H. Habibi and S. M. Guo, "The hot corrosion behavior of plasma sprayed zirconia coatings stabilized with yttria, ceria, and titania in sodium sulfate and vanadium oxide," *Materials and Corrosion,* vol. 66, pp. 270-277, 2015.

[85] R. S. Roth, *Phase diagrams for ceramicsts,* 1981.

[86] C. Mercer, S. Faulhaber, A. G. Evans, and R. Darolia, "A delamination mechanism for thermal barrier coatings subject to calcium–magnesium–alumino-silicate (CMAS) infiltration," *Acta Materialia,* vol. 53, pp. 1029-1039, 2// 2005.

[87] J. M. Drexler, "Thermal Barrier Coatings Resistant to Glassy Deposits," M.S., Materials Science and Engineering, Ohio State University, 2011.
[88] R. Shannon, "Revised effective ionic radii and systematic studies of interatomic distances in halides and chalcogenides," *Acta Crystallographica Section A,* vol. 32, pp. 751-767, 1976.